NANOSTRUCTURE, BIOPIEZOELECTRIC AND BIOFERROELECTRIC BEHAVIORS OF MOLLUSK SHELLS STUDIED BY SCANNING PROBE MICROSCOPY TECHNIQUES

LI TAO

(B. Eng. (Hons.), National University of Singapore)

A THESIS SUBMITTED

FOR THE DEGREE OF DOCTOR OF PHILOSOPHY

DEPARTMENT OF MECHANICAL ENGINEERING

NATIONAL UNIVERSITY OF SINGAPORE

2013

DECLARATION

I hereby declare that this thesis is my original work and it has been written by me in its entirety. I have duly acknowledged all the sources of information which have been used in the thesis.

This thesis has also not been submitted for any degree in any university previously.

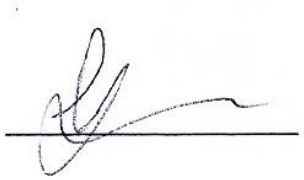

LI TAO

1 August 2013

LIST OF PUBLICATIONS

The research works and results reported herein were accomplished under the supervision of Associate Prof. Zeng Kaiyang from the Material Division of the Department of Mechanical Engineering, National University of Singapore. The major results presented in this dissertation have been published in variety of international journals or presented at international conferences and workshops that listed in the following.

Journal Papers

1. **T. Li** and K. Zeng, Nanoscale elasticity mappings of micro-constituents of the abalone shell by band excitation contact resonance force microscopy, **Nanoscale** (accepted, DOI:10.1039/C3NR05292C)

2. **T. Li** and K. Zeng, Nanoscale piezoelectric and ferroelectric behaviors of seashell by piezoresponse force microscopy, **Journal of Applied Physics** 113 (2013), 187202

3. **T. Li**, L. Chen, and K. Zeng, In situ studies of nanoscale electromechanical behavior of nacre under flexural stresses by Band Excitation PFM, **Acta Biomaterialia** 9 (2013), 5903-5912.

4. **T. Li** and K. Zeng, Nano-hierarchical structure and electromechanical coupling properties of clamshell, **Journal of Structural Biology**, 180 (2012), 73-83.

5. **T. Li** and K. Zeng, Piezoelectric properties and surface potential of Green Abalone shell studied by Scanning Probe Microscopy Techniques, **Acta Materialia**, 59 (2011), 3667-3679

Conference Presentations

1. **T. Li** and K. Zeng, "Electro-Mechanical Coupling Effects of the Green Abalone and Clam Shells", **6th World Congress on Biomechanics**, August 1-6, 2010, Singapore.

2. **T. Li** and K. Zeng, "Studies of Electromechanical Coupling Effects of Abalone and Clam Shells by Piezoresponse Force Microscopy", **8th**

International Workshop on Piezoresponse Force Microscopy, August 25-27, 2010, Beijing, China.

3. **T. Li** and K. Zeng, "Electromechanical Coupling of Abalone Shell by Scanning Probe Microscopy", **MRS (Materials Research Society) Spring Meeting** 2011, April 25-29, San Francisco, USA.

4. **T. Li** and K. Zeng, "Piezoelectricity and Ferroelectricity of Seashell by PFM", **ICYRAM (International Conference of Young Researchers on Advanced Materials)** 2012, July 1-6, Singapore.

5. **T. Li** and K. Zeng, "Piezoelectric and Ferroelectric Behaviors of Seashells", **ISAF-ECAPD-PFM (International Symposium on Applications on Ferroelectrics – European Conference on the Applications of Polar Dielectrics – International Symposium Piezoresponse Force Microscopy and Nanoscale Phenomena in Polar Materials)** 2012, July 9-13, Aveiro, Portugal.

6. **T. Li** and K. Zeng, "Nanoscale Biopiezoelectricity and Bioferroelectricity of Seashells by PFM", **ICMAT (International Conference on Materials for Advanced Technologies)** 2013, June 30-July 5, Singapore.

7. **T. Li** and K. Zeng, "Nanoscale Elasticity Mappings and Electromechanical Couplings of Abalone Shell", **ICBME (The 15th International Conference on Biomedical Engineering)** 2013, Dec 4-7, Singapore.

ACKNOWLEDGEMENTS

In the first place, I would like to express my sincere gratitude to all of the people who have selflessly offered their help and knowledge during my Ph.D. study, especially my supervisor Associated Prof. Zeng Kaiyang. His professional knowledge, advanced research skills, and personality charm have lightened up my pass towards the scientific success. I also would like to thank my group members including Dr. Wong Meng Fei, Dr. Chen Lei, Dr. Amit Kumar, Dr. Zhu Jing, Ms. Xiao Juanxiu, Ms. Yang Shan, and Ms. Lu Wanheng. I will not be able to overcome so many difficulties and challenges in my research works without the valuable help and encouragement from these people.

Also, I would like to thank the lab officers in materials lab, Mr. Thomas Tan, Mr. Ng Hong Wei, and Mr. Abdul Khalim Bin Abdul, for their patient guidance and helps in equipment usage, device purchasing, safety training, and many more daily activities that managed by them in our lab.

In addition, I would like to thank the service scientists from Asylum Research (USA), Dr. David Beck, Dr. Jason Li, and Dr. Amir Moshar. Whenever I have any queries, doubts, or difficulties, they always provide prompt helps to me. They are one of the important factors for me to get familiar and gradually master the usage of SPM technique, which is the key characterization tool in my research.

Last but not least, I would like to thank my parents and my husband for their seamless care, support, and encouragement. Without them I would not be able to thrive on my 4-year research life.

TABLE OF CONTENTS

SUMMARY

Biopiezoelectricity can be defined as the conversion from external mechanical force to induced biological electric pulse, and vice versa, the conversion from external electric field to induced tissue deformation. Nearly all biosystems exhibit biopiezoelectricity. This property may contribute to mechanical, biological and physiological behaviors of biomaterials in a way of intrinsic sensing and actuating mechanisms. Information of the functionalities and working mechanisms of biopiezoelectricity in living organisms are still scarce, especially at the nanoscale. Accompanied with biopiezoelectricity, some biomaterials also show bioferroelectric behaviors. Fundamentally, it is originated from switchable polarizations that are crystallographically preferred. Bioferroelectricity may contribute to energy storage and release in biosystems, and it may open a door for biomaterial-based storage device or biomimetic-based new materials for various applications, such as energy storage, and strengthening or toughening structural materials. However, the research into bioferroelectricity is still at its early stage. Therefore, the primary objective of this study is to systematically characterize the nanoscale biopiezoelectric and bioferroelectric properties of mollusk shell and to explore their potential functionalities in natural biomaterials. Mollusk shell is chosen because of their survival in billion years of natural selection, as well as their truly outstanding mechanical properties, and relatively simple composition and structure.

Main results herein are presented in four sections: structure and nanomechanical properties, biopiezoelectric properties, bioferroelectric

properties, and the effects of external factors (stress and temperature). The characterizations are mainly based on various Scanning Probe Microscopy (SPM) techniques. In particular, nanomechanical property of mollusk shell is quantified by Contact Resonance Force Microscopy (CR-FM). It provides true nanoscale mappings of local elasticity and energy dissipation of the scanned surface. In addition, biopiezoelectricity of mollusk shell is characterized by Piezoresponse Force Microscopy (PFM), which is a powerful branch technique of SPM to assess local piezoelectric behaviors of various materials. PFM provides information of strength of piezoresponse and polarization directions. Both vertical and lateral piezoresponse of polished fresh mollusk shell are studied in various orientations and locations. The piezoresponse is found to be originated from the biopolymers in mollusk shell. To confirm this, biopolymers-removed shells are also studied. Furthermore, bioferroelectric properties of mollusk shell are studied by using Switching Spectroscopy PFM (SS-PFM). Local deformation and polarization switching are recorded and can be combined to form ferroelectric hysteresis loop. Characteristic parameters, such as, coercive bias and imprint, can be extracted from the loop. Shell without biopolymers showed no ferroelectric behavior. Lastly, we also studied the responsive behaviors of biopiezoelectricity and bioferroelectricity of mollusk shell to the external stress and temperature. Moreover, the subsequent chapter presents some preliminary results of the piezoresponse of bone and the healing phenomena of mollusk shell. Based on all finding, the implications and significances of biopiezoelectricity and bioferroelectricity are proposed and discussed. Lastly, general conclusions and future research topics are proposed at the end of this dissertation.

LIST OF TABLES

LIST OF FIGURES

V_{ac} step. The mean heights of images (a)-(d) are -87.45 pm, -80.65 pm, -58.34 pm and -50.93 pm respectively.

Fig. 5.2 Three sets of DSHO fitted DART-PFM images of abalone shells.1st column (800×800 nm^2): observed from cross-sectional surface with one interlamellar biopolymer layer; 2nd and 3rd column (400×400 nm^2): observed from the interior and boundary of platelet on the nacre surface. (a) (d) and (g) are height images, (b) (e) and (h) are amplitude images, and (c) (f) and (i) are phase images. (probe: AC240TM, k_c = 2.37 N/m)

Fig. 5.3 Illustration of observing orientations and planes on both cross-sectional surface (a) and platelet surface (b).

Fig. 5.4 PFM images obtained at the inner surface of nacre (500×500 nm^2, 256×256 pixels). The two columns on the left-hand side are observed from the sample before rotation. The other two columns on the right-hand side are from the 90 ºrotated (counter-clockwise) same platelet. (a) and (b) the corresponding topographic images. The 2nd row are DART amplitude [(c) and (e)] and phase [(d) and (f)] images in the vertical direction. The 3rd row are the DART amplitude [(g) and (i)] and phase [(h) and (j)] images in the lateral direction. All of the amplitude images show the piezoresponse at 1 V_{ac}. Last row are the magnitude [(k) and (m)] and argument [(l) and (n)] images of vector-PFM in the x-z [(k) and (l)], and y-z [(m) and (n)] planes.

Fig. 5.5 Topographic and PFM images of deproteinated nacre surface. (a) Topographic image of the scanned platelet by tapping mode (7×7 μm^2, 512×512 pixels); (b) Topographic image where DART-VPFM [(c) and (d)] and DART-LPFM [(e) and (f)] are scanned (500×500 nm^2, 256×256 pixels); (c) and (e) are the amplitude images; (d) and (f) are the phase images.

Fig. 5.6 DART-VPFM [(b) and (c)] and -LPFM [(d) and (e)] images observed from the cross-sectional nacre surface (800 × 400 nm^2, 512 × 256 pixels). (a) height, (b) and (d) amplitude, (c) and (e) phase.

Fig. 5.7 DSHO fitted DART-PFM images of clam shell. The drive amplitude is 4 V_{ac} for all images. Images in the 1st (1×1 μm^2) and the 2nd (300×300 nm^2) column are observed on the outer surface of clam shell, while the images in the 3rd (300×300 nm^2) column are observed on the cross-sectional surface. The lines on Figs. (h) and (m) are to be explained on Fig. 5.4. (Probe: PPP-NCSTPt, k_c = 8.23 N/m)

Fig. 5.8 Data curves along line sections in Fig. 5.3(h) and (m). Data in 1st and 2nd columns are obtained from the cross-sectional shell surface and the outer shell surface respectively. (a) and (e) are height curves, (b) and (f) are amplitude curves, (c) and (g) are Q-factor curves, (d) and (h) are resonance frequency curves.

Fig. 5.9 The histograms of amplitude and phase data comparisons between fresh and bleached clamshell. Curves show data distributions from

LIST OF SYMBOLS

ϕ	Volume fraction of the piezoelectric sphere in a two phase spherical dispersion model
ε	Dielectric constant
χ	Damping of cantilever in free space
f_n^c	n^{th} mode of contact resonance frequency
Q_n^c	n^{th} mode of contact resonance quality factor
f_n^0	n^{th} mode of free resonance frequency
Q_n^0	n^{th} mode of free resonance quality factor
Q	Quality factor
A	Amplitude of piezoresponse
f_0	Cantilever free oscillation resonance frequency
f_1	First contact resonance frequency
φ	Phase of piezoresponse
d_{zz}^{eff}	Piezoelectric constant calculated from the amplitude that has not been fitted by DSHO model
d_{zz}	Piezoelectric constant defined by the deformation in the vertical direction induced by electric field in the same direction
L'	Tip location to the end of cantilever ($L-L_1$)
L_1	Tip position along cantilever length
L	Total length of cantilever
a_n	Real term in wavenumber function that represents the elastic tip-sample stiffness
b_n	Imaginary term in wavenumber function that represents the sample's viscous damping behavior
c	Elastic constant

d_c	Piezoelectric strain-constant of the piezoelectric sphere in a two phase spherical dispersion model
E_{chirp}	Linear chirp up electric drive signal
t	Time in second
V_{ac}	AC Drive amplitude
V_{dc}	DC biases
x_n	Real wavenumber under the elastic situation
m	Control parameter for chirp signal
α	Normalized tip-sample contact stiffness
β	Normalized damping coefficient
θ	Angle of sector cut for abalone sample under flexural stress
λ_n	Complex wavenumber for the viscoelastic equation
k_c	Cantilever stiffness

LIST OF ABBREVIATIONS

AC	Alternating Current
AC-mode	An operation mode of Scanning Probe Microscopy technique, in which cantilever oscillates mechanically to detect the topography and surface properties.
AFM	Atomic Force Microscopy
AM-AFM	Amplitude Modulated Atomic Force Microscopy
BE	Band Excitation
$CaCO_3$	Calcium Carbonate
CNTR	Calcite-Nacre Transition Region
CPD	Contact Potential Difference
CR-FM	Contact Resonance - Force Microscopy
CSM	Continuous Stiffness Measurement
DART	Dual AC Resonance Tracking
DC	Direct Current
DI	Deionized
DSHO	Damped Simple Harmonic Oscillation
DTA	Differential Thermal Analysis
EDTA	Ethylenediaminetetraacetic acid
FE	Finite Element
FeRAMs	Nonvolatile Ferroelectric Memories
FESEM	Field Emission Scanning Electron Microscope
HV	High Voltage
ICDD	International Center for Diffraction Data
IMRE	Institute of Materials Research and Engineering
JCPDS	Joint Committee on Powder Diffraction Standards
KPFM	Kelvin Probe Force Microscopy
LPFM	Lateral Piezoresponse Force Microscopy
MEMS	Microelectromechanical Systems

NaOH	Sodium Hydroxide
PFM	Piezoresponse Force Microscopy
PR	Piezoresponse
PVDF	Polyvinylidene Difluoride
P(VDF-CTFE)	Poly(vinylidene Difluoride chlorotrifluoroethylene)
SiC	Silicon Carbide
SPM	Scanning Probe Force Microscopy
SSPFM	Switching Spectroscopy Piezoresponse Force Microscopy
TGA	Thermogravimetric Analysis
VPFM	Vertical Piezoresponse Force Microscopy

Chapter 1

Introduction

CHAPTER 1 Introduction

This chapter defines the scope and describes the background of the research works to be discussed in this thesis. The research motivations and objectives, as well as the thesis outline are also provided.

1.1 Overview of the Piezoelectric and Ferroelectric Behaviors of Natural Materials

Through billion years of natural selection, the survived species need to progressively evolve their functionalities to adapt to the changing environment. Many of their functions and properties are genuinely coveted by the engineering world, for example, the toughness of spider silk, the strength and lightweight of bamboos or the adhesion abilities of the gecko's feet, which are typical examples of high performance natural materials (Barthelat, 2007). Biomimetics is a broad scientific field that examines natural biological systems and attempts to design systems and synthetic materials through biomimicry (Rao, 2003). Nature usually makes economic use of materials by optimizing the design of the entire structure or system to meet the needs of the multiple functionalities. The studies of natural materials can inspire engineers and scientists to develop new generation of synthetic materials and systems. The first step of biomimetic approach is to identify materials properties of natural systems and to understand the underlining mechanisms that promote these properties.

Structures and properties of variety of natural materials have been extensively characterized from macroscale to molecular level since 1950s,

including plants, flies, insects, mollusks, vertebrates, and many others (2010). However, many functional properties of the natural materials are still not fully understood, and biopiezoelectricity is one of them. In short, piezoelectricity or electromechanical (EM) coupling is a material behavior that involves the conversion between mechanical energy and electrical energy. It is widely accepted that virtually all biological systems manifest a mechanical response to an applied bias (Rodriguez et al., 2008). The effects and roles of piezoelectricity in biological systems have been studied and applied in many clinical trials, such as electrically-stimulated bone remodeling, massage therapy, and chiropractic. The significance of piezoelectricity in biological tissues has been pointed out by Bassett (1968). Theoretically, the piezoelectricity may affect the cell migration and proliferation, orientation of inter- and intra-cellular macromolecules, enzyme activation and suppression and many other physiological phenomena. Recently, the piezoelectric and ferroelectric biomaterials have been proposed with potential applications on tissue engineering and molecular ferroelectrics attributed to their advantages over the conventional inorganic ferroelectrics, for instance, they can be flexible, biodegradable, cost effective, and self-assembled (Bystrov et al., 2012; Heredia et al., 2012; Sencadas et al., 2012). However, due to the complexity of the systems and the highly multidisciplinary nature of the research, the mechanisms of the piezoresponse in biological systems are not fully understood and the detail information of biopiezoelectricity and bioferroelectricity are still scarce (Bystrov et al., 2012). Therefore, it is both scientifically and technologically significant to study the piezoelectric and

ferroelectric phenomena in biological systems, and exploit their characteristics for engineering and biomedical applications.

Among various biomaterials, much attention has been paid on hard/mineralized biomaterials, including mollusk shells, bone and teeth, because of their self-regeneration properties and distinctive hierarchical structures that promote extraordinary mechanical properties. Most of the previous studies on piezoelectricity of mineralized biomaterials are on the macroscale tissue level (Fukada, 1968b; Fukada and Ueda, 1970; Marino, Becker and Soderholm, 1971; Ando, Fukada and Glimcher, 1977). On the other hand, with the development of Piezoresponse Force Microscopy (PFM), one of the functional modes of Scanning Probe Microscopy (SPM) technique, the studies of the piezoelectric and ferroelectric behaviors of biomaterials at the nanoscale resolution have become feasible (Rodriguez et al., 2006b; Kalinin et al., 2007a; Bystrov et al., 2012).

1.2 SPM Technology and Its Applications on Natural Materials

SPM is the most common non-destructive technique to observe structure and diverse properties of various materials at the nanoscale. SPM examines materials by using a probe with super-sharp tip apex. The applied mechanical contact force commonly ranges from a few nanonewtons to a few micronewtons. Therefore, SPM can have atomic resolution and is virtually non-destructive. SPM consists of many operational modes, for instance, Atomic Force Microscopy (AFM), Kelvin Probe Force Microscopy (KPFM), Magnetic Force Microscopy (MFM), and many more. Local topographic,

mechanical, electrical, magnetic, and chemical properties can be studied via the corresponding SPM techniques.

In recent years, SPM techniques are greatly applied in biosystems researches mainly in terms of visualizing the surface, measuring physical properties, and being a manipulation tool in biology, for example, examination of the mechanical properties of biotool tissues (e.g. teeth and claws), force measurement of receptor-ligand interaction on living cells, nano-structuration and nano-imaging of biomolecules for biosensors, and many more (Martelet et al., 2007; Eibl, 2009; Schöberl, Jäger and Lichtenegger, 2009). On the other hand, PFM is the primary tool to investigate the piezoelectric and ferroelectric properties of various advanced materials, including biomaterials. However, such researches on natural materials are still at a nascent stage. The studies of biopiezoelectricity and bioferroelectricity are mainly conducted on bones (Halperin et al., 2004; Minary-Jolandan and Yu, 2010) and organic polymers [e.g. collagen and Polyvinylidene Difluoride (PVDF)] (Fukada, 2000). There are also some studies on cell (Kalinin et al., 2007b) and teeth (Habelitz et al., 2007; Wang et al., 2007). Nevertheless, the roles of piezoelectricity and ferroelectricity in biosystems are mysterious, and the information related to biopiezoelectricity and bioferroelectricity is still scarce, especially at the nanoscale.

1.3 Objective and Motivation

As described earlier, EM coupling is a near-universal phenomenon shared among all biological systems (Kalinin, Rar and Jesse, 2006). The main motivation to study piezoelectricity in biological systems is to explore and

understand the relationships between physiologically generated electric field and various properties at the molecular, cellular, and tissue levels (Gruverman, Rodriguez and Kalinin, 2007). Furthermore, it has been proposed that the EM coupling, via mechanical stress that generates an electric potential, controls the mechanisms of local tissue development (Kalinin et al., 2006c). It could be the origin of bone remodeling, tissue regeneration, neuron reaction and many other physiological phenomena. The ultimate purpose in this research field is to help to predict and to manipulate biomaterial behaviors, and may also develop new synthetic materials via biomimicry, but it is a long journey ahead. For this particular research work, the primary objective is to characterize the fundamental piezoelectric and ferroelectric properties of mollusk shells, and to correlate these properties to their structural, mechanical, and physiological behaviors. In addition, the micro- to nano-scale hierarchical structures of the shells, and the nanoscale elasticity are also to be studied.

Mollusk shell is a calcified biological system that exhibits substantially superior mechanical properties than those of its individual constituents. It has hierarchical structure formed under environmental conditions. Hungering for similar extraordinary properties, some synthetic nanocomposites have been developed by scientists in a way to mimick the hierarchical structure of mollusk shell (Tang et al., 2002). However, the overall performance cannot be compared to that of the natural mollusk shell. Hence, it is reasonable to speculate that some other factors, such as the electromechanical interactions at different structural levels, may play important roles, not only in the organized functionality of biosystems, but also the outstanding mechanical properties of natural calcified materials. Therefore, a comprehensive understanding of the

working mechanisms of these natural biological systems is required in order to develop a new generation of composite materials, which may be self-organized, light weight, high strength and toughness, as well as biocompatible.

1.4 Thesis Outline

This thesis consists of nine chapters. Chapter 1 provides a brief overview and evolution of the studies of piezoelectric and ferroelectric properties in natural materials. In addition, an introduction of SPM technique and the motivations and objectives of this research work are also included. In Chapter 2, literatures closely relevant to this dissertation are reviewed in details in three aspects, including biopiezoelectricity and bioferroelectricity, mollusk shell properties, and various modes of SPM technique. Chapter 3 provides the details of the experimental methods and parameters used for this study. The major results in this dissertation are presented in Chapters 4 to 7, including nanoscale structure and mechanical properties of abalone and clam shells; piezoelectric properties of mollusk shell; ferroelectric behaviors of mollusk shell; and responsive behaviors of mollusk shell under external flexural stress and rising temperature. Based on the reviewed literatures and all of the observations from this study, the implications and significances of biopiezoelectricity and bioferroelectricity are proposed in Chapter 8. Lastly, Chapter 9 provides a general conclusion of the research work, as well as the recommended succeeding works.

Chapter 2

Literature Review

CHAPTER 2 Literature Review

This chapter provides necessary background for better understanding of the subsequent chapters. Three most relevant aspects, including biopiezoelectricity and bioferroelectricity, fundamental properties of mollusk shell, and scanning probe microscopy techniques will be explained in details. In addition, as many key terms related to EM coupling are used throughout the thesis, those related terms are found in Appendix A.

2.1 Biopiezoelectricity and Bioferroelectricity

Electromechanical (EM) coupling is a kind of material behavior that converts electrical impulse to mechanical action, or coverts mechanical stress to voltage. It comprises properties of piezoelectricity, ferroelectricity, pyroelectricity, ionic channel, etc. Piezoelectricity is a fundamental property of biological tissues. It may be account for many biological phenomena such as bone remodeling, the formation of thrombi due to injury of blood vessels and all tactual responses (Shamos and Lavine, 1967). This property of some biological materials has been studied continuously, for example, wood (Fukada, 1968a), bone (Aschero et al., 1996), collagen (Goes et al., 1999), tooth (Kalinin et al., 2005) and lobster apodeme (Fukada, 1995), as well as some organic biopolymers having large molecule and complex structure; such as cellulose, collagen, keratin, chitin, amylose and DNA (Gruverman, Rodriguez and Kalinin, 2007). Permanent and induced electric dipoles can be easily found within these organic biopolymers. Comparing to the mineral crystals with centrosymmetric crystal structure, the oriented biopolymer

molecules are therefore thought to be responsible for the piezoelectricity in biological materials (Gruverman, Rodriguez and Kalinin, 2007). The piezoelectricity apparently stems from a shearing stress on the oriented long chain fibrous molecules, the actual effect being a displacement of charge due to the distortion of cross-linkages in the molecular structure (Shamos and Lavine, 1967). Furthermore, Fukada (1995) pointed out that the origin of piezoelectricity was from the internal rotation of dipoles such as CO-NH and CO-O based on the study of synthetic polypeptides and optically active polymers. However, comparing with the traditional inorganic piezoelectric materials, the piezoelectric constants of the biological materials are generally small (Table 2.1). Hence, the induced deformation or polarization is limited, but it is sufficient for various physiological functions.

Table 2.1 Shear piezoelectric constant of various biopolymers. Reprinted from Fukada (1995)

		$-d_{14}$ (pC/N)
Polysaccharide		
Cellulose	wood	0.1
	ramie	0.2
Chitin	crab shell	0.2
	lobster apodeme (demineralized)	1.5
Amylose	starch	2.0
Proteins		
Collagen	bone	0.2
	tendon	2.0
	skin	0.2
Keratin	wool	0.1
	horn	1.8
Fibrin	elongated films of fibrinogen-thrombin clot	0.2
Deoxyribonucleic acids	salmon DNA (at -100° C)	0.07
Quartz Crystal	d_{11} = 2.2 pC/N	

There are many factors that may influence the piezoresponse of biological systems. Water content is one of such significant factors. Based on the study of decalcified bovine bone (Maeda and Fukada, 1982), when water content in the collagen fibrils was beyond a critical value, the piezoelectric constant of bone was reduced. Collagen is the major organic contents in bone and it is a macromolecule consisting of polypeptides organized in the form of a triple helix. The triple helix is stabilized by hydrogen bonds and polypeptides chains. By introducing a small amount of water, the crystallinity of collagen is increased due to the additional interchain hydrogen bonds from water molecule. If the water content is large, the density of piezoelectrically effective dipoles is also reduced because of the expansion between the triple helix and microfibrils that induced by adsorbed water. It is generally believed that piezoelectric constant reduces with increasing water content due to the induced ionic current that neutralizes the piezoelectric polarization.

To the best of knowledge, only one earlier study has elaborated on the piezoelectricity of mollusk shell (Ando, Fukada and Glimcher, 1977), which was conducted on lobster shell. Instead of collagen in bone, the major biopolymer of the invertebrates is chitin. When shear force is imposed in an oriented plane of chitin molecules, polarization is produced in a direction perpendicular to the plane. The obtained highest piezoelectric strain constant d_{14} (shear polarization generated by normal stress) was reported to be 4×10^{-8} cgsesu (~13.34×10^{-18} C/m) from demineralized apodeme. The variations of the piezoelectric and dielectric constant with temperature and hydration were also studied. Increments in both piezoelectric and dielectric constants were observed at -100 ℃ and 100 ℃ of 5% moisture content sample. With a high

moisture content, the piezoelectric and dielectric constants were generally reduced with temperature. A two phase spherical dispersion model has been developed to explain such temperature dependent phenomenon (Fukada and Date, 1973), in which piezoelectric spheres were uniformly distributed in a non-piezoelectric medium. The piezoelectric constant is:

$$d = \phi d_c \frac{5c_2}{3c_1 + 2c_2} \times \frac{3\varepsilon_1}{2\varepsilon_1 + \varepsilon_2} \qquad \text{(E2.1)}$$

where ϕ is the volume fraction of the sphere, d_c is the piezoelectric strain-constant of the sphere, c and ε are elastic constants and dielectric constants respectively. The subscripts 1 and 2 indicate the corresponding values of sphere and medium. When the temperature of specimen increased from -150 ℃ to -100 ℃, the thermal liberation of the local molecular motion of chitin in medium caused increment in ε_1 and decrement in c_1, which resulted in a total increase of d value (assume the rest parameters are temperature independent). When temperature further increased to 100 ℃, the measured ε_1 was dramatically increased; this led to the increase of d value. Nevertheless, if moisture content was high, as temperature was increasing, the mobility of water which is adsorbed on the surface of the crystalline region was increased. This generated a rise of surface conductivity neutralizing the piezoelectric polarization. The resultant increased ε_2 under this condition gave a very small d value (Fukada, 1995).

2.2 Properties of Mollusk Shells

Mollusk is one of the most ancient species that still persist today. Their armors or shells protect them from predators in billions of years of evolution.

These shells self-organize in an aqueous environment and under ambient conditions (Heinemann et al., 2011). The shells are composed by readily available nontoxic elements: about 95 wt.% minerals (calcium carbonate: $CaCO_3$) and less than 5 wt.% biopolymers. The biopolymers are mainly polysaccharide and proteins (Li et al., 2004). The mollusk shells are formed via biomineralization process, during which site-directed and region-specific nucleations occur with regulation of the growth, structure, morphology and orientation of the mineral crystals (Rao, 2003). The whole process is regulated by the biopolymer contents.

More importantly, mollusk shell is an excellent example of high performance natural nanocomposite. They are about 500~1000 times tougher than that of the abiogenic counterparts such as geological calcite and aragonite (Fig. 2.1), with only a slight reduction in the stiffness (Barthelat, Rim and Espinosa, 2009). It has been found that the high performance of mollusk shells is mainly originated from their hierarchical structures.

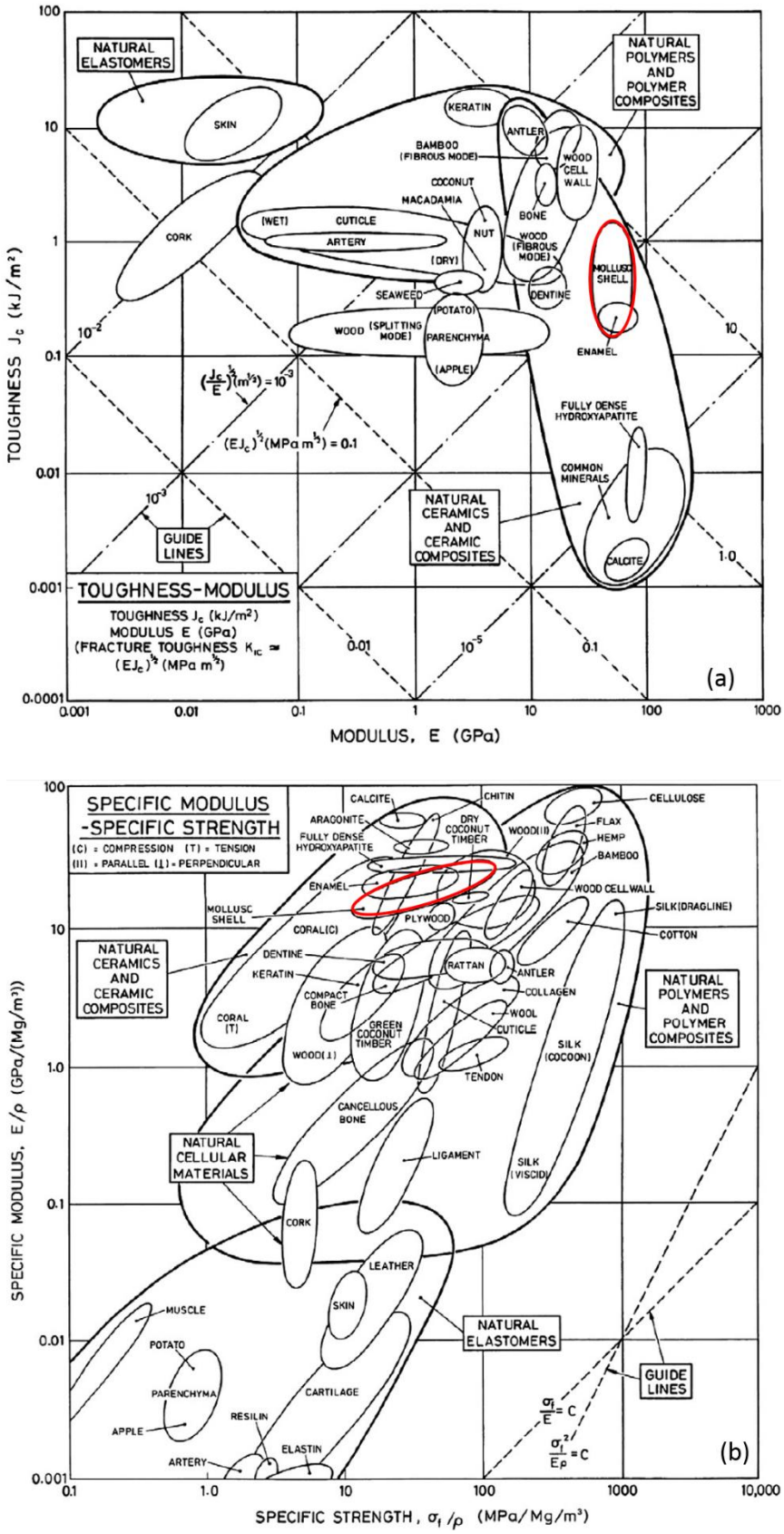

Fig. 2.1 Materials properties map for a variety of natural materials. (a) toughness & Modulus chart, (b) specific Modulus & Specific Strength chart. Reproduced from Heinemann et al. (2011)

Mollusk shells have a variety of structures as illustrated in Fig. 2.2, including prismatic, foliated and cross lamellar structure, columnar, and sheet nacre. These structures usually have two to three orders of hierarchies from nano- to micro-scale in a way of embedded $CaCO_3$ crystals in organic matrix or biopolymers (Ji and Gao, 2010). The distinct composition and hierarchical structure promote the superior mechanical properties of mollusk shells. Based on the mechanical tests on 20 different species of mollusk shells, the elastic modulus of mollusk shells was reported ranging from 40~70 GPa, while their tensile strength is in the range of 20~120 MPa (Currey and Taylor, 1974; Barthelat, Rim and Espinosa, 2009). Therefore, mollusk shells are important models for new generation of sustainable materials, which is lightweight, tough and with high strength. Amongst all of the structures found in mollusk shells, nacre appears to be the strongest and the most widely studied one. It is the major structure found in abalone shells, which is to be studied in this work.

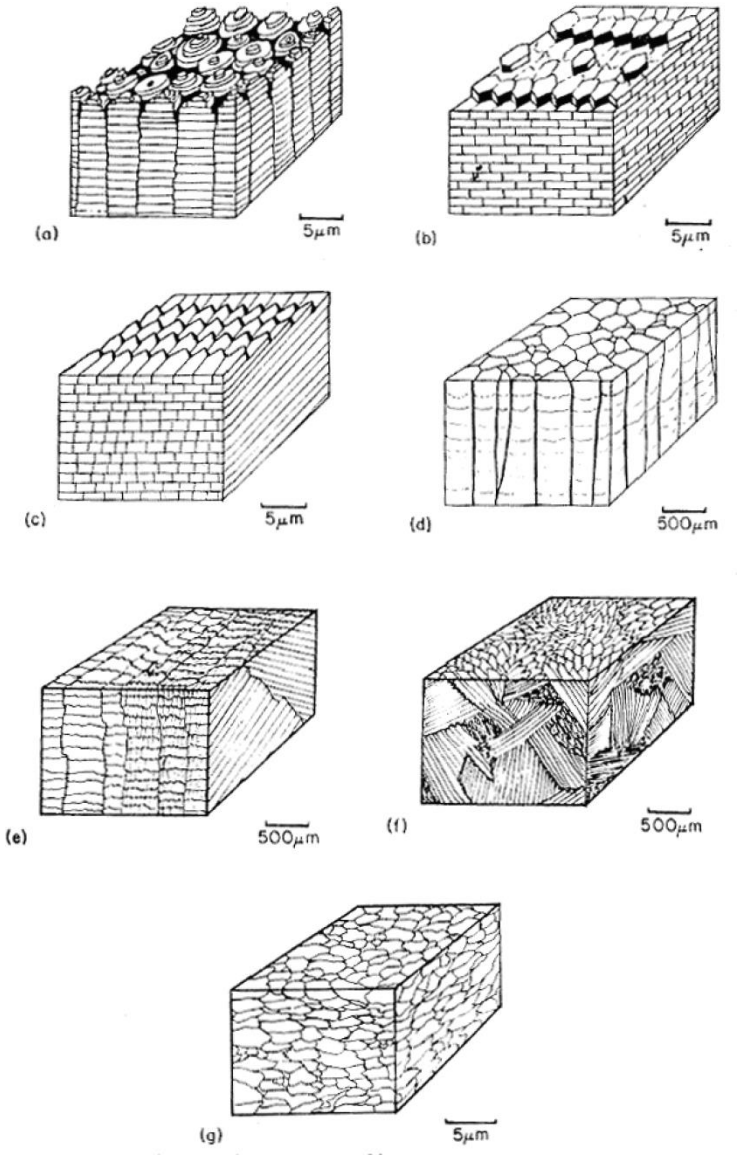

Fig. 2.2 Mineral structures found in mollusk shells. (a) columnar nacre, (b) sheet nacre, (c) foliated, (d) prismatic, (e) cross-Lamellar, (f) complex cross-laminar, (g) homogeneous. Reproduced from Currey and Taylor (1974).

2.2.1 Abalone shell

Abalone belongs to the Gastropoda class, which is the largest class of mollusks. Abalone shell is composed of 95 wt.% $CaCO_3$, about 5 wt.% biopolymers, and a small amount of water. Macroscopically, abalone shell can be divided into two sections: the outer calcite (rhombohedral) section and the inner aragonite (orthorhombic) section (Fig. 2.3).

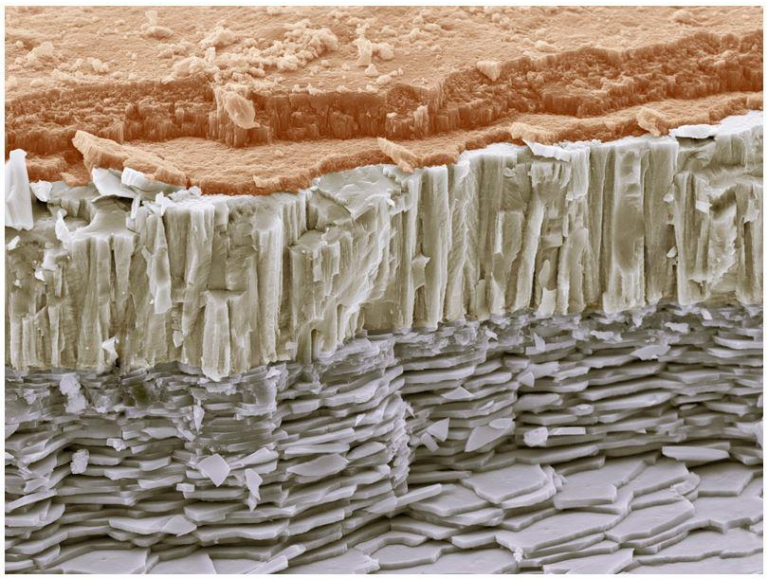

Fig. 2.3 Cross-section of the abalone seashell, illustrating the deliberate spatial and orientational control of $CaCO_3$ reinforcing elements in a unique 3D architecture. (Copyrights: Science Photo Library / keystone). Retrieved from: http://www.ethlife.ethz.ch/archive_articles/120113_drei_d_komposit_cho/index_EN

The aragonite section is composed by closely packed platelets and forms a lamellar structure, i.e. the nacreous structure. The platelets are 300~500 nm in thickness and 5~15 μm in width. The basic building blocks of the platelets are a large number of mineral nanograins (~ 44±23 nm size) that imbedded inside a continuous organic matrix (intracrystalline biopolymers) (Rousseau et al., 2005). The thickness of the intracrystalline biopolymers is found to be about 4 nm (Stempfléet al., 2010). Thus, the platelet basically is an organomineral nanocomposite, instead of a homogenous single crystal composed by nanograins only (Towe and Hamilton, 1968; Stempfléet al., 2010). Furthermore, on the surface of platelets, two or three nanograins are found to form nanoscale asperities in the size of about 100 nm. The interlocking of these asperities is believed to be one of the contributors to the outstanding fracture toughness of nacre (Li et al., 2004). When viewed from

the cross-sectional surface, the mineral layers are joined by thin layers (~20 nm) of interlamellar biopolymers (Katti, Katti and Mohanty, 2010), and this is usually called “bricks and mortar” structure. The continuous crystal regions between the two adjacent mineral layers form the mineral bridges. They penetrate through the biopolymer layers, and are believed to be the origin of the perfect c-axis alignment of the aragonite crystal from the adjacent mineral layers (Meyers et al., 2008). The polygonal platelets in the same mineral layer usually have different sizes and number of edges. Misorientations between these platelets usually exists, i.e., the rotation about the c-axis, and they were found to be connected by the {110} twin planes of orthorhombic lattice (Sarikaya et al., 1990; Heuer et al., 1992). In addition, there are intertabular biopolymers located between the side walls of the platelets in the same mineral layer (Heinemann et al., 2011; Launspach et al., 2012).

On the other hand, the outer calcite section is composed of the prismatic crystal columns/blocks that are enveloped in the interprismatic matrix (Nudelman et al., 2007). The columns are orientated perpendicular to the shell surface. Generally, the exact composition and size of structures depend on shell age and biomineralization environmental conditions.

The biopolymers presented in nacre is composed of chitin (polysaccharide) and different kinds of proteins, such as perlucin, perlwapin, AP8 and perlinhibin (Marin and Luquet, 2004; Launspach et al., 2012). The interlamellar matrix comprises a porous chitin filaments sheet and the associated proteins. Some of these proteins are tightly bonded to the chitin core, while others are dissolvable by weak acetic acid. Moreover, the intertabular matrix is found to be the thin proteinacious sheets that contain

collagen. Furthermore, the soluble proteins encased into the mineral crystals inside a single platelet are the intracrystalline biopolymers (Heinemann et al., 2011; Launspach et al., 2012). Nevertheless, the full understanding of the combination of proteins in a particular shell species is still under development. The exact locations, orientations, and cross-linkings of these biopolymers are uncertain. The organic biopolymers are believed to function as the "glue" that joins the mineral crystals together and to facilitate the motion of aragonite crystals under external stresses. Thus, it plays the key role in the improvement of the strength and toughness of abalone shell.

Based on the knowledge of nacre structure, synthetic materials have been developed, but it still cannot achieve the levels of toughness (in relative to their constituents) of the natural abalone shell (Katti, Katti and Mohanty, 2010). It may be due to the limitations of the synthesis technique, but it also bring the possibility that the mechanisms other than hierarchical structure and mechanical aspect may also be involved in the toughening mechanisms (Li and Zeng, 2011; Li and Zeng, 2013), and the piezoelectric and ferroelectric properties of the nacre may be one of the contributing toughening mechanisms.

2.2.2 Clam Shell

Clam shell belongs to the Bivalvia class, which is the 2nd largest class of mollusks. The published information about structures and compositions of clam shell is not as many as those of abalone shell. Clam shell has more complex structure than that of the abalone shell. Two distinct regions can be easily visually identified, the outer white region and the inner translucent

region. The outer region is composed of layers of compact aragonite needles which are arranged cross-lamellarly and are separated by thin organic matrix. The angle between needles in neighboring layers is about 120 °. A single needle is made up of smaller sub-grain phase with size of 10~20 nm and some amorphous substance (Zhu et al., 2006). In the inner region of giant clam shell, micro-layered structure is also observed but is composed by long columnar aragonite crystals. Many flaws in form of microcracks are contained in this region (Lin, Meyers and Vecchio, 2006).

In term of organic phase, both tubular and banded organic matrices are revealed after chemical treatment. The tube-like organic matrix is Ethylenediaminetetraacetic acid (EDTA) insoluble and is evenly distributed in the entire clam shell. The tubes penetrate through the layers and act similarly to the canaliculus fibers in the mollusk shell. Generally speaking, clam shell has less ordered and more isotropic structure than that of the abalone shell.

2.2.3 Mechanical Properties of Mollusk Shell

Large number of researches have been conducted in order to determine the mechanical properties, including hardness, fracture strength and elastic modulus of various species of mollusk shells, especially of the abalone shell. Because of the variations in the testing methods and sample conditions, the discrepancy among the results is large. There are many factors contributed to the large variation of the mechanical properties, which can be generally divided into two categories. One is the experimental setup, such as loading rate, tensile or compressive test, and the loading direction relative to the layer orientations in the mollusk shells. The other is the shell conditions such as age,

growth and storage environment, as well as the water content in the shell samples.

However, the common finding is that the mechanical property of mollusk shell is dramatically improved in spite of the weak constituents. The Young's moduli of the dry and wet nacres (i.e., the brick and mortar structure) were reported to be 70 GPa and 60 GPa respectively, and the tensile strengths of dry and wet nacres were found to be 170 MPa and 140 MPa. Furthermore, the work of fracture of nacre was found in a range of 350 to 1240 J/m^2 (Jackson, Vincent and Turner, 1988), which is about 500-3000 times higher than that of the geological aragonite (Jackson, Vincent and Turner, 1990; Rao, 2003; Lin and Meyers, 2005). In addition, comparing to that of the abalone shell, clam shell has higher hardness but weaker compressive strength (Lin, Meyers and Vecchio, 2006; Zhu et al., 2006).

The mystery of the toughening of nacre has also been widely studied. For example, a summary of the toughening mechanisms was provided by Katti, Katti and Mohanty (2010), including the viscoelastic deformation of the mineral platelets (Mohanty et al., 2006), the presence of nano-asperities and mineral bridges that improves the frictional resistance (Wang et al., 2001; Song, Soh and Bai, 2003), the unfolding of protein domains and breaking of crosslinks in organic macromolecules upon tensile stress (Smith et al., 1999), crack blunting and bridging by the ligaments of organic phases (Wang et al., 1995; Sumitomo et al., 2008), and some others.

2.3 Scanning Probe Microscopy

Different from the optical and electronic microscopy techniques, SPM uses mechanical force to sense surface morphology. The sensing is via a probe that typically comprises a substrate, a cantilever and a sharp tip [Fig. 2.4(a)]. The cantilever is usually tens to hundreds of micrometers long. One end of the cantilever is fixed with the substrate. At the free end of the cantilever, the sharp tip is mounted below. The tip is the media directly contact or interact with the sample surface. As the tip radius ranges from a few nanometers to tens of nanometers, the interaction between the tip and sample is usually confined within a few atoms or molecules. The atomic force between tip and sample or the sample response is detected by the tip and transmitted through the cantilever deflection. The deflection is recorded by a laser-detector system, as illustrated in Fig. 2.4(b). Through the years of development, SPM now comprises a numbers of techniques to reveal not only the topography, but also various surface and subsurface properties on the atomic- to nano-scale. All of these techniques are based on the fundamental principles of SPM. Following sections will discuss the details of the techniques used in this research work.

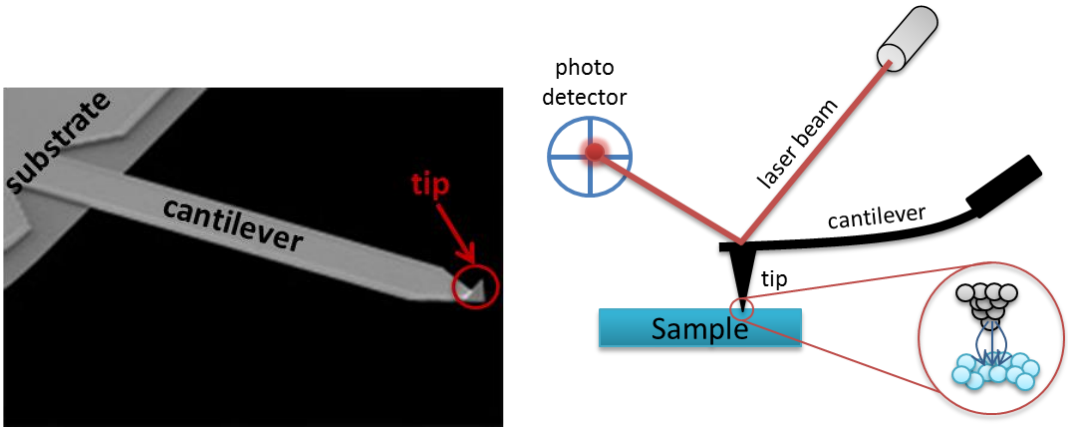

Fig. 2.4 (a) example of SPM Probe (AC240TM), retrieved from http://www.asylumresearch.com/Probe/AC240TM,Olympus, (b) schematic of SPM working principle.

2.3.1 Atomic Force Microscopy (AFM)

AFM is the most fundamental mode of the SPM. Its primary function is to acquire three-dimensional (3D) sample topography of the surface at the nanoscale resolution. AFM can be operated in either amplitude-modulated (AM) or frequency-modulated (FM) mode. In this study, only the AM-AFM is used. It works based on two mechanisms: contact mode and tapping mode (also called AC-mode). Under contact mode, topography is tracked by maintaining constant force between the tip and sample when scanning the surface line by line. The base of cantilever or the substrate is adjusted up or down to maintain the set point force, which is accomplished by a feedback loop control.

On the other hand, tapping mode or AC-mode uses different principle. Instead of steady contact with the sample surface, cantilever is oscillating with predefined drive amplitude and drive frequency when scanning over the sample surface. This mode is accomplished by mechanically exciting the substrate of cantilever by a piezo-crystal, and maintaining a set point amplitude. The responsive amplitude and phase signals due to tip-sample interaction are detected and recorded by monitoring cantilever deflection. Besides the topography, material property variations can be revealed in the phase image (Garcia et al., 1999; Tamayo and Garcia, 1998). Due to the nature of tapping mode, both tip and sample can be better preserved; smaller force can be detected; and material properties can be revealed in more details. More information about AFM is nicely introduced by Eaton and West (2010).

2.3.2 Contact Resonance Force Microscopy (CR-FM)

The most promising AFM methods for quantitative measurements of relatively stiff materials are dynamic approaches, in which the cantilever is vibrated at or near its resonant frequency (Hurley, 2010). CR-FM is the general name of these techniques. Different from nanoindentation experiments, which gives elastic modulus as an average value over the entire sample surface, CR-FM shows high-resolution image of elasticity mapping of a scanned area on the nanoscale. For highly nonhomogeneous materials, like seashell, CR-FM can provide more meaningful modulus mappings rather than a single averaged modulus value. In addition, CR-FM has been recently applied to polymer composites to quantitatively reveal both elastic/storage modulus and loss/dissipative modulus (Killgore et al., 2011a; Killgore et al., 2011b; Yablon et al., 2012).

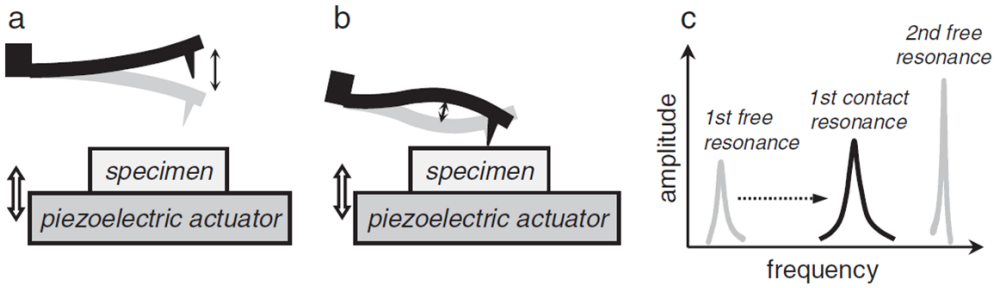

Fig. 2.5 Concept of CR-FM. (a) resonant mode of the cantilever is excited by a piezoelectric actuator when the tip is in free space, (b) cantilever in contact with a specimen under an applied static force, (c) resonance spectra. Reproduced from Hurley (2009).

Generally speaking, CR-FM measures the frequencies at which the free and contact resonances occur. Mechanical properties of samples can be deduced from the measured frequencies incorporated with two models: the dynamic motion of cantilever and the tip-sample contact mechanics (Hurley, 2010). The concept of CR-FM is illustrated in Fig. 2.5. A resonator is placed

below the tested sample to initiate the ultrasonic oscillation. The CR-FM measurement involves many precautions and procedures. Firstly, cantilever has to be calibrated to determine the sensitivity and spring constant, and thus to know the exact static force F_N applied to the tip. When testing stiff materials, F_N is typically in the range of several hundred nanonewtons to a few micronewtons. Such forces ensure the elastic contact between the tip and sample. Secondly, reference material with known elastic modulus is necessary for elastic properties quantification. The reference material needs to have the similar stiffness to the testing sample. Thirdly, due to the relatively large contact force, the tip can be easily blunted, in which case the contact radius between the tip and sample will change along with the scanning process (Killgore, Geiss and Hurley, 2011). Thus, the reference material needs to be examined at least twice, before and after the sample was tested. Finally, the adherence between the sample and piezo-actuator has to be strong enough. Otherwise, more than one contact resonance peaks may be shown on the frequency spectrum. CR-FM can be conducted at a single point or over a defined area. Because the analysis relies on the contact resonance frequency at each data point, the frequency tracking is necessary. Dual-AC Resonance Tracking (DART) is one of the methods to trace shifts of contact resonance frequency that is caused by surface roughness or property difference (Rodriguez et al., 2007). The details of DART method is going to be introduced in section 2.3.4. In the experiments, CR-FM measurement obtains four types of experimental data, *free* resonance frequency and quality factor, and *contact* resonance frequency and quality factor. These data are required for further analysis.

For data analysis, value of storage modulus depends on the contact resonance frequency, while the loss modulus depends more on both the frequency and the quality factor of the resonance spectrum (Yablon et al., 2012). By modeling the dynamic motion of the cantilever and tip-sample contact mechanics by using Kelvin-Voigt model, the normalized tip-sample contact stiffness α and damping coefficient β can be calculated from the following formula:

$$\alpha + i\beta(\lambda_n L_1)^2 = \frac{(2/3)(\lambda_n L_1)^3(1+\cos\lambda_n L\cosh\lambda_n L)}{[(\sinh\lambda_n L_1\cos\lambda_n L_1 - \sin\lambda_n L_1\cosh\lambda_n L_1)(1+\cos\lambda_n L^{'}\cosh\lambda_n L^{'}) + (1-\cos\lambda_n L_1\cosh\lambda_n L_1)(\sin\lambda_n L^{'}\cosh\lambda_n L^{'} - \cos\lambda_n L^{'}\sinh\lambda_n L^{'})]} \quad \text{(E2.2)}$$

where "n" indicates the nth flexural eigenmode of cantilever dynamics, and $\lambda_n L = a_n + ib_n$ is a normalized complex wavenumber ($a_n = x_n^0 L(f_n^c / f_n^0)^{1/2}$, $b_n = a_n[(2\pi f_n^c - \chi Q_n^c)/8\pi f_n^c Q_n^c]$). L is the total length of the cantilever, and tip location is expressed by L' when measured from the free end of the cantilever, and $L_1 = L - L'$. $x_n^0 L$ is the correspondence root of the characteristic equation for free flexural vibration, and equals to 1.8751, 4.6941, and 7.8548 for the first three modes. In addition, the damping of the cantilever in free space is expressed as $\chi = 2\pi f_n^0 / Q_n^0$ (Killgore et al., 2011b). The above analysis method applies to both tested sample and reference material. Based on the calibrated constants α_{cal} and β_{cal}, which are calculated from the reference material, the reduced storage modulus $E^{'R} = E^{'R}_{cal}(\alpha/\alpha_{cal})^{3/2}$ and the reduced loss modulus $E^{''R} = E^{''R}_{cal}(f_n^c\beta / f_{n\,cal}^c\beta_{cal})^{3/2}$ for the tested sample can be determined based on the sphere-plane Hertzian contact model.

2.3.3 Piezoresponse Force Microscopy (PFM)

PFM is another operational mode of SPM technique and it is a key tool for probing EM coupling phenomena on the nanoscale (Rodriguez et al., 2006a; Soergel, 2011). It works according to the reverse piezoelectricity principle, i.e., the surface of a piezoelectric material will oscillate mechanically in accordance to the applied AC bias. The bias is applied via a conductive probe usually with a Pt-coated silicon tip. Because of its extremely high resolution (on the molecular scale), reliable quantitative results, ability to study local piezoresponse, ease of implementation, and nondestructive nature, PFM has been extensively applied to microelectromechanical systems (MEMS), nonvolatile ferroelectric memories (FeRAMs) and many other ferroelectric materials in the form of bulks or thin films to study, for instance, ferroelectric switching, spectroscopy, domain dynamic and domain writing behaviors (Christman et al., 2000; Gautier et al., 2002; Rodriguez et al., 2002; Kalinin, Karapetian and Kachanov, 2004; Gruverman and Kalinin, 2006; Kalinin, Rar and Jesse, 2006; Kholkin et al., 2007). Furthermore, PFM has a dramatic contribution to the characterization of electromechanics of biological systems. Instead of a traditional high voltage macroscopic measurement on the bulk specimens, PFM is able to investigate even single molecule with a much lower voltage, such as millivolts. PFM allows high resolution imaging of biological systems and the differentiations between organic and mineral components. PFM based research on piezoelectricity of many mineralized hard tissue such as teeth and bones (Halperin et al., 2004; Habelitz et al., 2007), and soft organic materials such as isolated biopolymers and virus (Kalinin et al., 2006a; Majid and Yu, 2009) have been published in recent

years. As mentioned earlier, mollusk shell has overall prominent mechanical properties compared to each microconstituent. However, the synthetic materials cannot reach the level of toughness of natural mollusk shell by simply biomimicking the structures of mollusk shell. Under this circumstance, the universal biopiezoelectricity and bioferroelectricity in biomaterials may play a role in the toughening mechanisms or even other physiological behaviors in mollusk shell. Therefore, it is reasonable and necessary to characterize the nanoscale piezoelectric and ferroelectric behaviors of the mollusk shell by PFM, which has not been conducted and reported in the literatures so far.

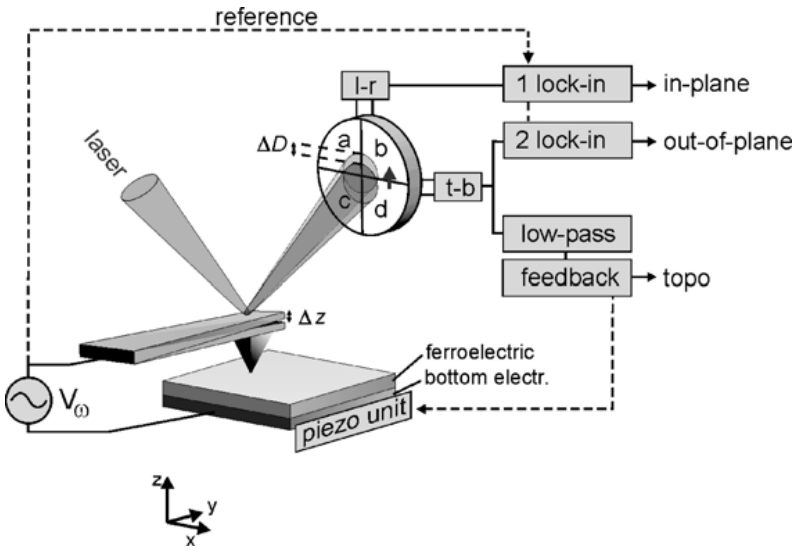

Fig. 2.6 Standard PFM experimental setup. Reproduced from Kholkin et al. (2007).

The standard experimental setup of PFM is illustrated in Fig. 2.6. It is usually based on a commercial scanning probe microscope equipped with a four-quadrant photo detector, a conductive cantilever tip, a function generator, and two lock-in amplifiers. Application of AC electric bias to the conductive

tip results in a local oscillation of sample surface due to the converse piezoelectric effect, which is detected by cantilever deflections. The deflections cause the accordance laser shifting on the photo detector. Electronic feedback facilitates accurate tracking of the cantilever deflections caused by sample oscillations by using the lock-in technique with simultaneous recording of the surface topography. Both out-of-plane (vertical PFM) and in-plane (lateral PFM) components of the electromechanical responses can be obtained from photo detector regions of (a+b)-(c+d) and (a+c)-(b+d), respectively (Fig. 2.6). Output signals generate at least two images, amplitude and phase images. Amplitude image represents the distribution of piezoelectric response strength, while phase image shows the polarization directions distribution, in other words the domain structure. In addition, the surface morphology can be viewed in the normal topographic images. The details of the PFM principle are available in many literatures (Kalinin, Karapetian and Kachanov, 2004; Kalinin et al., 2010; Soergel, 2011). PFM allows high resolution imaging of biological systems and differentiation between the organic and mineral components in a non-destructive way. It thus can provide additional important information on the microstructure of the biological materials (Gruverman, Rodriguez and Kalinin, 2007).

2.3.4 Dual AC Resonance Tracking (DART)

The primary use of DART is to locate the contact resonance frequencies during the scanning even when the frequencies shift due to the surface roughness. DART simultaneously uses two different drive frequencies (f_1, f_2) to scan: f_1 is below (or on the left hand side) the frequency tuning peak,

and f_2 is above (or on the right-hand-side) it (Fig. 2.7). The cantilever responses, including amplitudes (A_1, A_2) and phases (ϕ_1, ϕ_2) are collected at these two frequencies. In addition, the drive frequencies are chosen such that the measured amplitudes A_1 and A_2 are equal. The contact resonance frequency shift is tracked by moving these two frequencies to maintain a similar amplitude value at them, i.e., $\Delta A = A_1 - A_2 = 0$, and also maintain a constant $\Delta f = f_2 - f_1$ (Gannepalli et al., 2011).

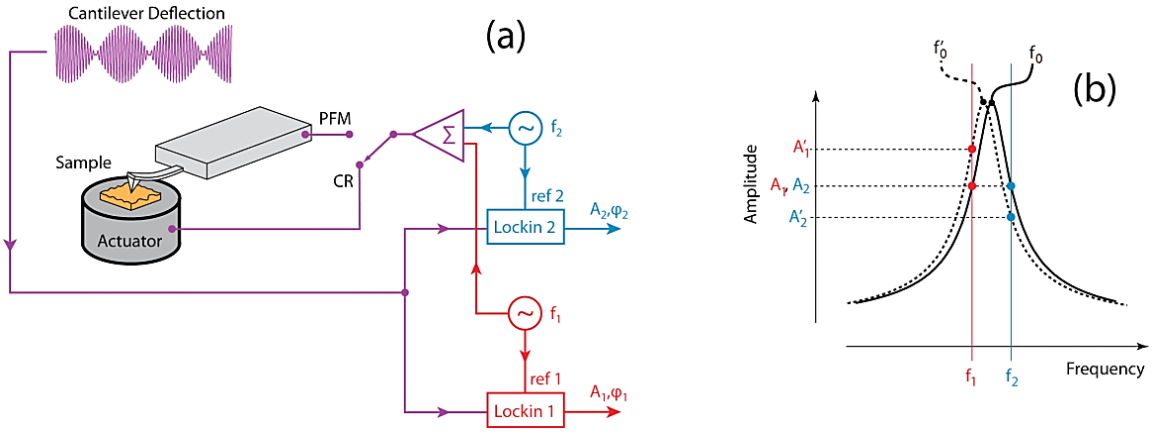

Fig. 2.7 Principle of DART method. Reproduced from Gannepelli et al (2011).

In case of DART-PFM, the obtained raw responses are directly from the cantilever other than the sample itself, and the cantilever motion is driven by the oscillation of sample according to the inverse-piezoelectricity. The electric field induced sample oscillation or response (A_{drive}, φ_{drive}) can be extracted by fitting the raw response data to the damped (simple) harmonic oscillator (DHO or DSHO) model.

The dynamics of the AFM cantilever tip can be generally approximated using the simple harmonic oscillator (SHO) model, which is appropriate for modeling single-eigenmode characterization when the tip-

sample interactions do not significantly perturb the oscillation (García and Pérez, 2002; Kareem and Solares, 2012). When encountering tip-sample interaction, there is usually energy dissipation or loss, which can be represented by adding a dash-pot or damper to the SHO model, i.e., the DSHO model. In this model, the responsive amplitude and phase of cantilever oscillation can be expressed by the formulas (Gannepalli et al., 2011):

$$A(f) = \frac{{f_0}^2 A_{drive}}{\sqrt{({f_0}^2 - f^2)^2 + (f_0 f / Q)^2}} \quad \text{(E2.3)}$$

and

$$\varphi(f) = \tan^{-1} \frac{f_0 f}{Q({f_0}^2 - f^2)} + \varphi_{drive} \quad \text{(E2.4)}$$

By solving these two equations, four unknown parameters, including sample response ($A_{drive}, \varphi_{drive}$), contact resonance frequency f_0, and energy dissipation Q can be extracted uniquely from the four known variables from the cantilever oscillation ($A_1, A_2, \varphi_1, \varphi_2$). Therefore, the piezoresponse of sample surface can be quantified by the DART-PFM technique.

2.3.5 Band Excitation (BE)

Similar to the DART method, BE method can be used to track the frequency shift during the SPM scanning. In addition, BE allows the decoupling between conservative and dissipative tip-sample interactions and identifying the non-linear responses. It can also eliminate topographic cross-talk (Jesse et al., 2010). This technique excites and detects response at all frequencies within a specified frequency band (usually 20~40 kHz) simultaneously, in which the resonance frequency is roughly located in the

center of this frequency region (Jesse and Kalinin, 2011) (Fig. 2.8). Under the operation of BE, cantilever oscillations are recorded at hundreds of frequency intervals within the frequency band, the responsive amplitude and phase data can be fitted within the whole frequency spectrum. Thus, the contact resonance frequencies can be identified unambiguously for each scanned data point. Any change of the contact resonance frequency can be detected within this band. Most importantly, because of the usage of multiple frequencies, more data can be recorded and used for the high-quality DSHO fitting, i.e., fit the cantilever amplitude response to a Lorentzian curve (equivalent to E2.3) (Rodriguez et al., 2010; Kareem and Solares, 2012), in order to extract the real sample deformation. Same as those from DART-PFM method, four types of images can be extracted from BE-PFM method: amplitude (response strength), phase angle (polarization direction), Q-factor (relative dissipative energy), and contact resonance frequency (conservative tip-sample response that reveals relative stiffness) (Jesse and Kalinin, 2011).

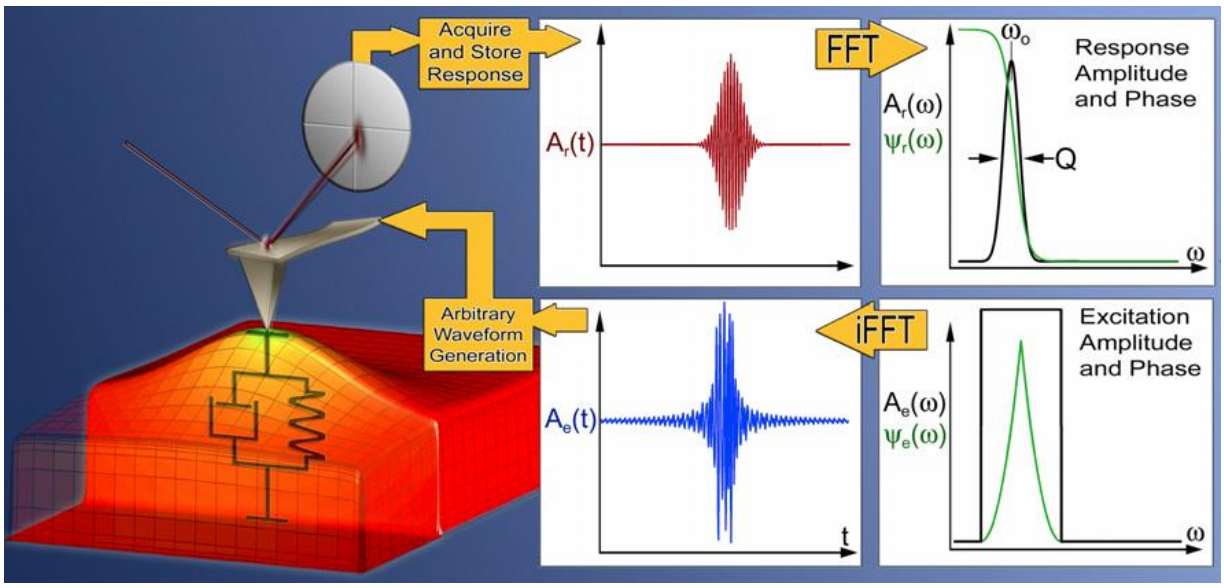

Fig. 2.8 Principle of BE method. Reproduced from Jesse et al. (2007).

More specifically, in BE-PFM method, the frequency (f), location (x, y) dependent amplitude (A) and phase response (φ) are collected and stored in a 3D data arrays as {A, φ}(x, y, f). The data stored in the time domain are Fourier transformed to the data expressed in frequency domain (Fig. 2.8). The saved data at each pixel are then fitted by the DSHO model to acquire the 2D images of the piezoresponse amplitude, the phase offset angle, the Q-factor, and the contact resonance frequency. The detailed working principles of BE technique can be found in some of the recent publications (Jesse et al., 2007; Nikiforov et al., 2010; Jesse and Kalinin, 2011).

2.3.6 Switching Spectroscopy PFM (SS-PFM)

SS-PFM is the technique to acquire local ferroelectric hysteresis loops at a single point on sample surface. In addition, an SS-PFM map can also be generated over M × M mesh points in a defined region. This technique provides the information about the local polarization dynamics and also reveal the pinning, internal field, energy loss and much more information based on the shapes and characteristic parameters of the hysteresis loops.

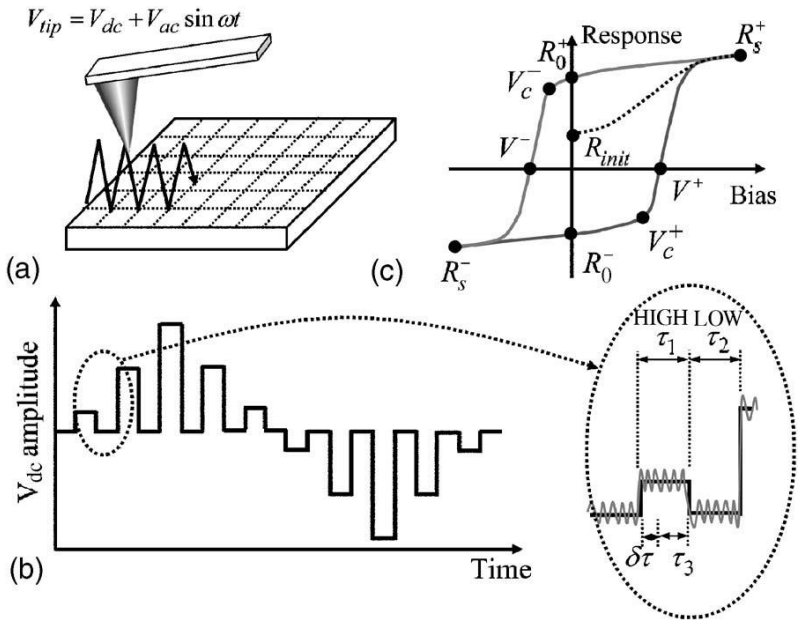

Fig. 2.9 Switching and driving waveforms of SS-PFM. (a) electric signal supplied to tip, (b) one cycle of triangular square wave, (c) typical PR hysteresis loop. Reproduced from Jesse, Baddorf and Kalinin (2006).

Fig. 2.9 illustrates the switching and probing waveforms in the SS-PFM measurement. The drive signal involves a DC and an AC voltage. The most commonly used DC drive is the triangular square wave as shown in Fig. 2.9(b). The AC signal is imposed in the DC drive to detect the real-time piezoresponse. Usually, the remanent responses, i.e. responses at DC-off pulses, are used to calculate the hysteresis loop. The raw data from SS-PFM are amplitude and phase. The piezoresponse (PR) is calculated with the relation of PR = A $\times \cos(\varphi)$. The typical hysteresis loop of PR versus bias is shown in Fig. 2.9(c). From this loop, many critical parameters describing the switching process can be extracted and analyzed, including positive and negative coercive biases (V^+ and V^-), remanent piezoresponses (R_0^+ and R_0^-), imprint voltages, saturation piezoresponse, nucleation bias and work of switching. More details of SS-PFM analysis are presented in the literature (Kalinin et al., 2010).

Chapter 3

Materials and Methods

CHAPTER 3 Materials and Methods

This chapter describes specific sample preparation methods for individual characterization. Experimental setups and procedures are provided. However, for SPM techniques, the operational parameters vary between the experiments. Thus, essential details of experimental parameters will be provided in the corresponding chapters.

3.1 Sample Preparation

Abalone shell and clam shell were chosen for this study. They were selected for this research project mainly for three reasons. Firstly, by comparing to some other shells, abalone shell shows higher compressive and flexure strengths, while clam shell has higher microhardness (Lin, Meyers and Vecchio, 2006; Zhu et al., 2006). Secondly, they represent two common classes of seashells, i.e. monoplacophora and bivalvia. Finally, both kinds of shells are readily available.

In this study, fresh mollusks were purchased from seafood market. Shucked shells were stored in tap water under ambient conditions. All of the characterizations were conducted on three kinds of surfaces of mollusk shell: the outer shell surface (connected to outside environment), the inner shell surface (connected to living organism), and the cross-sectional surface, as illustrated in Fig. 3.1.

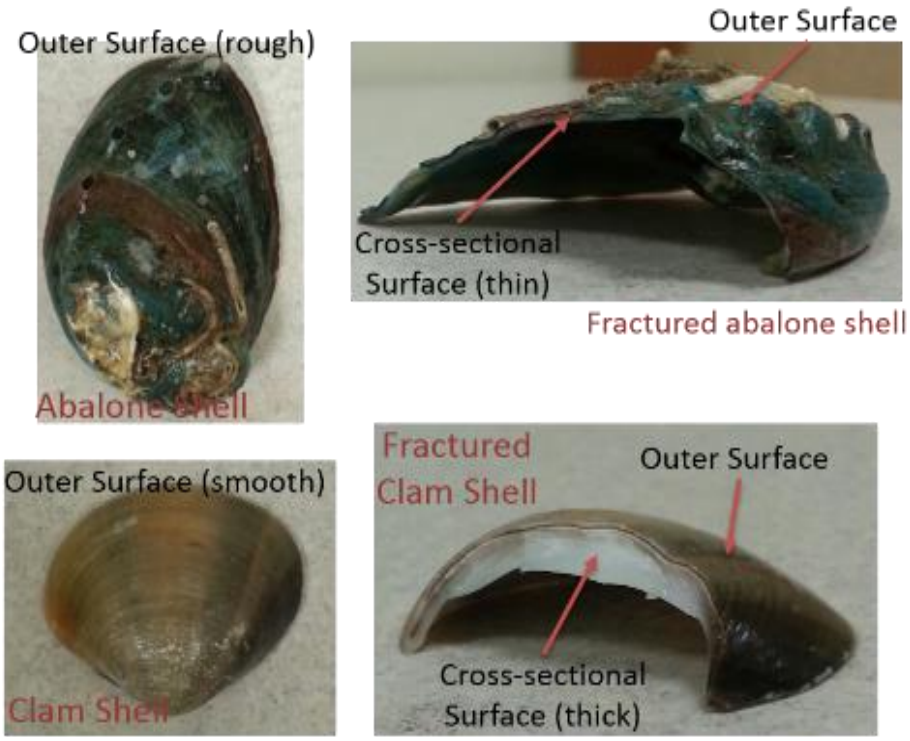

Fig. 3.1 Illustrations of abalone and clam shells and the surfaces studied in this work.

3.1.1 Mechanical Polishing

To observe a decent SPM image, sample needs to be polished to obtain a flat and low roughness surface. Two cases were involved for sample preparation. The first case is that when sample size is not confined by SPM space. Fresh shell was either cut or fractured to small pieces. These pieces were then casted in epoxy resin under ambient conditions. Solidified casted samples were in cylindrical shape with a diameter of 30 mm. After that, samples were progressively grinded with 1200, 2400, and 4000 SiC papers by water-cooled semi-auto polisher (Struers LaboForce-3, Denmark). Followed by this, samples were polished with 0.3 and 0.05 μm alumina powder. Finally, fine polished samples were sonicated in deionized (DI) water to remove any residual polishing powders or loosen materials. Then the samples were air-

blown dried, and ready for various SPM characterizations. On the other hand, if sample size is confined by scanning space of a particular SPM mode, the initially cut small pieces of shell samples cannot be embedded in epoxy resin. Thus, they are hand-polished in the same procedures as described above. In this study, the hand-polished samples are only for the 3D-PFM, high-voltage (HV) SS-PFM and heating experiments, where the shell-in-epoxy samples cannot fit in the sample holder or cannot resist the high temperature.

3.1.2 Chemical Treatment

To verify the functionalities of each micro-constituent, $CaCO_3$ and biopolymers, in mollusk shells, chemical solutions were used to partially remove either $CaCO_3$ or biopolymers. To remove $CaCO_3$, 0.5 M Ethylenediaminetetraacetic acid (EDTA) was used (Pokroy and Zolotoyabko, 2003). On the other hand, 4% NaOH was used to remove biopolymers (Tao et al., 2009). The amount of the removed micro-constituents depends on the duration that samples are immersed inside the solutions. To retain sample integrity and reasonable surface smoothness for SPM observation, only the materials on and slightly below the sample surface were partially removed by sonicating in respective solutions for about 15 minutes. The samples were then thoroughly rinsed by DI water and air-blown dried after chemical treatment.

3.1.3 Special Preparation for In-Situ SPM Characterization under Flexural Stresses

Only the cross-sectional abalone shells were tested by this method due to the set-up of the experiment. To study the in-situ response of the abalone

shell under the external flexural stresses, the shell was cut into small rectangular pieces by using a water-cooled diamond slicing blade. The rectangle pieces were casted in epoxy resin. The solidified samples were in a cylindrical shape, with a 40 mm of diameter and at least 10 mm of height. In order to ground the mollusk shell under PFM and SS-PFM modes, the rectangular shell pieces need to be cut to the height more than 10 mm such that after poling process, shell can exposed on both top and bottom surfaces of the casted sample. Both the upper and lower surfaces of the cylinder were grinded flat using #1200 SiC paper. To apply flexural stresses, two slots were cut in the epoxy mount. One was a sector cut with an initial opening angle of 60 °-65 °, and the other was a rectangular cut to help deliver more stress to the embedded abalone shell by only a small deformation of the epoxy resin. Flexural forces were applied by a home-made fixture as described in section 3.2. After cutting slots, the samples were undergone the same grinding, polishing, and cleaning steps as described in the section 3.1.1.

3.2 Bending Fixture and Stress Calculation for In-Situ SPM Characterization under Flexural Stresses

To apply flexural stresses to the abalone shell samples, a simple fixture was designed and fabricated. The fixture is a metal ring with 10 mm of height and 40 mm of inner diameter, so that the polished sample as described in the section 3.1.3 can just fit in it. Two holes were made through the ring wall so that two point-forces can be applied by tightening screws against the edge of sample. Fig. 3.2 schematically shows the top view of the setup, including the metal ring and the shell sample casted in epoxy resin. When force is applied

via tightening of the two screws, the sector cut will be closed accordingly. The change of the sector cut angle ($\Delta\theta$) is an indicator of the applied stress. This change is about 1 °in maximum because of constraints from the metal ring and the resistibility of the epoxy resin to the point force (a large point force can break the epoxy at the point of contact). This setup has the advantages of low cost and easy operation. No precision cutting of the specimen is required, which is usually difficult for thin abalone shells. More importantly, the fixture can be easily fitted into the confined space below the SPM head with the system we used. The effects of both tensile and compressive stresses on nacre can be studied simultaneously from the same sample.

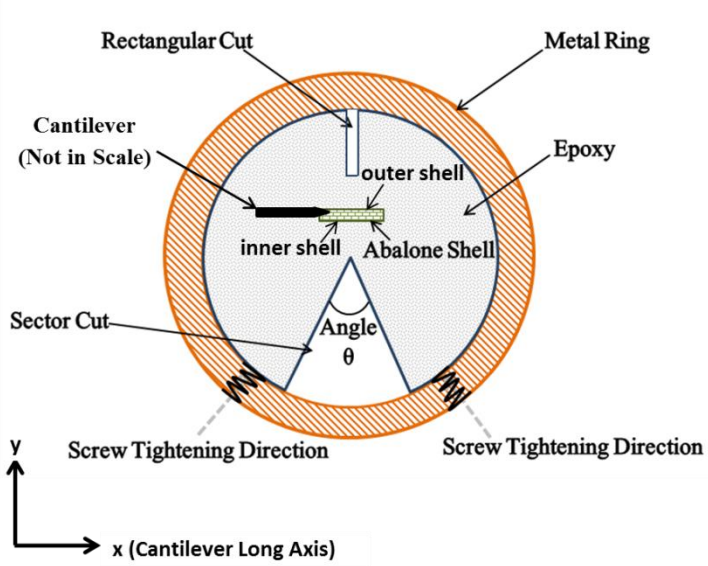

Fig. 3.2 Illustration of setup for flexural stress application to abalone shell.

A numerical method is used to provide a guideline of the stress distribution of the cross-sectional nacre in abalone shell, and help to determine the approximate locations of the neutral axis (stress-free), tensile, and compressive stresses for SPM image and analysis. The stress was calculated by the finite element (FE) simulations using the commercial software

ABAQUS. The exact geometries arising from the experimental setup were used in the FE model. As the exact dimensions of the samples and mountings may differ, such as the initial opening angle and shell thickness, therefore, each sample was measured explicitly for its own FE calculations. During the FE simulation, the boundary conditions applied to the model were: (1) the center of the epoxy plate is fixed to reduce the rigid motion; (2) loading is imposed to the notch at the lower side of plate under displacement-controlled conditions. Upon stress exertion, within the shell structure, the soft biopolymer will deform first and the hard mineral nanograins may remain unchanged. It can be very complex if the responses of different constituents are calculated separately. Therefore, the nacre is treated as a homogeneous integrated body. In addition, both the epoxy plate and abalone shell sample were considered to be linear elastic due to the very small deformation ($\leq 1°$) in the experiments. This is sufficient to provide the estimation of the locations where the tensile and compressive stresses are exerted. Table 3.1 summarized the detailed material parameters used for simulations.

Table 3.1 Materials properties used in the calculation

	Young's Modulus, E (GPa)	**Poisson's Ratio, υ**
Epoxy	3.66	0.36
Abalone Shell	70 (Meyers et al., 2008)	0.32 (Song et al., 2008)

In the FE calculations, the epoxy plate and abalone shell sample were both modeled with three-node linear triangular elements (C2D3). The sizes of the elements in the vicinity of the notch-tip area were refined carefully because of the strong stress gradient. Furthermore, to accurately capture the stress variation, the size of the elements within the sample was set to be 1/12

times of the sample thickness. The validation and convergence of the mesh size described above were confirmed in the simulations. The stress distribution was found to change linearly with the position in the shell cross-section. The neutral axis is near the central line of the cross-section. In other words, the outermost shell exhibits the maximum tensile stress while the innermost shell exhibits the maximum compressive stress (refers to Fig. 3.2). The tensile stress can reach to about 150 MPa at the outer shell surface and the compressive stress can reach to 140 MPa at the inner shell surface. Nevertheless, the stress state of the nacre sample can be multi-axial during the application of loading. However, the stress components including shear stress and the axial stress in y-direction were found to be much smaller than that of the axial stress in x-direction, especially in the middle region of sample. Therefore, in this work, only the axial stress component was employed to confirm the neutral axis. Fig. 3.3 shows the complete stress distribution with $\Delta\theta \approx 1^{o}$ at different positions of the cross-sectional surface of nacre. This setup was then placed inside the SPM machine for in-situ piezoelectric and ferroelectric studies.

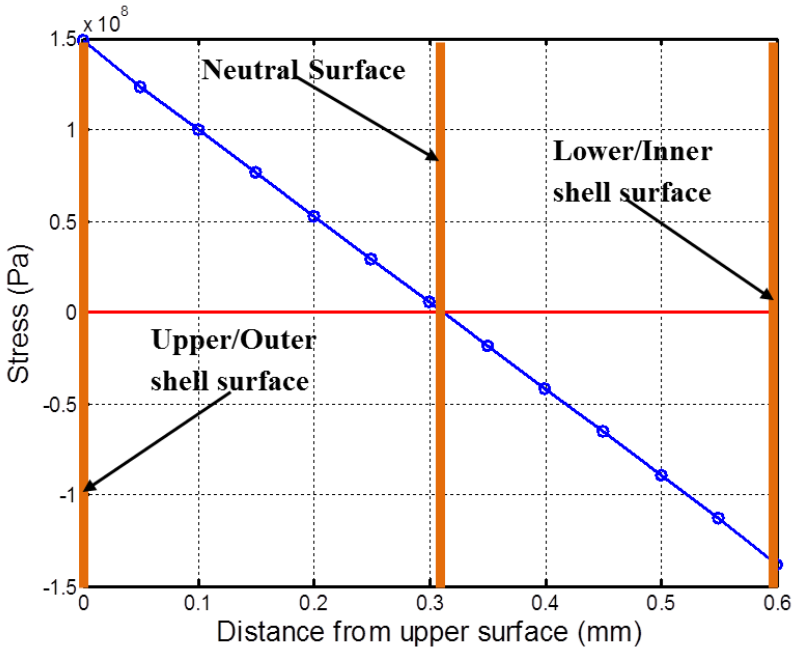

Fig. 3.3 Stress distribution on the cross-sectional abalone shell sample surface determined by FE computation. The curve is displayed as stress vs. positions, while the position is measured with respect to the upper/outer shell surface.

3.3 Morphology Characterization

3.3.1 Field Emission Scanning Electron Microscopy (FE-SEM)

FE-SEM is a vastly used characterization tool to observe surface morphologies of various kinds of materials. It works in a way of shooting electrons to a conductive surface and secondary or backscattered electrons are collected by detector and form images. For this study, as the mollusk shells are isolators, each sample was coated with a thin gold film by a gold sputter (JEOL JFC 1200, Japan) before the observation by using FE-SEM (Hitachi 4300, Japan). Two kinds of surface were studied: polished and fractured. The polished surface was flat and smooth, which leads to little or no contrast in the images. To overcome this difficulty, the polished surface was sonicated in EDTA solution for about 15 minutes to remove partial of the $CaCO_3$ on sample surface (Pokroy and Zolotoyabko, 2003). The sample was then

thoroughly rinsed by DI water. By this method, shell microstructure was revealed clearly. On the other hand, the fractured surface was easily obtained by either hand breaking or impacting fracture of the shells.

3.3.2 AFM

AFM is usually the primary choice to observe high resolution nanoscale image of surface morphology. A commercial AFM (MPF-3D, Asylum Research, US) was used for this observation. AC-mode or tapping mode was used in experiments to preserve both sample and tip. This mode also has higher resolution than that of the contact mode. Besides topography, AC-mode generates a phase image that represents the tip-sample energy dissipation. Under the AC-mode, repulsive regime (phase angle < 90 °) was usually maintained. Scan speed was varied between 0.5~2 Hz. As mollusk shell samples have hard surfaces, the probe for AC-mode scanning was chosen with nominal stiffness of either 7.4 N/m (PPP-NCSTPt, Nanosensors, Switzerland) or 42N/m (NCHPt, Nanosensors, Switzerland).

3.4 Mechanical Properties Characterization

3.4.1 Microhardness Test

Indentations by microhardness tester (Shimadzu HMV-2) were used primarily for two purposes. First is to measure the microhardness of mollusk shell in various location and orientations. Second is to make defects on sample surface for shell healing studies. For this test, the loading duration was 15 seconds and indenting force was in the range of 98.07 mN~4.90 N.

3.4.2 CR-FM

CR-FM is a powerful technique to quantify true nanoscale mechanical properties of a material in a nondestructive way, which is unachievable by other techniques. In this study, the elasticity mapping of the abalone shell was obtained by this method. Magnesium and silicon dioxide were chosen as reference materials because these two materials have the same order of stiffness as that of the abalone shell. The elastic moduli of reference materials were characterized by nanoindentation CSM tests (serviced by Institute of Materials Research and Engineering, Singapore). Scanning was conducted by a silicon probe (AC200TS, Olympus, Japan) whose nominal stiffness is 9.7 N/m and tip radius is 9±2 nm. For this probe, the tip is located just at the end of the cantilever. Its first resonance in air is around 157 kHz, and Q-factor is around 328. Each set of experiments was started with cantilever calibration by an improved thermal noise method (Proksch et al., 2004), and followed with examination of reference materials. After that, shell sample was tested, and finally reference materials were examined again. Contact forces between the tip and sample were maintained at 100~200 nN. After collecting necessary data, the quantification of local elastic modulus of abalone shell was accomplished by the method proposed by Killgore et al. (2011b). The configuration used in the experiment is that the oscillation is supplied from a resonator underneath the sample. Contact stiffness and contact damping are firstly converted from contact resonance frequencies of the cantilever. Afterwards, the reduced elastic modulus is calculated from contact stiffness based on Hertzian contact model. By assuming tip properties, the Young's

modulus of sample can be calculated. For the measurement in this study, all of the data were collected at the first contact resonance frequency.

3.5 Nanoscale Piezoelectric Properties Characterization by PFM

3.5.1 Domain Imaging

PFM is one particular mode of the commercial AFM as mentioned earlier. It is used to scan images which reveal piezoresponse variations in the area. Images were scanned near the contact resonance frequency to amplify the detectable signals. To closely track the contact resonance frequency shifts caused by surface roughness, DART method (Gannepalli et al., 2011) is usually used. For 2D or 3D PFM images, to ensure the corresponding locations of vertical and lateral piezoresponse, single frequency PFM is used due to the limited number of data channels. The requirement of good contact resonance frequency tracking in PFM usually leads to slow scan rate (0.5 Hz or even slower). Finally, DSHO fitting was applied to PFM raw images to transfer the detected response of cantilever to the true response of sample surface. The pixels that cannot be fitted by the DSHO approach are highlighted by red color. Probe used for PFM observation has conductive tip. Cantilever with nominal stiffness of 7.4 N/m (PPP-NCSTPt, Nanosensors, Switzerland) was chosen. To clearly observe nano-domains, scan size for PFM measurement was usually less than $2\times2\ \mu m^2$. Resolution is either 256×256 or 512×512 pixels, depending on the scan size or size of the smallest feature of sample.

3.5.2 Piezoelectric Constant d_{zz}

Piezoelectric constant d_{zz} is an indicator of the strength of piezoelectricity of a material (the extent of vertical deformation induced by electric field in the same direction). Two different methods were adopted to characterize this value. One was based on image, and the other was based on single point observation (scan size < tip radius). Both methods required PFM imaging with gradual increment of drive amplitude V_{ac}, i.e. the AC electric field applied to sample surface. The corresponding sample responsive amplitudes (mechanical deformation in the unit of pm) were plotted against the AC voltages. The slope of this curve, which is expected to be linear, was the value of d_{zz} of which the dimension is pm/V. In addition, if the cantilever was calibrated (known sensitivity) before PFM imaging, the calculated d_{zz} can be quantified by the DSHO fitting. Otherwise, only semi-quantified effective d_{zz}^{eff} can be obtained because of the convoluted magnifying factor with the amplitude.

3.5.3 BE-PFM imaging

BE is the method using a frequency band to closely track the shift of contact resonance frequency. Combined with PFM, local piezoresponse, polarization orientation, relative stiffness, and relative energy loss can be quantified. It works in the way exactly same as the normal PFM, except that the drive signal has multiple frequencies. In this study, an exponential chirp waveform with 512 waveform points was used as the excitation signal. Chirp is one of the most common band excitation signals (Fig. 3.4). It is defined as:

$$E_{chirp} = \sin(mt^2) \quad \text{(E3.1)}$$

where E_{chirp} is the band excitation electric drive signal, m is the control parameter in units of rad/s^2, and t is the time measured in second.

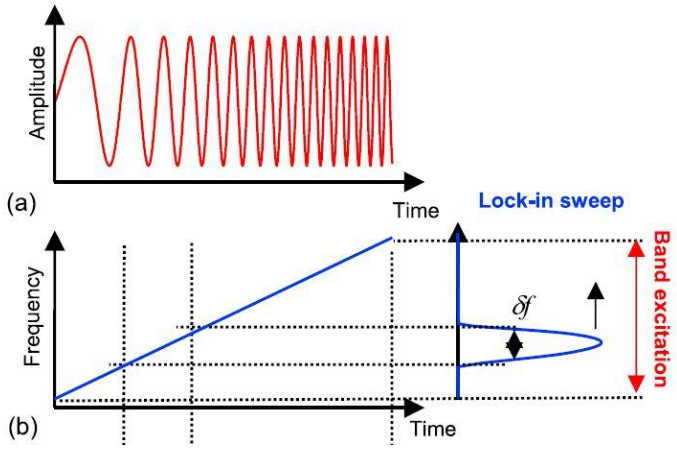

Fig. 3.4 (a) Chirp excitation signal that can be represented as a sinusoidal excitation (in time domain), (b) with linearly varying frequency (in the frequency domain after Fourier transformation). Reproduced from Jesse et al. (2007).

In practice, chirp signals are modified such that they gradually increase and decrease in amplitude by multiplying an envelope function, in order to prevent any artificial peaks caused by the sharp oscillations in the frequency spectrum, especially near the frequency cutoff at the signals used in the BE method (Fig. 3.5) (Kareem and Solares, 2012). In this study, the excitation bandwidth was 20 kHz. Thus, the drive frequency range was fixed around 700 ~ 720 kHz. Drive amplitude was 4 V_{ac}.

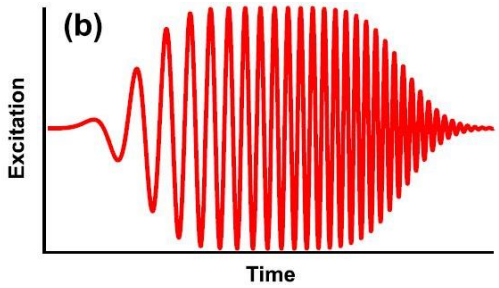

Fig. 3.5 Example of chirp function modified by envelop function in practice.

3.6 Local Ferroelectric Hysteresis Loop Observation by SS-PFM

SS-PFM is an advanced PFM technique to acquire ferroelectric hysteresis loops locally. The probe used for this technique need to be conductive and flexible enough. Thus, conductive cantilever with nominal stiffness of 2 N/m (AC240TM, Olympus, Japan) was used. A high-voltage attachment (maximum ±220 V) is required to supply voltage higher than 10 V. The proper value of bias window depends on material and sample orientation. The DC electric pulse is triangle-square wave as described by Jesse, Baddorf, and Kalinin (2006). The time duration of each square pulse was 24.5 ms, and one complete triangle cycle took 10 seconds. Each bias cycle started at 0 V_{dc}, and at least two cycles were recorded at each location. Remanent (DC bias off) ferroelectric hysteresis loops were recorded and studied.

3.7 Thermogravimetric Analysis (TGA) and Differential Thermal Analysis (DTA)

Thermal analysis is a technique to detect inter/intra-molecular interactions of a material when it is exposed to temperature change. TGA measures the mass change of a specimen as a function of temperature and time under a controlled atmosphere. DTA measures the temperature difference of

the specimen caused by thermal events in a material. It complements TGA data with phase transition information. In this study, TGA/DTA tests of mollusk shell were conducted by DTG-60H Simultaneous DTA-TG apparatus (Shimadzu, Japan). Experiments were conducted in air atmosphere, and temperature rises from room temperature to 900 ℃ with a rate of 10 ℃/min. The purpose of this test is to find the trace of biopolymer degradations with temperature, which can be used for high temperature PFM imaging or heat treatment of the mollusk shell samples.

Chapter 4

Structure and Mechanical Properties of Abalone and Clam Shells

CHAPTER 4 Structure and Mechanical Properties of Abalone and Clam Shells

This chapter presents detailed descriptions of multilevel structures of abalone and clam shells from microscale to nanoscale. FE-SEM and AFM were used to observe these structures. In addition, the nanoscale elasticity mappings of abalone shell by using DART CR-FM are presented as well.

4.1 Nano- to Micro-Structure of Abalone Shell

The microscopic hierarchical structures of abalone shell have been extensively studied as described in the literature review chapter. The nanoscale structures of polished fresh abalone shell are particularly discussed in this section. Fig. 4.1 shows AC-mode AFM images of cross-sectional surface, inner (nacre) and outer (calcite) surfaces of abalone shell. By controlled polishing of irregular outer surface of the abalone shell, the transition regions from nacre to calcite also can be visualized on the same surface [Fig. 4.1(a)].

Nacre nanostructure is presented in Figs. 4.1(b), (c) and (d). Several interesting features can be observed. Firstly, on the cross-sectional nacre surface, the "brick-and-mortar" structure can be clearly identified. However, bulging bridges/layers can be visualized near the biopolymer layers. It is the particular feature of polished nacre. The thickness of these bridges is mainly affected by polishing direction with respect to the z-axis of the aragonite platelet. If the polished surface is perfectly parallel to z-axis of platelets, which is difficult to achieve, the bridge is the thinnest or even disappears. This

phenomenon brings the idea that the mechanical properties of the junction between mineral and interlamellar biopolymer may differ from the other part of the structure. This junction is more resistant to the shear stress induced by polishing, or the bonding at this region is much stronger than that in the other regions. Secondly, the whole image appears to be composed by large numbers of nanograins. They can be visualized more clearly in the phase image [Fig. 4.1(c)]. Contrast of the phase image is constructed based on the material property variations. The phase image (phase lag) is recorded under repulsive force regime indicated by the phase angle which is less than 90 °. Thus, the brighter pixels indicate more energy dissipation, and these regions surround the nanograins. Generally, this type of response represents softer materials if the dissipation is due to repulsive viscoelastic interaction or more hydrophilic surface if the dissipation is from water capillary hysteresis (Sahagun et al., 2007). In the second case, the phase image can be regarded as a surface hydrophobicity map for biological samples. No matter in which case, these regions are expected to be the biopolymers. Thus, the biopolymers and mineral phases can be differentiated to certain extent from the phase image. Lastly, platelets with different sizes and shapes can be clearly seen in Fig. 4.1(d). Some polishing marks strike through the platelets. The intertabular biopolymers that supposed to locate at platelets boundaries may be detached due to the polishing process.

On the other hand, calcite nanostructure is presented in Figs. 4.1(e), (f) and (g). The whole cross-sectional surface is composed by elongated needle-shape nanograins [Fig. 4.1(e)], which are also embedded in the biopolymer matrix. All of these nanograins have similar physical orientation. The whole

surface seems more uniform than that of the cross-section surface of nacre. In addition, Fig. 4.1(g) illustrates the calcite surface that composed by oval nanograins. The grain size is larger than that of nacre. The bright and dark regions may be from the different prisms.

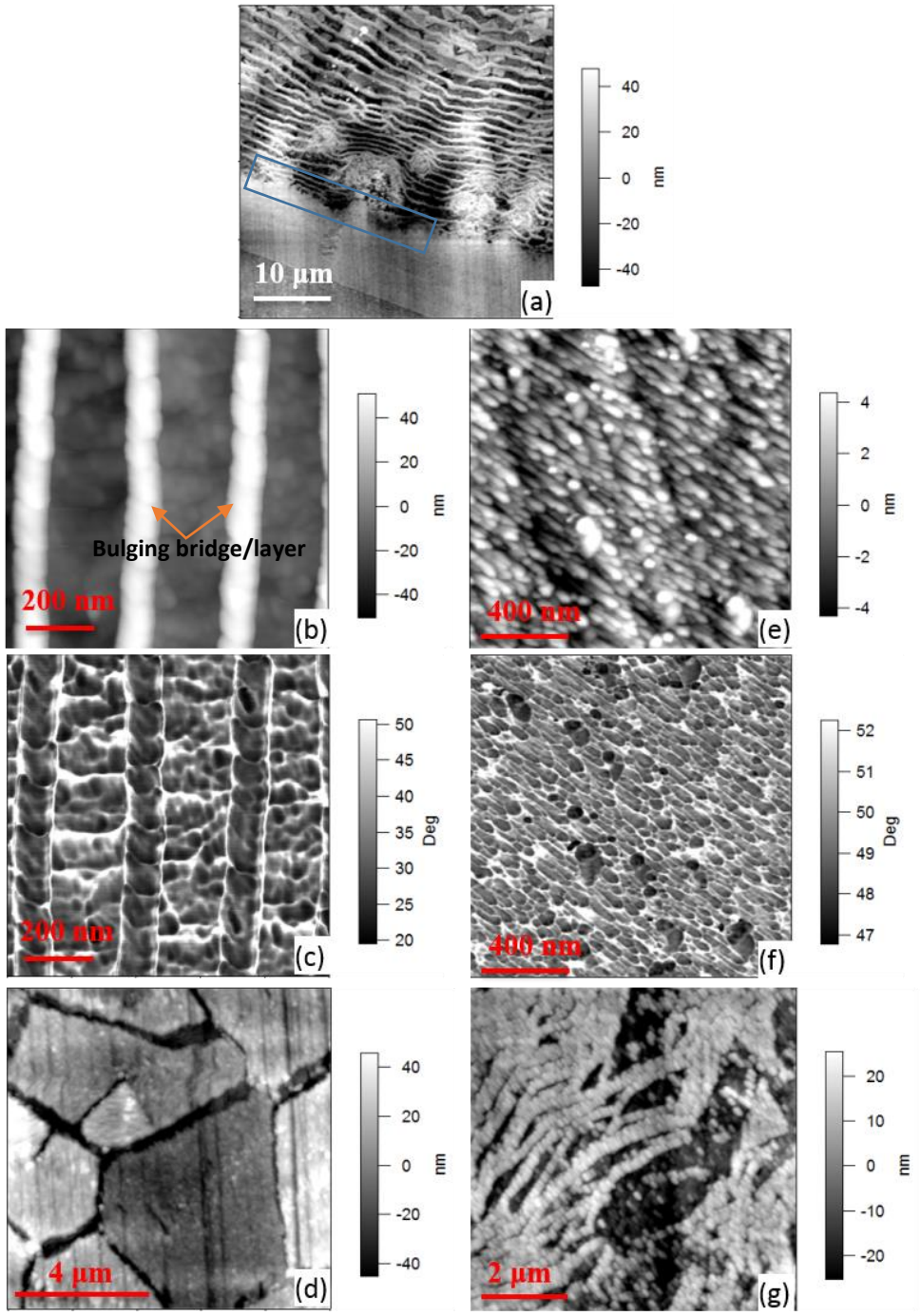

Fig. 4.1 Micro- and nano-structures of abalone shell. (a) height image of the region showing transition between nacre and calcite, (b) height image of cross-sectional nacre, (c) phase image of cross-sectional nacre, (d) height image of nacre surface, (e) height image of cross-sectional calcite, (f) phase image of cross-sectional calcite, and (g) height image of calcite surface.

4.2 Nano- to Micro-Structure of Clam shell

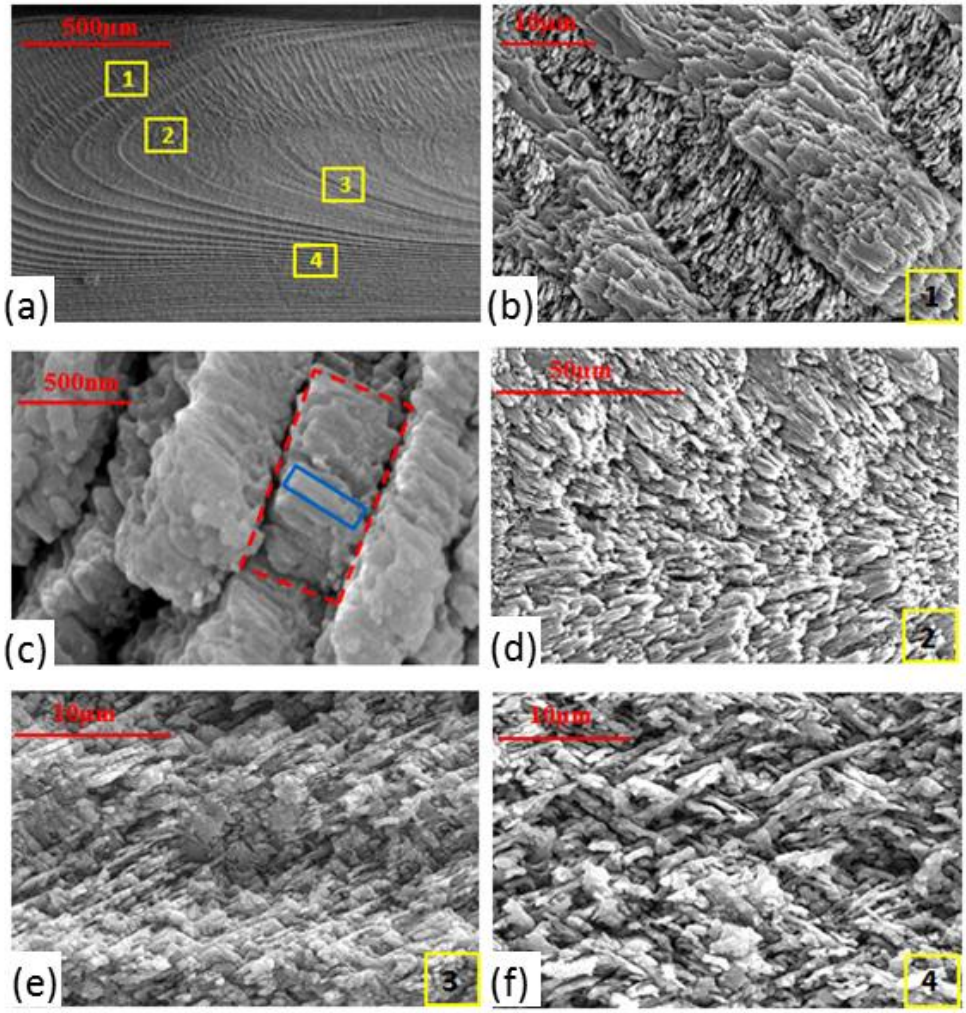

Fig. 4.2 Hierarchical structures of clamshell observed by FE-SEM: (a) Overall structure of entire cross-sectional clamshell; (b) 1st level structure in the region "1" of the Fig. (a); (c) 2nd level structure in region "1" of the Fig. (a), it is composed of 3rd level lamellar/needles; (d) Concentrated packing of needles at region "2" of the Fig. (a); (e) Enlarged microstructure at region "3" of the Fig. (a) – transition region from outer shell to inner shell; and (f) Enlarged micro-structure at region "4" of the Fig. (a) – inner translucent region.

From the FE-SEM observations (Fig. 4.2), two types of macroscopic sections are clearly visible on the cross-sectional surface of partially decalcified clam shell, i.e., the concentric hemi-ellipse patterns near the outer surface, and the parallel straight-line patterns near the inner surface of the clam shell [Fig. 4.2(a)]. There are also wavy patterns cutting through the

concentric hemi-ellipses. Under higher magnification, four levels of hierarchical structures can be observed. The 1st level laminas are clearly revealed in Fig. 4.2(b) [corresponding to the position "1" in Fig. 4.2(a)]. Different from the stacked single-orientated layers in nacre, the structure of clam shell near outer surface is in cross-lamella fashion, which leads to the similar microscale structure when viewed from the outer shell surface and the cross-sectional surface. Within each 1st level lamina, there are similarly oriented close-packed 2nd level laminas, and they are found to be reoriented by about 90 °in the neighboring 1st level lamina. In addition, the 3rd level structure [indicated by the solid rectangle in Fig. 4.2(c)] is tightly packed laminas or needles along their short axis to form a single 2nd order lamina [indicated by the dotted rectangle in Fig. 4.2(c)]. The 4th level or the highest order of the hierarchical structure observed in clam shell is the oval grains that compose each of the 3rd level structure. Moreover, at the position "2" in Fig. 4.2(a), i.e., the arc enclosed region, needle-shape crystals are found pointing towards the center of the arcs [Fig. 4.2(d)]. At the position "3" in Fig. 4.2(a), which is the transition between the outer and inner shell, repeated inter-crossed crystal patterns can be observed [Fig. 4.2(e)]. Finally, at the position "4" in Fig. 4.2(a), the levels of hierarchies are greatly reduced, and only the inter-crossed needles can be identified [Fig. 4.2(f)]. The arrangement of crystals becomes relatively uniform in this region. The differences in crystal arrangements between the inner and outer shells cause their distinct appearance in transparency.

In addition, both decalcified and deproteinated samples are examined. The biopolymers are primarily found between the 2nd level laminas as showed

by decalcified sample in Fig. 4.3(a). For deproteinated sample, Fig. 4.3(b) shows that the biopolymers between the 2nd level laminas are now removed and the nanograins are more clearly visible. In Fig. 4.3(c), it shows many highly localized smooth facets, which are not observed from decalcified sample. It can be the detachments of close-packed mineral grains from the sample surface due to the removal of the biopolymers, which is the joining media between the mineral particles. Therefore, biopolymers in clam shell should be existed between the 2nd level lamellas, as well as within the 3rd and even the 4th level of structures.

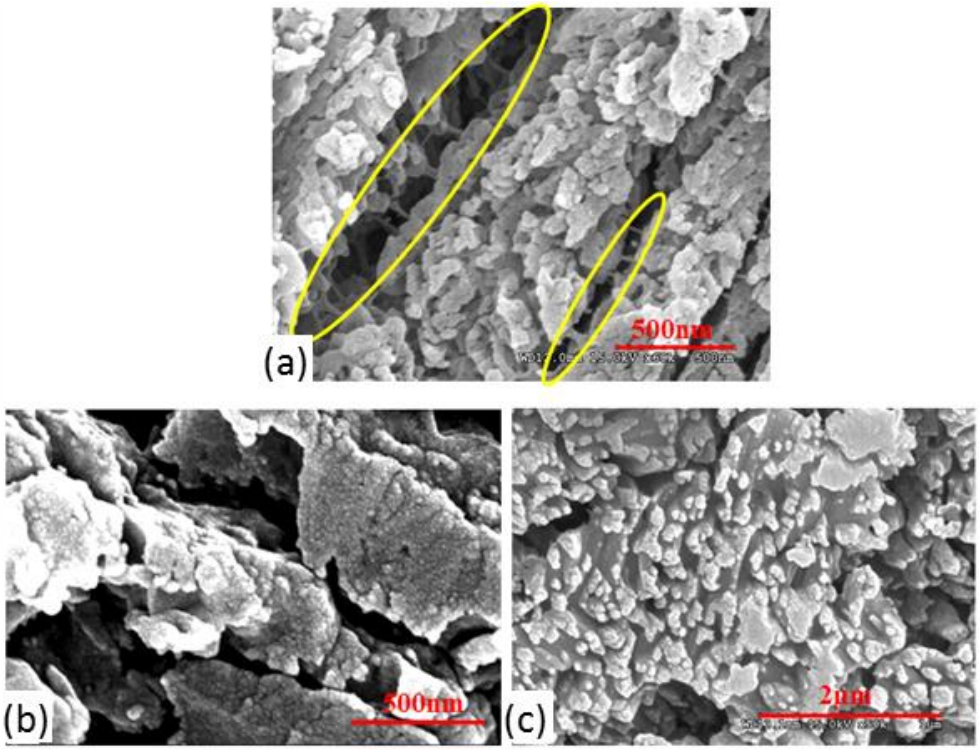

Fig. 4.3 FE-SEM images to reveal the biopolymer distributions. (a) cross-sectional surface of the decalcified clam shell (transition region close to outer shell), (b) microstructure of deproteinated cross-sectional clam shell near the inner surface, and (c) microstructure of deproteinated outer shell surface.

The nanoscale structure of fine polished clam shell images by AFM is illustrated in Fig. 4.4. Compared to that of the abalone shell, clam shell has more uniform structure. The topographic images are similar in several observation directions and locations, except the inner layer when observed from the cross-sectional surface. Blocks of mineral are usually found at this region.

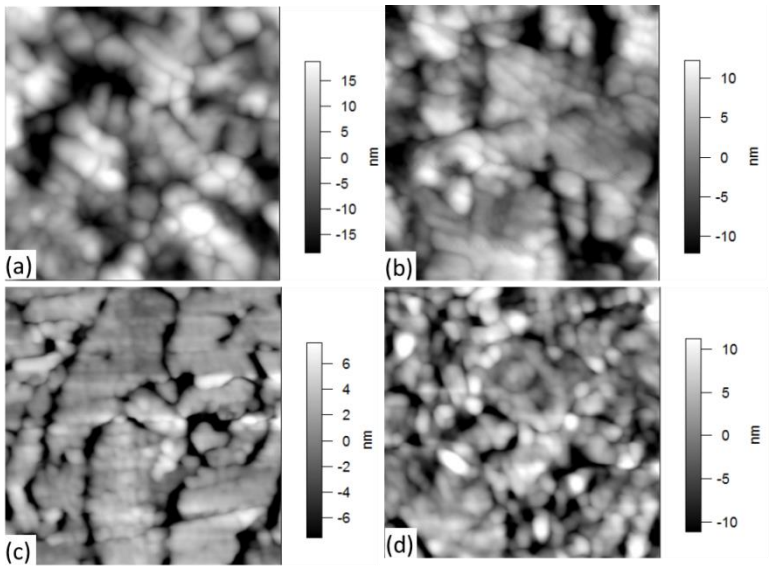

Fig. 4.4 Topographic images observed from (a) cross-sectional surface at the outer layer, (b) outer shell surface, (c) cross-sectional surface at inner layer, and (d) inner shell surface. Scan size of (a) and (b) is 1×1 μm^2, and for (c) and (d) is 2×2 μm^2.

4.3 Nanoscale Elastic Modulus Mapping of Abalone shell on the Nanoscale by CR-FM

To the best knowledge of the author, only one paper reported the nanoscale elastic modulus of mollusk shell characterized by CR-FM technique (Moshe-Drezner et al., 2010). In that study, the cross-section of nacre from a bivalve shell has been studied. The elastic modulus of the interlamellar biopolymers or β-chitin was reported to be 40 GPa. Moreover, from the

accumulated modulus maps, the gradual changes of elastic modulus in the aragonite tablets near the mineral/polymer interfaces were revealed. The regions of modulus changes are approximately four times larger than the thickness of the interlamellar biopolymer layers (~30 nm). However, Moshe-Drezner's study did not provide clear true nanoscale modulus mapping of the mineral grain and intracrystalline biopolymers.

On the other hand, in this thesis, abalone shell was studied using the CR-FM method in the direction normal to the outer shell surface. During the polishing process, the outer calcite can be gradually removed, and the underlying nacre can be exposed. Due to the uneven outer surface of the abalone shell, there are certain regions that the transition line between the calcite and nacre [as illustrated in Fig. 4.1(a)] can be exposed. Thus, the elastic modulus and loss tangent of calcite, nacre, and their transition regions were characterized and compared. These studies have not been reported and discussed in any literature. The details of experimental procedures were presented in Chapter 3. To validate the analysis method, the critical experimental settings are listed in the following:

(a) Applied static force is larger than the adhesion force between tip and samples.

(b) Ensure elastic material response by not using too large loading force.

In addition, the assumptions used in the elastic modulus calculation are listed below (the data analytical method was described in section 2.3.2 in detail):

(i) Material properties of Si cantilever: E=165 GPa, and ν=0.3;

(ii) Poissons' ratio of mollusk shell = 0.3;

(iii) Lateral coupling is neglected;

(iv) Reference samples are homogeneous in both lateral and depth extent; and

(v) Small damping evaluated by $a_n > 50b_n$.

4.3.1 Stiffness and Loss Tangent Mappings of Calcite

The most intriguing feature of CR-FM is the ability to give a nanometer or even sub-nanometer mapping of semi-quantified or quantified elastic modulus of the tested materials, depending on how accurate the experimental conditions can be controlled. Fig. 4.5 illustrates the DART CR-FM mappings of calcite surface under different mechanical loading forces. Larger loading force leads to larger tip contact area and more deeply penetrated stress field. However, tip wear is severe under large loading force, which can lead to high adhesion force. Moreover, contact radius varies continuously with scanned distance for both stiff and compliant cantilevers (Killgore, Geiss and Hurley, 2011). Contact radius is another critical parameters to quantify the elastic modulus from the CR-FM measurements (Hurley, 2010). The use of reference material eliminates the need to characterize contact radius directly by applying the same loading force on both sample and reference materials. However, duo to the continuous tip wear, the contact radius for sample and reference material can never be the same in reality, which is an important obstacle on the quantification of elastic modulus. To reduce the contact radius variation, in this work the loading force for all measurements is maintained to be less than 200 nN. Larger contact

radius can be directly identified from the height images, indicated by blurrier image and less detail features [Figs. 4.5(d) and (g) compared to (a)].

The extent of stress field depends on the stiffness of the tip and sample, the size and shape of the tip, as well as the applied force. If stress field extends deeply enough to probe an inclusion in the subsurface, and the stiffness of the inclusion is different from that of the surrounding matrix, the stiffness of the surface will be locally changed (Killgore et al., 2011b). If assuming Hertzian contact, the probed volume of materials is approximately three times of the contact radius in depth and diameter (Campbell, Ferguson and Hurley, 2012). As mollusk shells are nanocomposite, the stress field extent right below the AFM tip may contain alternating stacks of nanograins and biopolymers. Thus, stiffness obtained from different loading force may actually measure properties from surface to sub-surface materials. CR-FM is sensitive to surface roughness. But there is no strong correlation between height and modulus images, which indicates minimum topographic crosstalk.

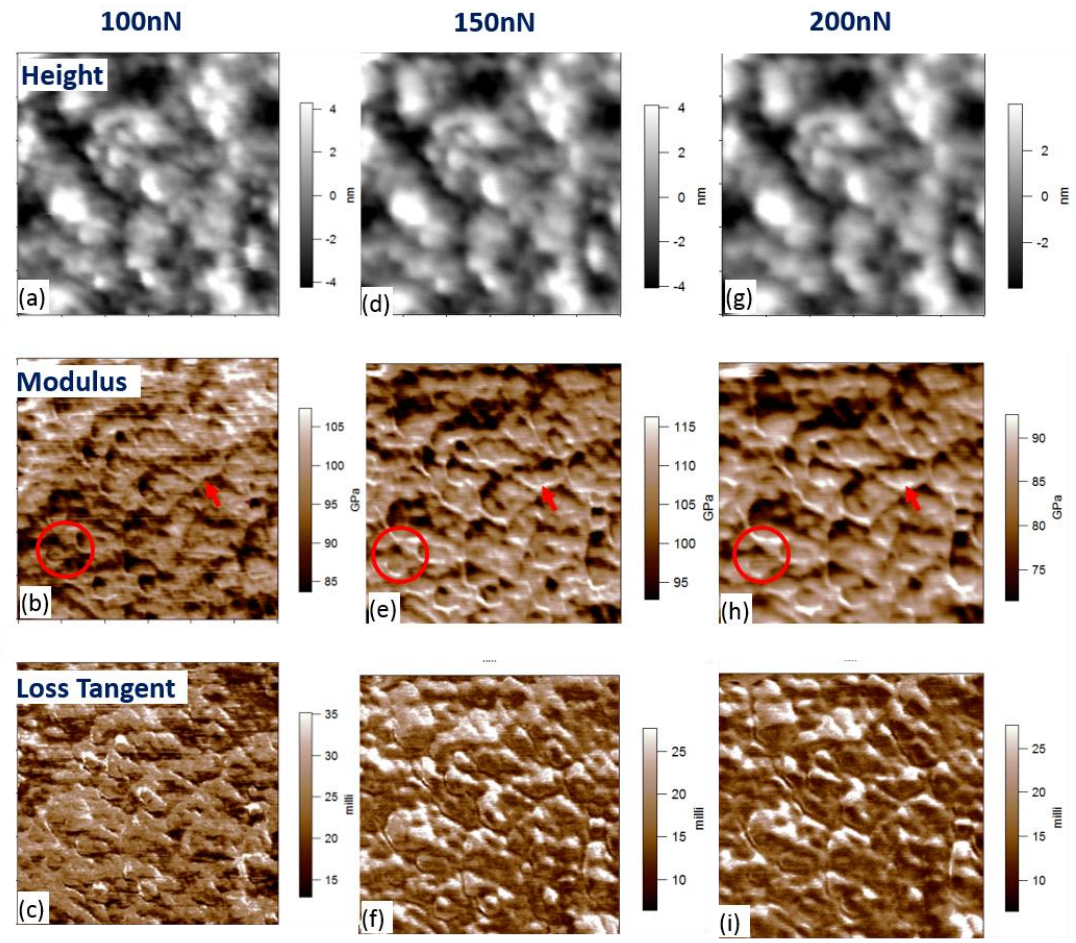

Fig. 4.5 CR-FM images (height, reduced modulus and loss tangent) of calcite surface at the same location with different loading forces: (a-c) 100 nN, (d-f) 150 nN, and (g-i) 200nN. Scan size is 600×600 nm^2.

The mean elastic modulus of calcite that calculated from CR-FM measurement by assuming tip properties (i.e., E=165GPa, υ=0.3) is 66.52, 70.77, and 60.55 GPa respectively under the loading force of 100, 150, and 200 nN. The contrast of materials modulus, reduced modulus and frequency mapping images are identical regardless of the unit and the exact values.

The modulus and loss tangent contrasts observed under 100 nN is dramatically different from those obtained under 150 and 200 nN. With 100 nN loading force, only properties very near sample surface are measured. The least stiff region [dark-color in Fig. 4.5(b)] occupies about 18% area of the

scanned surface and has modulus value of about 60 GPa. These regions do not have direct correspondence with the height image, they are distributed on both nanograins and grain boundaries. However, the less-stiff response should be originated from biopolymer contents. Thus, these less stiff regions should have more amount or volume of concentrated biopolymers, in both lateral and vertical extent. When loading force is increased to 150 and 200 nN, the measurement is more on the bulk property of calcite. Thus, their contrast are very similar. When probed the subsurface, the initially soft region become stiffer compared to the neighbor materials [circled in Figs. 4.5(b), (e) and (h)], which may be due to the stress field extents deeper to a level where nanograins are located. On the other hand, brighter contrast or stiffer regions at grain boundaries are evolved under large loading force [pointed by arrows in Figs. 4.5(b), (e) and (h)]. Biopolymers are expected to be located at these regions under loading-free condition. Large loading force can slight press the nanograins into the intracrystalline biopolymer matrix, and the biopolymers may be squeezed out near the grain boundaries. When scanning these regions, the squeezed out biopolymers together with the surrounded nanograins may show the highest stiffness.

In addition, loss tangent (tan δ) indicates damping condition. The measurements of tan δ are not relied on referencing or calibration technique (Campbell, Ferguson and Hurley, 2012). It was found that the tan δ mapping has invers contrast compared to that of the modulus mapping. It is reasonable because soft material may absorb or dissipate more energy when interacts with AFM tip, whereas hard material preserves more energy when the tip-sample interaction is concerned.

Generally speaking, calcite in abalone shell is a non-homogeneous material. Its stiffness varies from location to location. The maximum elastic modulus difference in this particular region is more than 10 GPa. It is proved that the CR-FM mapping can evidently reveal such difference on the nanoscale, which is unachievable by other techniques, such as nanoindentation tests.

4.3.2 Stiffness and Loss Tangent Mappings of Nacre

The similar CR-FM measurements were also conducted on nacre surface. The DART CR-FM mappings under different loading forces are illustrated in Fig. 4.6. Under the same experimental conditions, the mean elastic moduli of nacre (aragonite) are 60.87, 67.63, and 57.24 GPa respectively under loading force of 100, 150 and 200 nN. Overall nacre is softer than calcite. The modulus values determined from CR-FM measurement are very similar to the bulk properties of nacre reported in the literature (Heinemann et al., 2011). The average modulus and loss tangent of both nacre and calcite are summarized in Table 4.1 for convenient comparison.

Different from that of the calcite, it is noticed that some areas are highlighted by red-color in Figs. 4.6(b), (e) and (h), and correspondingly black-color in Figs. 4.6(c), (f) and (i). These red-color indicates the non-applicable of the modulus calculation method described before. They are directly caused by the extremely low values of raw amplitude data, which indicates large damping that violates the assumption (v) (page 61). These regions may also indicate plastic deformation. Most of the red-color areas are located at the voids on the scanned surface, which may correspond to the

biopolymers. The amount of red-color area is gradually reduced with increased loading force, and this may be due to the extended stress field that start to include the subsurface nanograins. There are no significance contrast differences in the modulus mapping of the nacre among different loading forces. However, the area percentage of stiffer regions [indicated by white-color in Figs. 4.6(b), (e) and (h)] in nacre is higher than that in the calcite, which may be due to more biopolymer contents in nacre. Similar to calcite, nacre is also a kind of non-homogenous nanocomposite material, whose maximum modulus difference is about 15 GPa within the scanned surface.

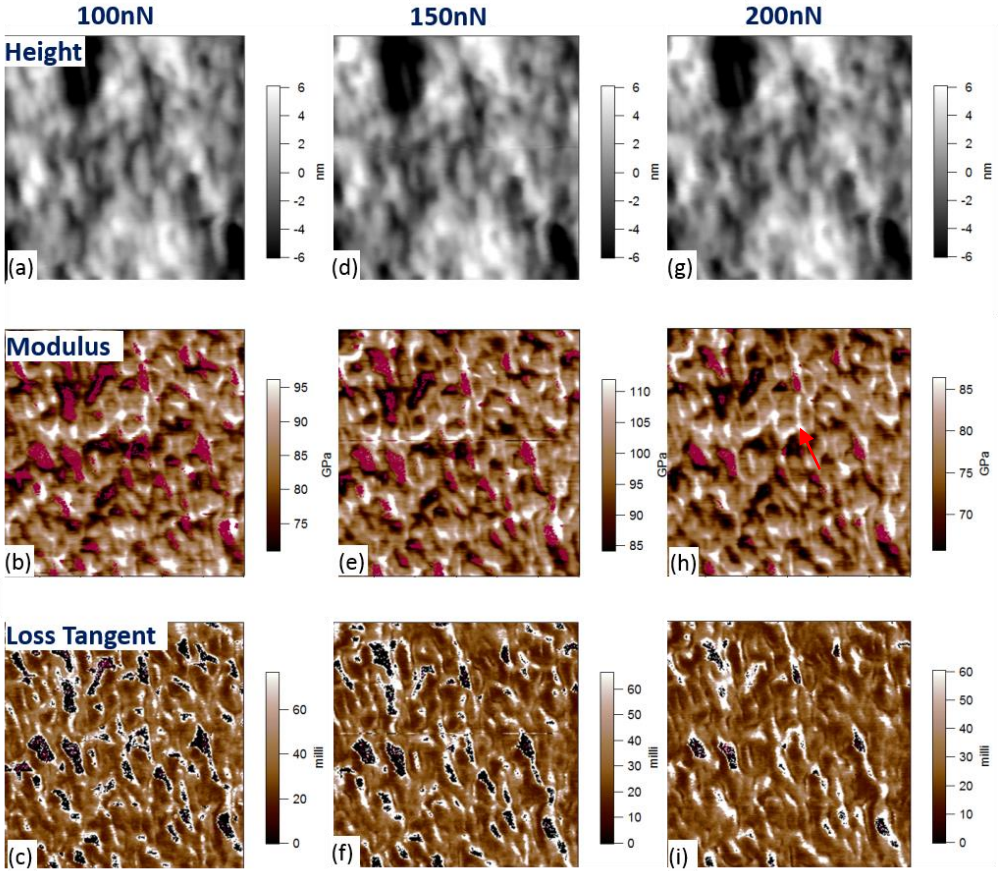

Fig. 4.6 CR-FM images (height, reduced modulus and loss tangent) of nacre surface at the same location with different loading forces: (a-c) 100 nN, (d-f) 150 nN, and (g-i) 200nN. Scan size is 600×600 nm^2.

Table 4.1 Average elastic modulus and loss tangent of calcite and nacre under various loading force. (Extracted from n=65536 data points) "R"- reduced elastic modulus; "S"- material elastic modulus

	Elastic Modulus (GPa)			**Loss Tangent (tan δ)**		
Force (nN)	**100**	**150**	**200**	**100**	**150**	**200**
Calcite-R	95.26±5.88	104.51±5.78	82.02±4.23	0.0237 ±0.0055	0.0175 ±0.0053	0.0167 ±0.0054
Calcite-S	65.43±2.57	69.34±2.38	59.30±2.55			
Nacre-R	83.40±6.22	98.02±6.88	75.92±5.13	0.0382 ±0.0272	0.0331 ±0.0249	0.0298 ±0.0216
Nacre-S	64.08±3.07	66.61±2.95	56.27±2.61			

In addition, the cross-sectional nacre has also been characterized (Fig. 4.7). However, due to the much higher roughness, defects are always associated with the DART CR-FM mappings, and higher loading force is required to obtain a relatively decent image. Bulging layers are again shown in this set of images. Near the bulging layer there are regions having low stiffness and high tan δ. They are expected to be the interlamellar biopolymers. Inside each platelet, nanograins can be identified on the height images. Similar to that of nacre surface, white-color area that surrounded mineral grains also appear on the cross-sectional nacre. The full range of stiffness values observed from both nacre surface and cross-sectional surface of nacre are similar. Therefore, the nanoscale stiffness is directional independent because at this scale only the highest level of hierarchical structure are measured and characterized. The main factors affect the stiffness mapping are the different chemical compositions, i.e. biopolymer or mineral, as well as the volume fraction of the individual component within the stress field.

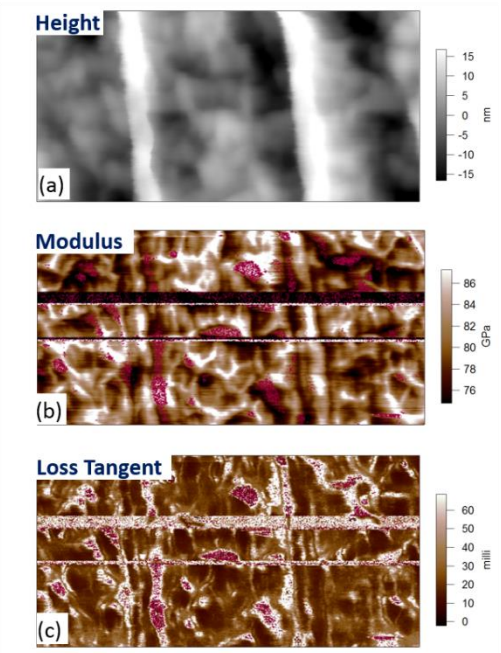

Fig. 4.7 DARC CR-FM images of cross-sectional nacre. (a) Height, (b) reduced modulus, and (c) loss tangent. Loading force: 450 nN. Scan size: $0.5 \times 1\ \mu m^2$

4.3.3 Stiffness Mapping of Calcite-Nacre Transition Region (CNTR)

The microscale topographic image of the transition region is shown in Fig. 4.1(a). The stiffness mappings of the CNTR by DART CR-FM were conducted at the regions very close to the boundary line, as enclosed by a rectangle in Fig. 4.1(a). Fig. 4.8 shows the DART CR-FM images of the exact boundary, as well as the regions slightly offset towards the side of nacre or calcite. The surface roughness defined by RMS values of the transition boundary is about three times larger than that of nacre or calcite. By examining the histogram plot of the reduced modulus mapping [Fig. 4.8(f)], calcite-side still has the highest mean modulus value, while nacre-side has the similar lower modulus as that of the boundary region. However, when compared with that of the calcite and nacre sections far away from the CNTR boundary, the regions near CNTR boundary exhibit the smallest modulus, which can be one of the reasons to cause more non-calculable data points (red-

dots in modulus mappings in Fig. 4.8). Therefore, the nature-designed transition between the different minerals is generally softer than that of the mineral themselves.

By examining the contrast of the modulus mapping, the transition region is even more non-homogenous than that of the pure calcite or nacre, for instance, the boundary near nacre side shows discrete regions [enclosed by two rectangles in Fig. 4.8(b)] with different modulus value ranges. Moreover, similar to that of the calcite and nacre, the stiffened nanograins boundaries (white-color area pointed by arrows in Figs. 4.5 and 4.6) can also be identified in the modulus mappings. The regions having dark-contrast or lower modulus are expected to be biopolymer concentrated area.

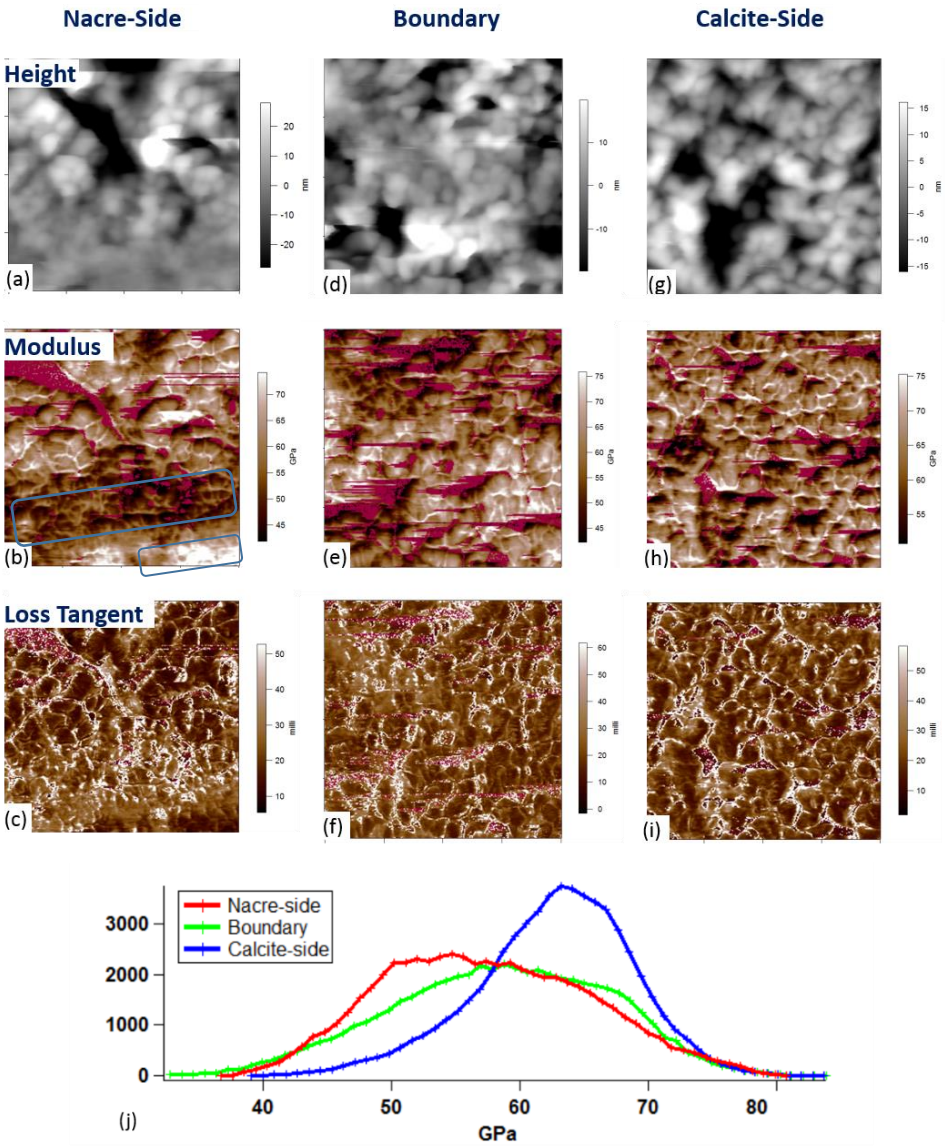

Fig. 4.8 DRAT CR-FM mappings of CNTR region, including height, *reduced* modulus, and loss tangent. Loading force: 150 nN. Scan size: 800 ×800 nm^2. The histograms of modulus mappings [(b) (e) and (h)] data are plotted together in (j).

4.3.4 Stiffness Mapping of Deproteinated Abalone Shell

To further verify the previous findings, the same shell sample underwent chemical treatment to remove biopolymers near the sample surface. Fig. 4.9 shows the DART CR-FM mappings with the exactly same settings as those used for fresh shell sample. After protein removal, the elastic modulus of nacre is increased significantly (about 10 GPa) compared to that of the fresh nacre surface under the same loading force. On the other hand, the elastic

modulus of the calcite is not increased much probably due to the small amount of polymer contents in the calcite region. Eventually, calcite and nacre regions show the similar values of the mean elastic modulus in the scanned surface. As expected, the elastic modulus is increased after deproteinated treatment on abalone shell. Furthermore, the extent of stiffened nanograin boundaries under relatively high loading force is reduced. It suggests that biopolymers may be contributed to the high stiffness of those regions in the fresh shell sample.

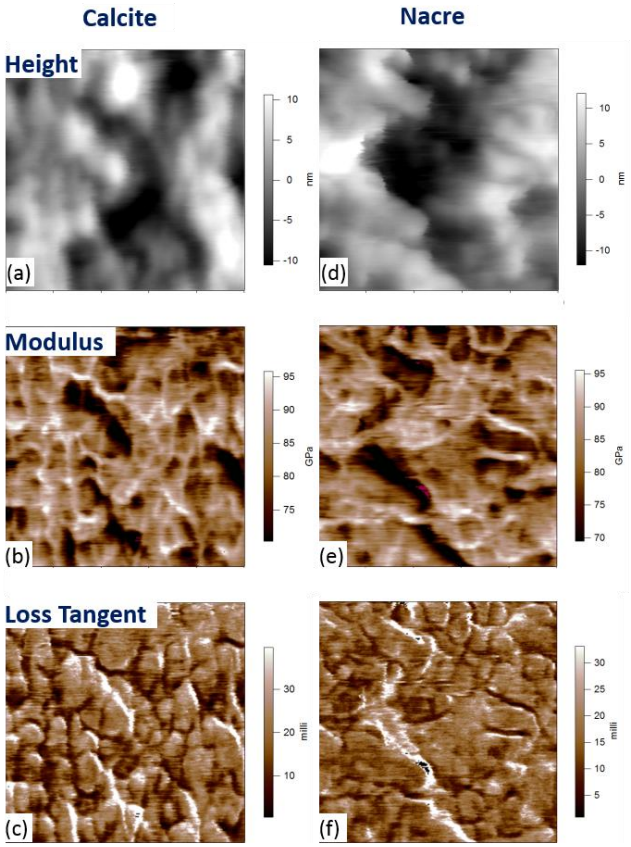

Fig. 4.9 DART CR-FM reduced modulus and loss tangent mapping of deproteinated calcite and nacre surface. Loading force: 200 nN. Scan size: 500 ×500 nm^2.

4.4 Summary

This chapter presented the hierarchical structures of both abalone and clam shells from micro- to nano-levels. The smallest feature of mollusk shells are the nanograins which are usually embedded in the biopolymer matrix. More importantly, the nanoscale elastic modulus and loss tangent mappings of the abalone shell have been obtained by using DART CR-FM method. Based on these mappings, it was found that the mollusk shell is highly non-homogenous material with the stiffness varied nearly point to point. This variation can only be observed by the CR-FM method. The fresh calcite and nacre, and NCTR boundary have been characterized. The NCTR boundary show much lower stiffness than those in other regions. The stiffness of nacre determined by this method is similar to that reported in literature. Furthermore, stiffening effect at nanograin boundaries under large loading force has been identified. It is believed that the biopolymers play roles in this effect based on the observations from deproteinated abalone shell. However, the results presented in this chapter is only semi-quantified. Many factors may affect the full quantification, for instance, the continuous change of tip radius and the choice of reference sample. Nevertheless, it is worth to conduct CR-FM tests on calcified tissues to give more valuable nanoscale mechanical information for better understanding of the material performance.

Chapter 5

Biopiezoelectric Properties of Abalone and Clam Shells Studied by PFM

CHAPTER 5 Biopiezoelectric Properties of Abalone and Clam Shells Studied by PFM

This chapter presents the determination and analysis of the biopiezoelectric properties of both abalone and clam shells, including the analysis of nanoscale PFM images, and the observation of piezoelectric constant d_{zz}. In addition, shells with proteins removed have also been studied and compared to those from the fresh shell. Lastly, the comparative studies of vertical and lateral piezoresponses of the abalone shell are presented. In this chapter, the piezoresponse observations were conducted on two surfaces: the cross-sectional surface and the outer or inner shell surface (i.e. platelet surface).

5.1 Biopiezoresponse of Abalone Shell

5.1.1 Electric Field Induced Topographic Change

It has been reported that the rotation and deformation of aragonite cobble-like polygonal nanoparticles are the two prominent mechanisms contributing to energy dissipation in abalone shell, and the biopolymer facilitates the particle rotation process (Li et al., 2004). In our studies, it has been found that this rotation and deformation of the aragonite nanoparticles can also be triggered by external electric field. By using DART-PFM, it is found that the nanograins of abalone shell are deformed and enlarged with increasing drive amplitude V_{ac}, as illustrated in Figs. 5.1(a)–(d).

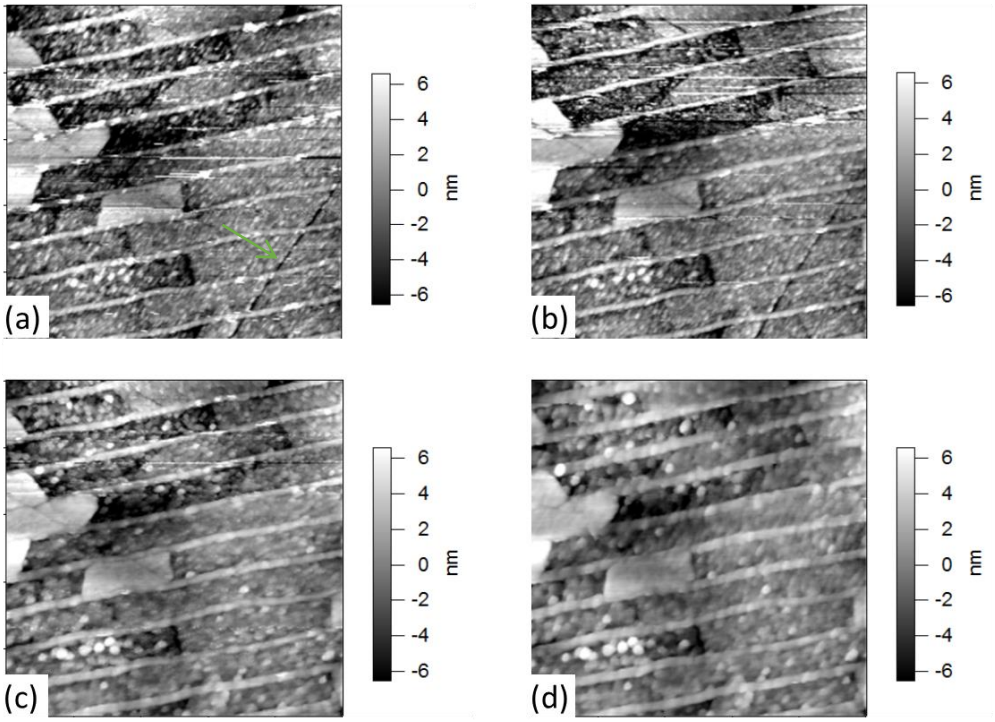

Fig. 5.1 Topographic images in the same scanning area. The drive amplitude is increased from 1.5 V_{ac} for image (a) to 3 V_{ac} for image (d), with 0.5 V_{ac} step. The mean heights of images (a)-(d) are -87.45 pm, -80.65 pm, -58.34 pm and -50.93 pm respectively.

The mean heights of the images is found to be increased almost linearly with the applied AC voltage, which demonstrates the piezoelectric deformation of the abalone shell structures. Therefore, the deformation and rotation of nanoparticles can be initiated by either mechanical stress or electric field. As the shells show piezoelectric properties, the electric field can be generated by mechanical stress, or vice versa, the mechanical stress can be generated by electric field. Furthermore, it is also noticed that the scratch mark in Fig. 5.1(a) (indicated by an arrow) gradually disappears with the increases of the applied voltage. This phenomenon reveals the potential of the self-healing behavior of the abalone shell under an external electric field or being generated by the external mechanical stress. Since PFM uses inverse piezoelectric principle, this means that the mechanical stress can generate an

electrical field, and the electrical field can cause particle deformation and rotation as well as possible crack or damage healing by this structure. The results further suggest that the toughness and strength of abalone shell may be also related to its intrinsic piezoelectric properties.

5.1.2 Piezoresponse and Domains Revealed from PFM Images

It is generally accepted that the organic constituents (mainly proteins and polysaccharides) are responsible for the piezoelectric behavior in biological material, owing to its large and complex molecular structure. The majority of the organic phases are water insoluble (Nudelman et al., 2007), and are mostly concentrated between the mineral layers in nacre. The first protein in the abalone shell is identified as the large multidomain protein Lustrin A by sequence analysis (Treccani et al., 2006), this protein provides adhesion between the platelets. Other constituents include aspartic acid, glutamic acid and serine. In addition, glycine and alanine are also found in the abalone shell. The bonding between the interlamellar biopolymer and aragonite platelets is based on the Ca^{2+} ions from the (001) plane of aragonite which attach to an aspartic acid-rich protein. The high chitin content β-sheets are the core layers of organic phase with branched aspartic-rich acid (Lin and Meyers, 2005).

In our studies, piezoresponse are found on almost the entire scanned surface, but unevenly distributed regardless of the surfaces studied (Fig. 5.2). In most cases, two types of distinguishable domains can be identified on the phase images (yellow vs. green). From the amplitude images, it is found that one type of the domain has dramatically larger piezoresponse than the other,

and this type of domain is only small portion of the scanned area. Therefore, this type of domain (yellow-color) is expected to be the organic phase concentrated regions.

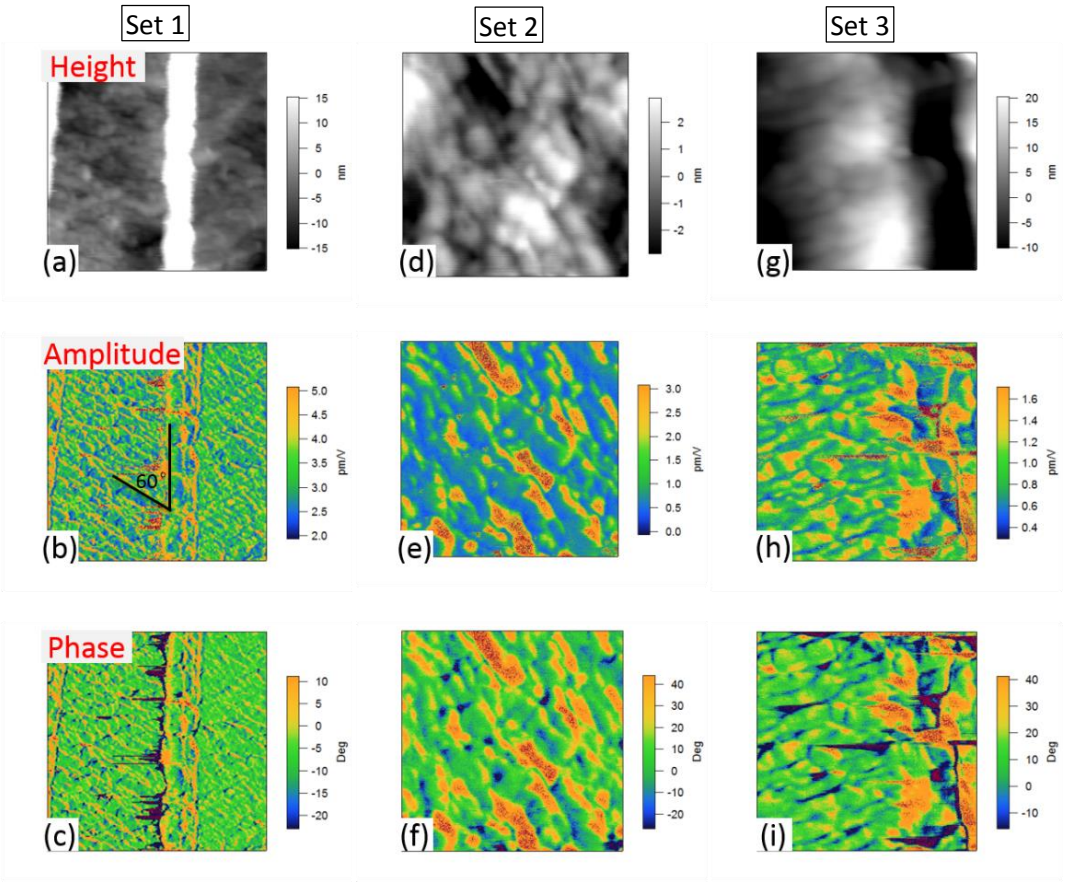

Fig. 5.2 Three sets of DSHO fitted DART-PFM images of abalone shells.1st column (800×800 nm^2): observed from cross-sectional surface with one interlamellar biopolymer layer; 2nd and 3rd column (400×400 nm^2): observed from the interior and boundary of platelet on the nacre surface. (a) (d) and (g) are height images, (b) (e) and (h) are amplitude images, and (c) (f) and (i) are phase images. (probe: AC240TM, k_c = 2.37 N/m)

The three sets of PFM images in Fig. 5.2 are scanned with the same settings. The phase image contrast is quite consistent with amplitude image contrast, which also helps to differentiate regions of micro-constituents with different piezoresponse. The phase lag of green-color domain is always smaller than that from the yellow-color domain. Without knowing the crystal

orientations of shell samples, only the phase difference can be quantified in this case. The phase angle difference between the green-color and yellow-color domains are 13 °, 60 °, and 46 ° for image sets 1, 2, and 3 respectively. In addition, there is no abrupt domain walls between these two types of domains; large gradual phase transition regions always exist between them. Moreover, the yellow-color domains between the nanograins are always found oriented along the direction which is about 60 ° to the interlamellar biopolymer layer on the cross-sectional surface [Fig. 5.2(b)]. From amplitude images [Figs. 5.2(b), (e), (h)], the strongest piezoresponse are mostly confined at the regions of interlamellar biopolymer layer and the boundaries between the aragonite platelets in a single mineral layer. However, a continuous single layer with strong piezoresponse does not exist. This is probably due to the displacement of the organic phase to the adjacent mineral grains during polishing. Theoretically-speaking, $CaCO_3$ should not show any piezoresponse due to its centrosymmetric structure, however in the PFM images, it is found that most nanograins also exhibit piezoresponse on both examined surfaces, but much weaker. The amplitudes are generally five times smaller than those of the organic concentrated regions. It is believed that these responses may originate from the organic phase intercalated within the crystal structure of the $CaCO_3$. These organic contents may have different structures or orientations from that of the interlamellar biopolymers. Furthermore, some of the nanograins also show very strong piezoresponse, which is comparable to that of the organic phase. This may be due to the displaced organic phase covering parts of the nanograins after polishing.

5.1.3 Piezoelectric Constant d_{zz}^{eff}

In order to obtain an overview of the strength of the piezoresponse of the abalone shell, the effective piezoelectric coefficient in the out-of-plane direction, d_{zz}^{eff}, is determined by the image-based method on baby abalone shells (4~5 cm). d_{zz}^{eff} indicates the vertical deformation induced by unit voltage, which is also applied in the vertical direction. Many factors may affect this value, such as scan size, tip-sample interaction, orientation of samples and shell age. In this study, the cantilever is not calibrated. For qualitative purposes, d_{zz}^{eff} is calculated based on the following formula

$$A = d_{zz} V_{ac} Q = d_{zz}^{eff} \times V_{ac} \quad \text{(E5.1)}$$

where A is the raw data of the amplitude measured in pm, V_{ac} is the drive voltage, d_{zz}^{eff} is the slope of a linear fit of the A and V_{ac} curve, and Q is the quality factor to enhance the signal strength which equals to 20~100 for DART- or BE-PFM (Proksch and Kalinin). The superscript "eff" indicates that the value is calculate from the raw data of the amplitude value, i.e., it is not fitted with the DSHO model. In this case, the Q factor is convoluted in the d_{zz}^{eff} value. For the polished cross-sectional fresh nacre, d_{zz}^{eff} is found to be in the range of 13~37 pm/V. d_{zz}^{eff} of the regions near outer shell is relatively higher than that of the regions near the inner shell on the cross-sectional surface. When observed on the inner shell surface, d_{zz}^{eff} is found in the range of 28~47 pm/V, which is slightly higher than that from the cross-sectional surface. For reference, the d_{zz}^{eff} of X-cut quartz is measured in the same way and it is found in the range of 60~90 pm/V. Thus, the piezoelectric constant of abalone shell determined by this method is about 1/4 to 1/3 times of that of X-

cut quartz. Unlike the cross-sectional surface of the abalone shell, it is difficult to identify the exact polishing depth in the mollusk shells when polish the shell surface. Thus, the "inner" and "outer" are relative depth rather than definite values. In this case, the inner shell showed slightly stronger piezoresponse than that of the outer shell region, which is opposite to that observed from the cross-sectional surface. Generally speaking, the piezoresponse varies with the locations inside abalone shell. The piezoresponse is the strongest when observed on the inner shell surface.

5.1.4 Piezoresponse under Relaxed Polishing Stress and Increased Moisture Conditions

After samples are kept in ambient conditions for one day, it is found that the value of d_{zz}^{eff} on the cross-sectional surface of the abalone shell changes significantly. The d_{zz}^{eff} generally increases with time in the inner-shell region, but decreases in the outer-shell region. However, on the shell surface, only inner shell exhibits dramatic decrease of the d_{zz}^{eff} values. These changes in d_{zz}^{eff} may be due to the relaxation of polishing-induced stress and the increased moisture content near the sample surface layer. After this measurement, the samples were kept in distilled water for an additional four days in order to study the effects of increased-moisture on the abalone shell. For those samples, the values of d_{zz}^{eff} decreased to an extremely low values regardless of the surface measured. The reason for this significant reduction in the d_{zz}^{eff} values may be directly due to the increased water content in the sample. The motion of electrically induced ions could neutralize the polar response. There are also other possibilities, such as chemical reaction between

the constituents in abalone shell and water molecules, and the decay or loss of organic constituents. In addition, the analysis of the phase images show scattered histogram distribution of polarization directions at low drive voltage, which indicates that the abalone shell may have reorganized its polar structure in water with the time. When a higher electric voltage is applied, the samples show the same behavior as that stored under ambient condition, i.e., the dipoles rotate to preferred directions according to their piezoelectric effects. In general, after being kept in air or water for a certain period of time, the abalone shells have reoriented their constituents or polarizations in order to eliminate the polishing-induced stresses and to achieve minimum energy state. Apparent changes can even be observed from the topography image. More importantly, the abalone shell studied here is no longer a living biological system, the entire active responses to external stimuli and environments are only the material/structural properties rather than any physiological behavior.

5.2 Comparative Studies of Vertical and Lateral Piezoresponse of Abalone Shell

5.2.1 Response from Inner Surface of Nacre

Both VPFM and LPFM images are acquired at the same location of the inner and cross-sectional surfaces of nacre from a grown abalone shell (7~8 cm in size) respectively. The drive frequencies used for VPFM and LPFM are the first contact resonance frequencies. The vertical and lateral sensitivities are calibrated with the inbuilt software (IGOR Pro) coming with the SPM machine (MFP-3D) by using force curve and friction loop method respectively. The lateral sensitivity was usually found to be 10~20 times larger

than the vertical sensitivity due to the dramatically large in-plane optical amplification in PFM measurement (Peter et al., 2005). Fig. 5.3 shows the orientations and planes stated in this section. In particular, 2D-PFM are conducted on the x-z plane for cross-sectional nacre [Fig. 5.3(a)], and on x-z and y-z planes for platelet surface [Fig. 5.3(b)].

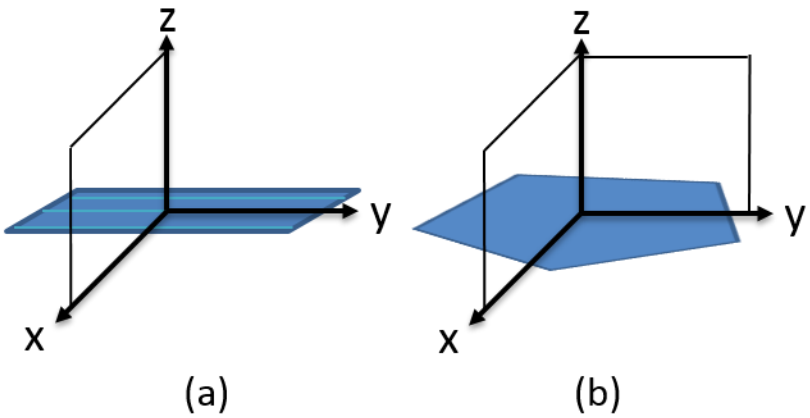

Fig. 5.3 Illustration of observing orientations and planes on both cross-sectional surface (a) and platelet surface (b).

Fig. 5.4 shows the vertical and lateral piezoresponse of nacre observed before and after the sample was rotated by 90 °. Figs. 5.4(a) and (b) are expected to be at the same location. However, the local morphology seems to be altered slightly by the applied bias and contact force after repeated PFM scans, which makes it difficult to identify the identical topographic patterns. Nevertheless, by careful marking, all of the images in Fig. 5.4 were definitely taken within the same square region showed in Fig. 5.5(a). Based on the DART-VPFM images [Figs. 5.4(c)-(f)], both the amplitude and phase images show similar patterns and values before and after the sample rotation by 90 °. The highest amplitudes (indicated by white-color) are observed to be concentrated at the grain boundary regions, which may be originated from the

intracrystalline biopolymers. For biopolymers, the most abundant amino acids that compose the soluble intracrystalline biopolymers can be the Asx (aspartic acid + asparagine), Gsx (glutamic acid + glutamine), proline, glycin, and leucin based on various studies from different groups (Heinemann et al., 2011). All crystals of enantiomorphic (chiral) protein amino acids exhibit a piezoelectric activity, except L-glutamine (Lemanov, Popov and Pankova, 2011). Among these amino acids, pure γ-glycin shows the strongest piezoresponse, which is comparable to that of the quartz crystal (Lemanov, 2000a). Recently, the effective longitudinal piezocoefficient of the as-grown γ-glycine microcrystals was found to be about 10 pm/V through the PFM measurement (Heredia et al., 2012). Therefore, these amino acids should be the foundations of the piezoelectric and ferroelectric response of biopolymers in the mollusk shells. In addition, although most biopolymers are semicrystalline, if there is good molecular orientation and piezoelectric symmetry in the observing directions, the non-crystalline regions can also exhibit piezoelectricity (Ando, Fukada and Glimcher, 1977). On the other hand, the centrosymmetric $CaCO_3$ should not exhibit any piezoresponse. However, some of the nanograins also show relatively high piezoelectric amplitude, which may due to the displaced biopolymers after polishing process or the intercalated biopolymers within the mineral crystal lattice (Pokroy et al., 2006). In the phase images [Figs. 5.4(d) and (f)], the phase angle difference between the biopolymers (dark-color) and nanograins (yellow-color) is approximately 90 °~110 °. The non-180 °phase difference may be due to the lateral component of the polarizations. In general, even after

rotating the sample by 90 °, the vertical piezoresponse of nacre surface is still the same as expected.

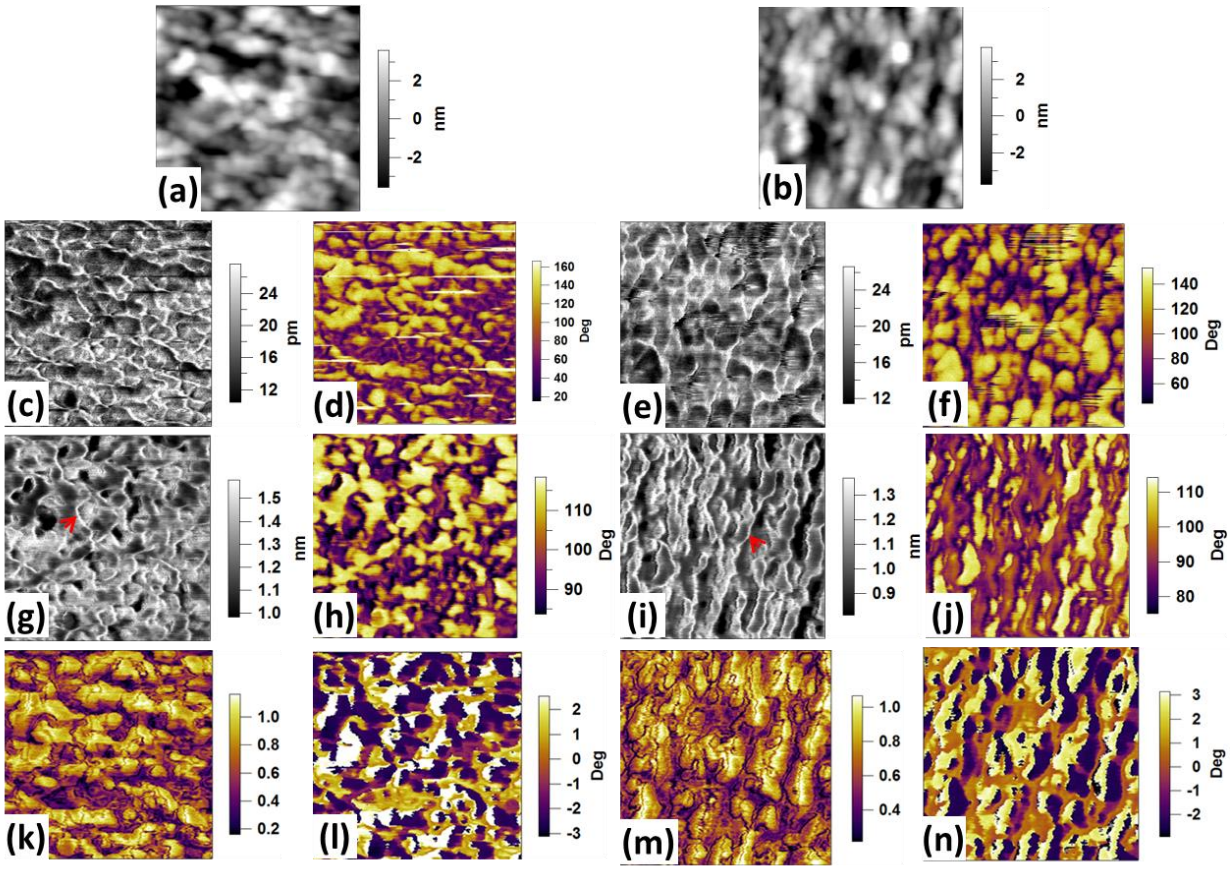

Fig. 5.4 PFM images obtained at the inner surface of nacre (500×500 nm^2, 256×256 pixels). The two columns on the left-hand side are observed from the sample before rotation. The other two columns on the right-hand side are from the 90 °rotated (counter-clockwise) same platelet. (a) and (b) the corresponding topographic images. The 2nd row are DART amplitude [(c) and (e)] and phase [(d) and (f)] images in the vertical direction. The 3rd row are the DART amplitude [(g) and (i)] and phase [(h) and (j)] images in the lateral direction. All of the amplitude images show the piezoresponse at 1 V_{ac}. Last row are the magnitude [(k) and (m)] and argument [(l) and (n)] images of vector-PFM in the x-z [(k) and (l)], and y-z [(m) and (n)] planes.

Figs. 5.4(g)-(j) show the amplitude and phase images of DART-LPFM at the same location as that of the DART-VPFM before and after 90 °rotation of the sample. The amplitude of the lateral images are found to be in the nm level, which is significant larger than the pm level of images observed in the

vertical direction. This significant increment of the orders of magnitude is originated from the large lateral optical magnification as mentioned earlier. Moreover, the LPFM cannot be quantified due to the lack of information of the frictional force. The LPFM can only measure the piezoresponse of sample in the direction perpendicular to the cantilever long axis. The DART-LPFM image patterns observed before and after sample rotation are different, and each corresponds to the local topography. Unlike vertical PFM, the lateral PFM is more susceptible to the topographic cross-talk. DART method can improve the situation, but not eliminate it. The intracrystalline biopolymers located between the nanograins still have the strongest piezoresponse even in the lateral direction (e.g. white curves pointed by red arrows). The mean amplitude value before the sample rotation (the scanning direction is parallel to the lamellar orientation) is 1.29 nm/V**,** which is higher than that observed from the rotated sample (1.06 nm/V). Furthermore, the phase angle difference between the biopolymers and nanograins is ~22 °on both shell surfaces. This much smaller angle difference may be due to the restrains from the torsional movement of the cantilever and the frictional force between the tip and sample surface.

In addition, the vector PFM images in the x-z and y-z planes are obtained by integrating the single frequency VPFM and LPFM images using the method proposed by Kalinin et al. (2006b). The vertical piezoresponse (vpr) and lateral piezoresponse (lpr) is firstly calculated from their own amplitude and phase data by equation E5.1 (Soergel, 2011)

$$pr = A / V_{ac} \times \cos(\varphi) \qquad \text{(E5.1)}$$

Then, the values of vpr and lpr are normalized to the range of (-1,1). The magnitude of the 2D vector-PFM is then calculated by $A_{2d} = \sqrt{(vpr^2+lpr^2)}$, while the argument with respect to the vertical or z-axis is defined as $\theta_{2d} = \arctan(lpr/vpr)$. From the magnitude images [Figs. 5.4(k) and (m)], two types of responses can be observed. One is from the nanograins (bright color) and the other is from the intracrystalline biopolymers located at the grain boundaries (dark color). From the argument images [Figs. 5.4(l) and (n)], the polarization orientation of biopolymer regions exhibit 1 °~2 °angle with respect to the z-axis. On the other hand, the nanograins have two distinct contrasts in Fig. 5.4(l): the white color on the left-hand side of grains, and the purple color on the right-hand side of grains. Clear separations between these two colors are along the apex of each group of nanograins, which indicates the possible topographic cross-talk or artificial effect. These separations of the nanograin domains are mainly originated from the lateral PFM observation. Similar artificial effect is also observed even when sample is rotated by 90 ° [Fig. 5.4(n)]. However, it seems that the intracrystalline biopolymers are free from such effect. The regions with angle of ~1 °can be identified as the biopolymers. Based on the images from 2D vector-PFM, the polarization directions of the intracrystalline biopolymers and the polymers within the mineral phase are both close to the z-axis (i.e. the [001] direction of aragonite platelet) and the difference between them are only ~2 °. However, without the knowledge of the complete type and 3D structure of the biopolymer molecules, it is still difficult to predict the physical orientation of these biopolymers.

5.2.2 Piezoresponse of deproteinated abalone shell

To verify the observed piezoresponse from nacre, the deproteinated sample has been characterized as well. The proteins on nacre surface have been partially removed using the method described in section 3.1.2. Fig. 5.5 shows the DART-VPFM and DART-LPFM response of the deproteinated nacre at the same region of the same platelet as the one where Fig. 5.5 is observed [square region in Fig. 5.5(a)]. After the protein-removal process, the RMS roughness value calculated based on the location illustrated in Fig. 5.5(a) increased from 5 nm to 42 nm. Many voids are observed on the topographic images under both microscale and nanoscale. Nanograins can still be observed from the topographic image [Fig. 5.5(b)]. The amplitude value of DART-VPFM [Fig. 5.5(c)] is greatly reduced compared with that from the fresh sample. The strong piezoresponse at grain boundaries are totally disappeared. The large area of dark color indicates the removal of biopolymers in that region. The bright area may be the response from the residual biopolymers. In case of the DART-LPFM images [Figs. 5.5(e) and (f)], clear contrast and strong response no long exist. The fuzzy contrast may be due to the topographic cross-talk. After the removal of biopolymers, the piezoresponse of the nacre surface is totally different from that observed from fresh sample. With the similar topography features, significantly different piezoresponses have been observed between the deproteinated nacre and fresh nacre samples, which confirms that the piezoresponse observed from fresh nacre is real phenomenon and not from the topographic cross-talk.

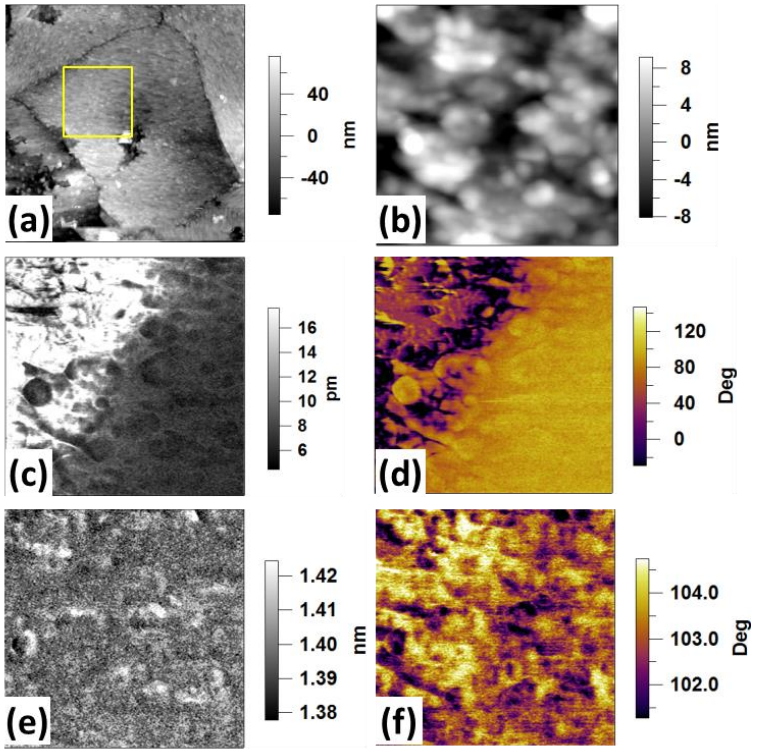

Fig. 5.5 Topographic and PFM images of deproteinated nacre surface. (a) Topographic image of the scanned platelet by tapping mode (7 ×7 μm^2, 512 ×512 pixels); (b) Topographic image where DART-VPFM [(c) and (d)] and DART-LPFM [(e) and (f)] are scanned (500 ×500 nm^2, 256 ×256 pixels); (c) and (e) are the amplitude images; (d) and (f) are the phase images.

5.2.3 Response from Cross-Sectional Surface of Nacre

For the cross-sectional surface of nacre, bulging layers always exist along the boundaries between the mineral and organic interlamellar layers after polishing. There can be the maximum of 100 nm height difference between the bulging layer and the mineral layer. The width of the bulging layers depends on the cutting direction in relative to the direction normal to the platelets. If the cut plane is perpendicular to the top and bottom surfaces of the platelets, the thickness of the bulging layer is the minimum. The cause of this bulging layer may be that the boundaries between biopolymer and mineral layers always exhibit higher resistance to the polishing stresses. These bulging layers can be a problem if the scanning direction is parallel to them. Since the

LPFM scanning can only be performed with 90 ºscan angle to the cantilever axis in order to minimize the signal from cantilever bulking. Therefore, the LPFM image is only observed at the direction perpendicular to the mineral layers on the cross-sectional nacre. Besides the intracrystalline biopolymers, the interlamellar biopolymers also can present on the cross-sectional surface. Fig. 5.6 illustrates the DART-VPFM and -LPFM responses of cross-sectional nacre surface. In the VPFM image, large amplitude regions are along the bulging layer that originated from the interlamellar biopolymer. But the intracrystalline biopolymers inside the platelet do not show piezoresponse. In the LPFM, the amplitude image [Fig. 5.6(d)] shows opposite contrast to that of the VPFM image [Fig. 5.6(b)]. In this case the intracrystalline biopolymers have the strongest piezoresponse. The LFPM on the cross-sectional nacre is along the [001] direction of aragonite platelet. The result agrees with the findings from the nacre surface that the polarizations of intracrystalline biopolymers are along the direction perpendicular to the platelet surface, and the piezoresponse is the strongest along this direction. On the other hand, the interlamellar biopolymers contain a chitin core, and silk-fibroin-like and negatively charged aspartic acid-rich proteins may be in the peripheral of the chitin core (Marin and Luquet, 2004; Heinemann, Treccani and Fritz, 2006; Bezares, Asaro and Hawley, 2010). This kind of biopolymers shows strong piezoresponse in the direction parallel to the platelet surface.

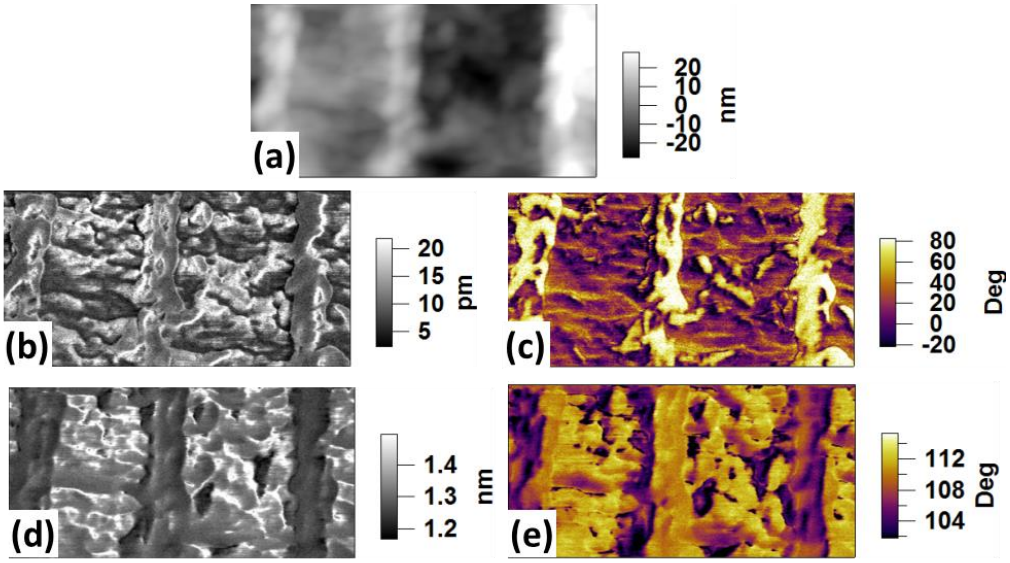

Fig. 5.6 DART-VPFM [(b) and (c)] and -LPFM [(d) and (e)] images observed from the cross-sectional nacre surface (800 × 400 nm^2, 512 × 256 pixels). (a) height, (b) and (d) amplitude, (c) and (e) phase.

5.3 Piezoelectric response of Clam shell

5.3.1 PFM Images and d_{zz} Evaluations of Fresh Clam Shell

For all of PFM observation, the tested samples were made from the same piece of clam shell to exclude the age effect. Three sets of images were taken from either the outer shell surface or the cross-sectional surface. Each set of PFM observation comprises five images: height/topography, amplitude (proportional to piezoelectric constant), phase (polarization direction), Q-factor (energy dissipation), and frequency (relative stiffness) images. These images are generated from the DSHO fitting of the raw data of the piezoresponse (described in Chapter 2). This method can reveal the relative piezoelectric constants, the frequency independent polarization orientations of the ferroelectric materials and simultaneously quantify the nanomechanical characterizations of sample surface (Gannepalli et al., 2011). The local piezoresponse of the clam shell is shown in Fig. 5.7. All topographic images [Figs. 5.7(a), (f), and (k)] show oval-shape nanograins, which are described as

the 4th level structure or the smallest feature in the clam shell structure. As the piezoresponse of clam shell on the macroscale are expected to be originated from the collective responses of the basic building blocks, this study mainly focus on the piezoresponse behavior of clam shell on the nanoscale.

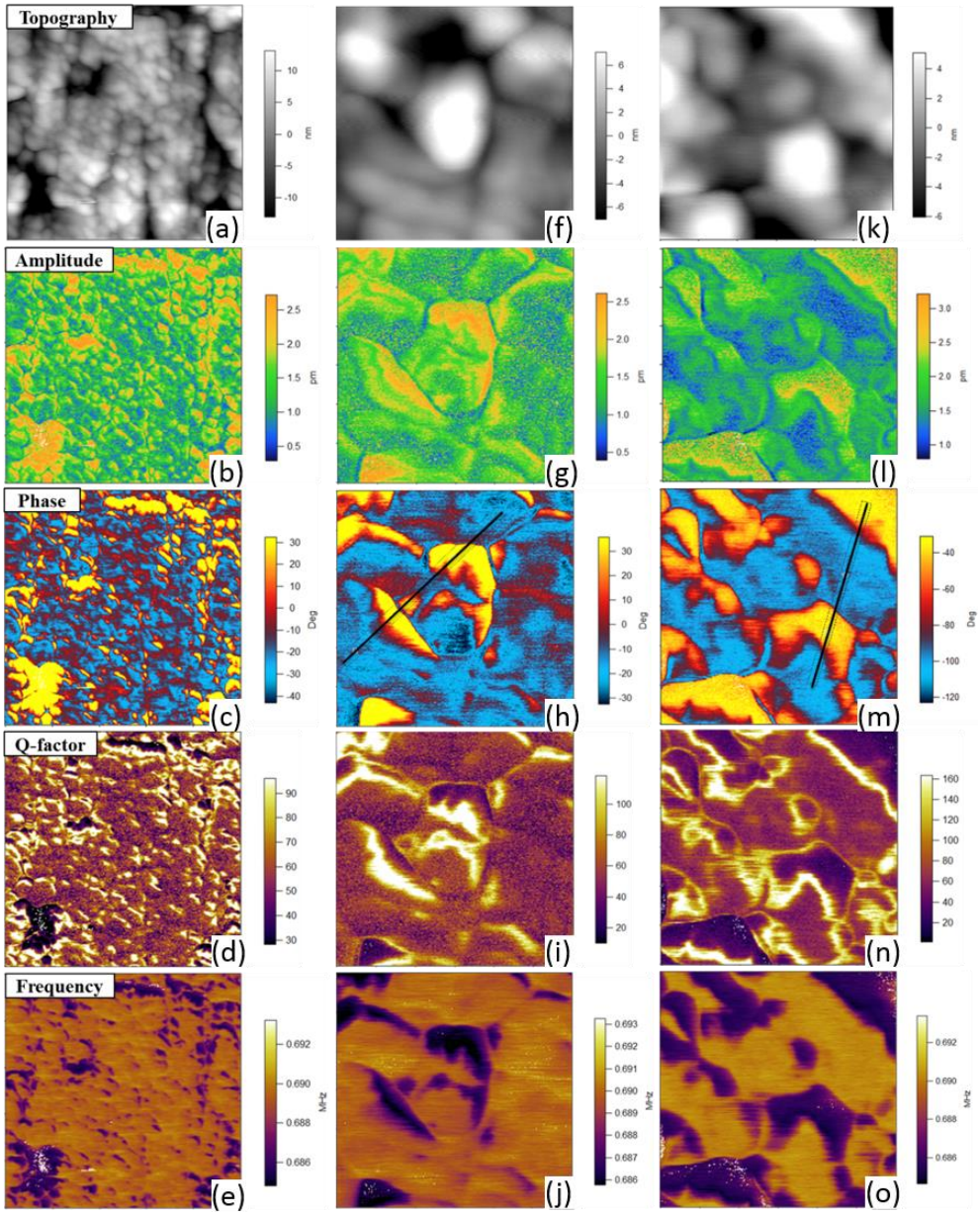

Fig. 5.7 DSHO fitted DART-PFM images of clam shell. The drive amplitude is 4 V_{ac} for all images. Images in the 1st (1×1 μm^2) and the 2nd (300×300 nm^2) column are observed on the outer surface of clam shell, while the images in the 3rd (300×300 nm^2) column are observed on the cross-sectional surface. The lines on Figs. (h) and (m) are to be explained on Fig. 5.4. (Probe: PPP-NCSTPt, k_c = 8.23 N/m)

In Fig. 5.7, the amplitude image demonstrates the relative strength of the local piezoresponse. Figs. 5.7(b), (g), and (l) show the piezoresponse over the different levels of structures, ranged from about 0.5~3.5 pm. The strongest piezoresponse (yellow-color in the amplitude images) is expected to be originated from the biopolymers because of their complex polar structure. Most of the amino acid residuals extracted from the biopolymers of mollusk shell have already been proved to exhibit piezoelectricity. Similar to the case of abalone shell, $CaCO_3$ should not exhibit any piezoresponse due to its centrosymmetric structure. Therefore, the strong piezoresponse observed on the nanograins should be mainly from the displaced biopolymers that are dragged to cover the grain surfaces after polishing process. These regions are usually near grain boundaries or deep grooves on the surface. There may also be biopolymer residuals intercalated inside the nanograin crystals after the biomineralization process, which may cause the weak piezoresponse observed from the middle regions of nanograins (blue-color in amplitude images). Some correlations between the amplitude [Figs. 5.7(b), (g), and (l)] and topographic [Figs. 5.7(a), (f), and (k)] images can be observed. Ideally, DART-PFM can track the contact resonance frequency shift caused by the surface roughness and stiffness changes, and thus reduce or eliminate the topographic crosstalk. This frequency shift at different locations is tracked in the frequency images [Figs. 5.7(e), (j) and (o)]. However, if the height difference is too large, DART technique may not work well, and the topography may still have effects on the amplitude images, for instance, at the boundaries of large grains. This problem usually associates with clam shell but not in the abalone shell because the clam shell has much larger grain size. Furthermore, the regions with different

levels of piezoresponses also have distinct phase contrasts accordingly. The phase image directly measures the phase lag angles (θ) of the piezoresponse signal against the drive signal (V_{ac}). In these images, the values that can be quantified are the relative differences in θ among various locations within the phase image. For materials having perfect opposite vertical polarizations, the relative difference of θ should be 180 º. For clam shell, the maximum phase differences that observed between the yellow- and blue-color regions are about 60 ~70 º[Figs. 5.7(c), (h) and (m)]. This implies the existence of the lateral polarization vectors (which are not studied in this work). In addition, the Q-factor image [Figs. 5.7(d), (i) and (n)] reveals the energy dissipation or loss of the tip-sample interaction. The smaller the value is, the more energy is dissipated or the system is more damped if simulate it as a damped harmonic oscillator. In other words, the total energy stored (kinetic and potential) in the tip-sample oscillator system is minimum. Lastly, when compare the PFM images from the outer shell surface [Figs. 5.7(f)-(j)] to those from the cross-sectional shell surface [Figs. 5.7(k)-(o)], no significant difference in piezoresponse is observed on the nanoscale. Clam shell shows relatively uniform structure at this level and its property deviations due to the directionality may not be so significant.

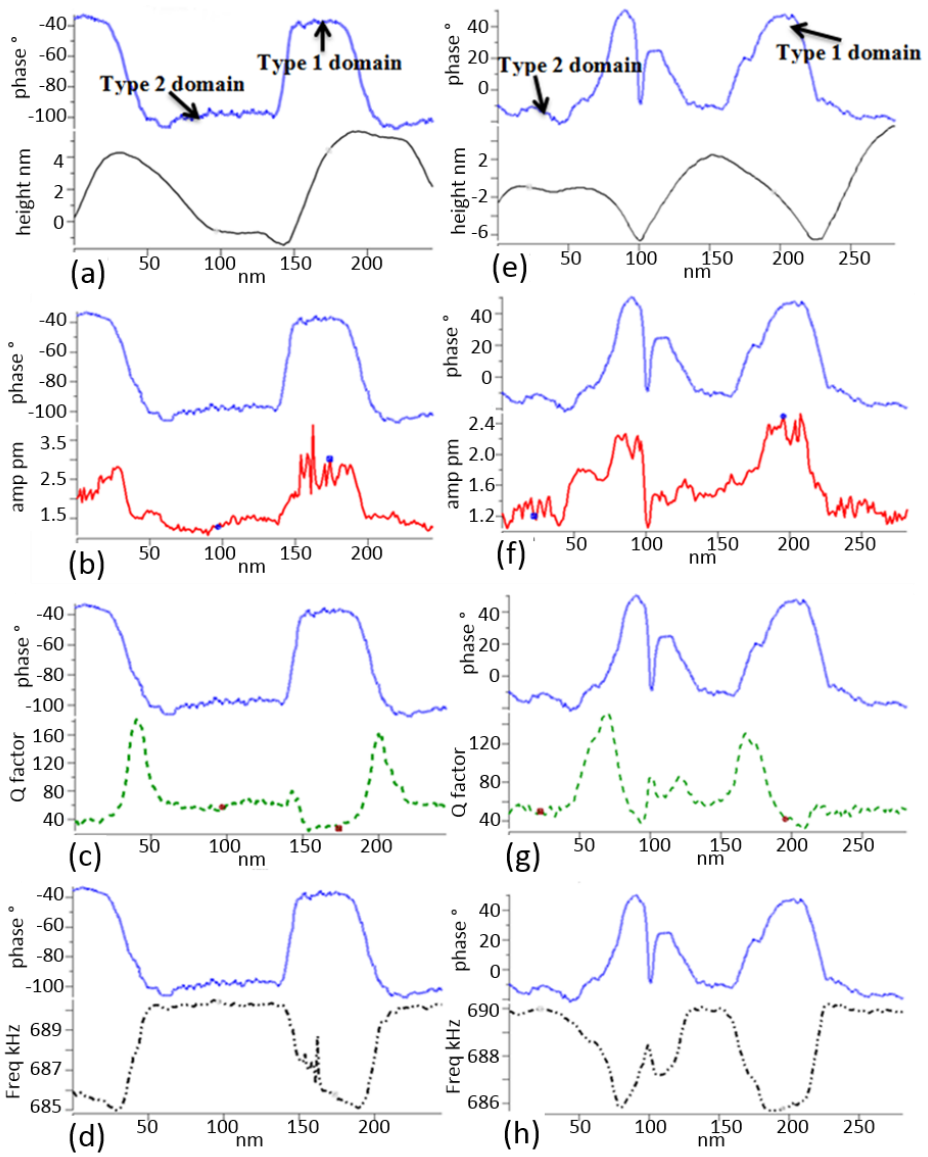

Fig. 5.8 Data curves along line sections in Fig. 5.3(h) and (m). Data in 1st and 2nd columns are obtained from the cross-sectional shell surface and the outer shell surface respectively. (a) and (e) are height curves, (b) and (f) are amplitude curves, (c) and (g) are Q-factor curves, (d) and (h) are resonance frequency curves.

To further study the corresponding relations among the topography, amplitude, phase, Q-factor, and resonance frequency, the data points of these five images at the exactly same locations [along the solid line section in Figs. 5.7(h) and (m)] are displayed and compared in Fig. 5.8. The phase offset data are taken as the reference curve and shown on each figure. It is clear that two

types of domains always exist on the two surfaces. The phase angle difference between these domains is all around 60 º. The domains near grain boundaries usually show either more positive or less negative phase angles [defined as type 1 domain in Figs. 5.8(a) and (e)]. In Figs. 5.8(b) and (f), the amplitude has the similar trend as the phase angle. The regions of high amplitude always associate with the type 1 domain, which implies the high biopolymer contents at grain boundaries. The overall piezoelectric amplitude observed from the local cross-sectional surface (1.1~3.0 pm) is slightly higher than that observed from the local outer shell surface (1.1~2.4 pm). In addition, the frequency curves [Figs. 5.8(d) and (h)] have the exact opposite trend as compared to the reference curves. This means that the contact resonance frequency of type 1 domain (~686 kHz) is lower than that of type 2 domain (~690 kHz), and they are directional independent, i.e., the similar values can be obtained on both outer shell and cross-sectional surfaces. The contact resonance frequency shift reveals the stiffness difference on the sample surface. Stiffer regions usually show higher frequency. It is well known that biopolymers are less stiff than that of the mineral phase. Thus, the lower frequency is expected to be associated with the biopolymer concentrated regions. On the contrary, the mineral phase should exhibit higher resonance frequency. This also agrees with the previous finding on the amplitude curves that the type 1 domain exhibits stronger piezoresponse and should be originated from the biopolymers. In addition, as mentioned earlier that the Q-factor is an indicator of the energy dissipation of the tip-sample interaction. It measures the damping level of the system. Lower value in the Q-factor image means more energy is dissipated, or the cantilever is more damped. The type 1 domain

(biopolymers region) shows lower Q-factor value (~40) than that of the type 2 domain (~60). Therefore, the soft biopolymers should be able to absorb more energy than that of the stiff mineral phase when interact with the same probe. However, there are usually spikes in the Q-factor curves (130~160) at the transitions between the type 1 and type 2 domains. These highest Q-factor positions correspond to the red-color regions in the phase images [Figs. 5.7(h) and (m)]. The responsive amplitudes corresponded to these regions stay at relatively low values. It suggests that there is gradual transition between the different domains in clam shell, similar to that in the abalone shell, but different from the traditional piezoelectric materials which usually have abrupt domain transition with only a few nanometers width of domain walls. The reason of this may be that the individual domains are formed by material with different compositions in the clam shell. This gradual domain transition region may due to the interpenetration between the biopolymers and mineral phases, and together they result in the lowest energy loss. Thus, the effective area of piezoelectric and mechanical responses from biopolymer is larger than the actual size of the biopolymer.

In addition, the effective local piezoelectric constant d_{zz} has been measured at random locations on both outer and cross-sectional surfaces by single point method. In this case, all of the responses have been fitted by DSHO model. Thus, the values of d_{zz} are the quantified true sample response. For polished fresh clam shell, it is found the quantified d_{zz} for outer shell surface is 0.29 ± 0.05 pm/v, whereas for cross-sectional surface it is 0.26 ± 0.08 pm/v. The d_{zz} of x-cut quartz measured in the same way (also by DSHO

fitting) is around 0.25 pm/v. Therefore, the d_{zz} of clam shell is comparable to that of quartz, and is also similar to the $-d_{14}$ value of tendon (Fukada, 2000).

5.3.2 Piezoresponse of Deproteinated Clam Shell

In addition, to verify the findings that the biopolymers are the origin of the piezoelectric response in clam shell, the partially bleached samples have been tested. The same samples for the previous tests are used to subject the chemical treatment to remove the biopolymers. The bleached samples maintain their integrity and part of the biopolymers on the sample surface are removed. The d_{zz} obtained from the bleached outer shell surface is 0.21 ± 0.04 pm/V, and on bleached cross-sectional surface, it is 0.18 ± 0.07 pm/V. Therefore, the overall piezoresponse is reduced when the biopolymers are partially removed. In addition, the piezoresponse obtained from PFM images are compared between the fresh polished and bleached samples. The histogram curves of the responsive amplitude and phase data from the fresh and bleached clam shells are shown and compared in Figs. 5.9(a) and (b) respectively. The amplitude curve of the bleached sample [red curve in Fig. 5.9(a)] is found to be shifted towards the lower value regions with respect to that of the fresh polished sample [green curve in Fig. 5.9(a)]. The mean amplitude value after Gaussian fitting is 0.34 pm and 0.21 pm for fresh and bleached samples respectively. Thus, the piezoresponse is reduced due to the partial removal of the biopolymer from the surface. As mentioned previously that the maximum relative phase lag is about 60 ~ 70 °between mineral and organic phases. This is shown by the green curve in Fig. 5.9(b). The highest peak at -20 °is found to associate with the mineral phase, while the small peak

at more positive value 45 ºshould be engendered by the biopolymer phase. However, for bleached shell sample, only one peak persists. The missing peak should represent the domain originated from the biopolymers on sample surface, and disappears due to the bleach treatment. All of the above findings have verified that the strongest piezoresponse of clam shell is originates from the biopolymer phase located between the nanograins. The biopolymers intercalated inside nanograins may not be able to be removed easily. Therefore, the shell surface still exhibits certain piezoresponse even after the bleaching treatment.

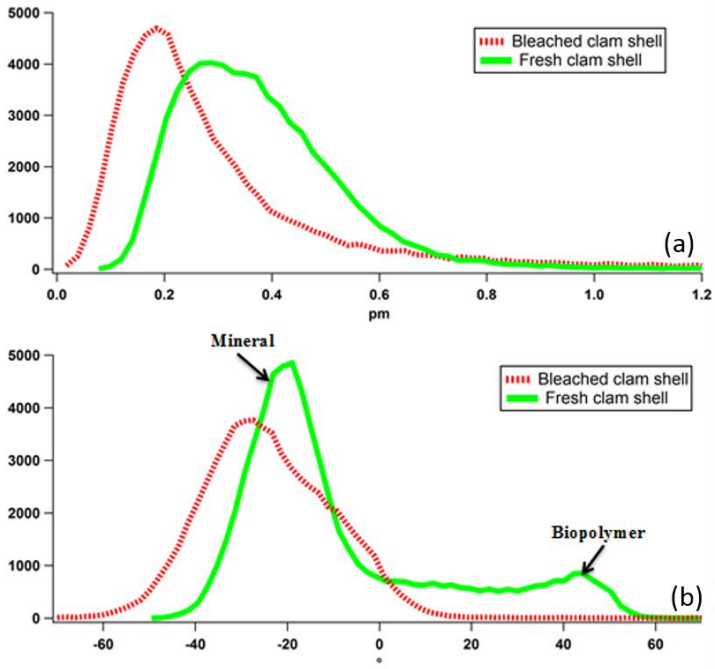

Fig. 5.9 The histograms of amplitude and phase data comparisons between fresh and bleached clamshell. Curves show data distributions from two 1×1 μm^2 DSHO fitted PFM images. One is observed from the fresh clam shell, while the other is observed from the bleached clam shell, both are from the outer surface. (a) Amplitude data distributions at 1 V_{ac}, and (b) phase data distribution. Vertical axes stand for the number of data points (256×256) in a PFM image, while horizontal axes show the data value range.

5.4 Summary

This chapter has reported the fundamental piezoelectric behaviors of fresh and deproteinated abalone and clams shells. In addition, clam shell has more uniform structure and homogeneous properties than that of the abalone shell. Thus, the vector PFM has been studied on abalone nacre. As expected, the piezoresponse of nacre surface are highly directionally dependent. Intracrystalline biopolymers usually show strong piezoresponse along the direction perpendicular to mineral platelet. Interlamellar biopolymers show strong piezoresponse in the direction parallel to the platelet.

In addition to the piezoresponse, the locations of biopolymers inside mollusk shell on the nanoscale can also be detected by the PFM technique in a non-destructive way, which is unachievable by other characterization techniques. The inherit piezoresponse of biopolymers in nacre can perform the sensing and even actuating roles associated with various biological, physiological and mechanical behaviors. Nevertheless, unlike the synthesized molecular piezoelectric and ferroelectric crystals whose composition, molecular structure and symmetry can be clearly identified (Fu et al., 2013), one of the great challenges for the in-situ piezoelectric characterization on fresh mollusk shell is to determine the exact combination and orientation of the biopolymers. It is worth noting that vector PFM is insightful only when the symmetry of the sample is known. For lower symmetry material, which biopolymer is likely to be, an out-of-plane polarization can give both normal and shear piezoelectric strain.

Chapter 6

Ferroelectric Behaviors of Abalone and Clam Shells

CHAPTER 6 Ferroelectric Behaviors of Abalone and Clam Shells

Besides piezoelectricity, ferroelectric behavior has also been observed in some biomaterials. However, the ferroelectric behaviors from biological materials have been through long debates. Although the behaviors have been observed experimentally and a ferroelectric model has also been proposed for cells and neurons, many artifacts are known to play possible roles, particularly, hysteresis loops that may be observed in any nonlinear dielectrics with losses (Lemanov, 2000b). This chapter clarifies the intrinsic ferroelectric properties of biomaterials, based on the studies of mollusk shells. The experimental setups that may affect the appearance of the hysteresis loops have also been studied.

6.1 Ferroelectric Hysteresis Behaviors of Abalone Shell

6.1.1 Low Voltage Hysteresis Loop Observed on Nacre

Local ferroelectric hysteresis loops were firstly successfully obtained from the inner surface of nacre under the relative low applied voltage, the maximum sum of AC and DC biases can be applied is ±10V.

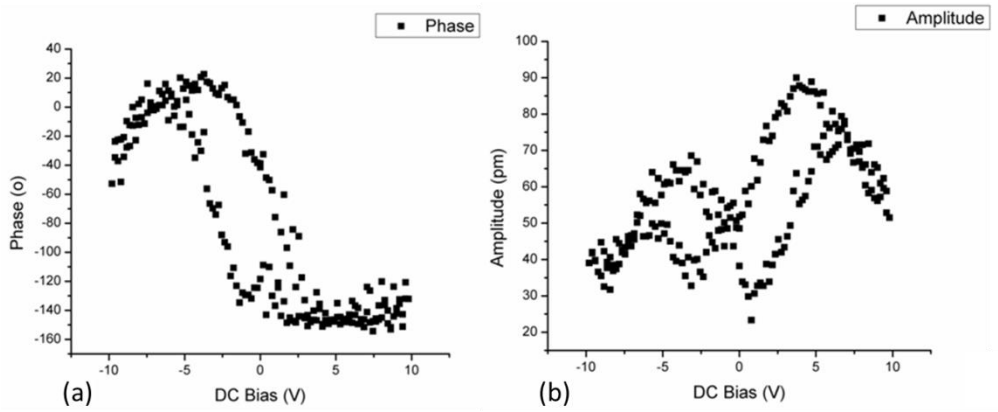

Fig. 6.1 Raw SS-PFM phase (a) and amplitude (b) loops observed from inner surface of polished fresh nacre. V_{ac} = 3V, V_{dc} = 10V. Probe: AC240TM

Fig. 6.1 shows raw data of the phase and amplitude in a single loop measured by SS-PFM method. As mentioned in Chapter 2, phase shift represents the polarization switching, while amplitude represents deformation or strain. The near 180 °of maximum phase inversion and the "butterfly" shape of amplitude loop provide the first evidence of ferroelectric behaviors of nacre. However, the loop shapes are different from that of the traditional ferroelectric non-biological materials, manifested as the highly non-symmetric strain loop and non-clear saturation on the phase loop. The positive voltage induces more deformation. Moreover, the "bend over" of both amplitude and phase loops near the saturation are mainly due to the low DC voltage in the control system. However, it also suggests that the ferroelectric behavior of nacre may be non-linear. Other factors such as the increased electrostatic attraction force and ionic motion at high DC voltage may also contribute to the reduction in the detected strain and phase shift. Although it is not possible to observe the hysteresis loop in every position of the sample, it still reveals the ferroelectric property of nacre in certain extent.

6.1.2 HV Hysteresis Loops Measurement on Nacre

By incorporating HV attachment in the PFM system, the hysteresis loops were acquired again on both cross-sectional surface and inner surface of nacre. In addition, the loops from both vertical and lateral response were obtained. A typical AC embedded DC triangle cycle is used as the drive signal (Jesse, Lee and Kalinin, 2006). The DART method is still used to detect the piezoelectric amplitude and phase, and all the hysteresis loops are recorded during the DC-off pulse. Both amplitude (A) and phase shift (φ) of the response signal can be recorded directly as the function of the DC bias cycles. To ensure a complete switching of the polarization, the minimum DC bias windows were chosen so that the phase angles were rotated by 180 °. To prevent the damage to mollusk shell sample, the maximum bias was maintained less than 100 V_{dc}. The durations of both DC-on (local poling) and DC-off (data acquisition) are fixed at 24.5 ms. Data acquisition speed is set to be 2 kHz. The ferroelectric hysteresis loop (PR loop) is calculated from the relation of $A \times \cos(\varphi)$ (Kalinin et al., 2010), where A is measured in pm and θ is measured in radian. It has been reported that the PR loops usually demonstrated good agreement with the macroscopic P-E measurement (Rodriguez et al., 2010). All of the loops presented in this study are smoothed by the adjacent-averaging method, and all tests are performed with the same conductive probe (ASYELEC, Asylum Research, USA) whose calibrated stiffness is 1.4 N/m, and the identical laser position on the cantilever.

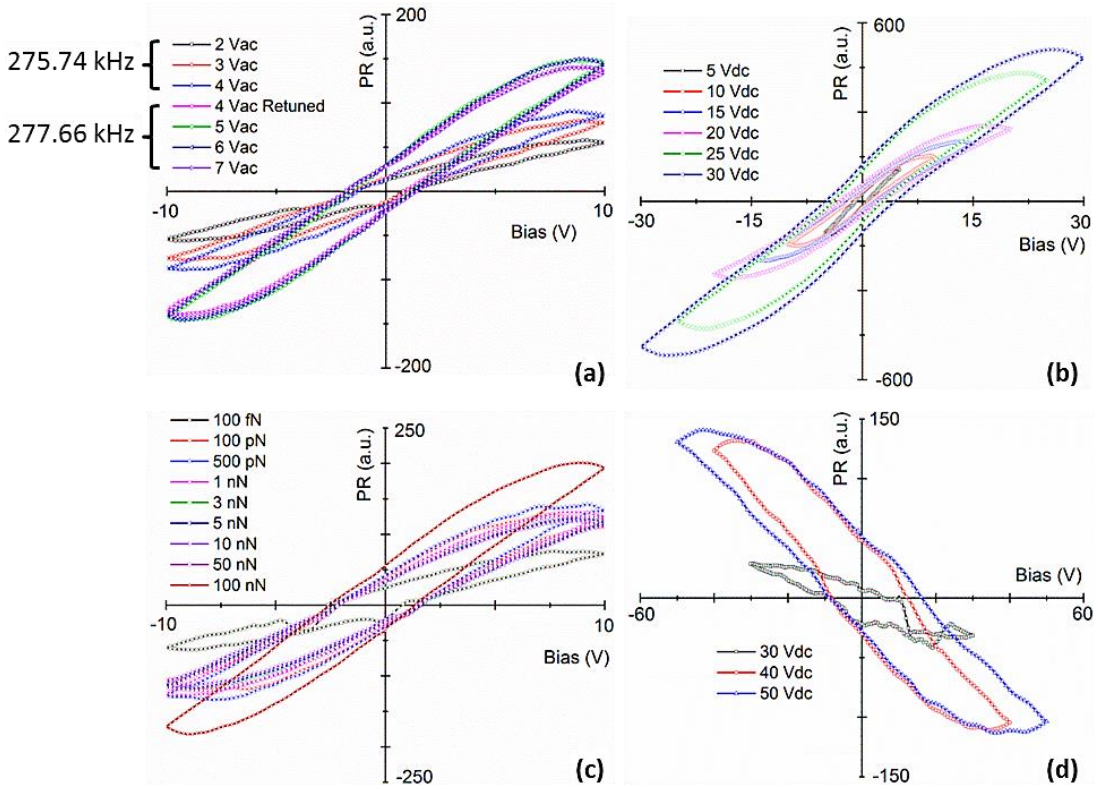

Fig. 6.2 PR hysteresis loops that acquired on cross-sectional surface of abalone shell (nacre section). Vertical PR loops demonstrating the effect of increasing AC drive amplitude (a), the effect of increasing DC bias window (b), and the effect of different tip-sample force(c), lateral PR loops are shown in (d)

Fig. 6.2 shows the hysteresis loops that obtained from *cross-sectional surface of nacre*. Many factors may affect the shape of the loops, such as the extent of DC bias window (V_{dc}), AC drive amplitude (V_{ac}), drive frequency, and the trigger force (the force experienced between tip and sample during the SS-PFM acquisition). During the SS-PFM acquisition, DART method is used for detecting the local change of A and θ after the localized poling by V_{dc}. The resultant hysteresis loops by only varying V_{ac} and holding other parameters to be constants are illustrated in Fig. 6.2(a). The hysteresis loop is analyzed in the same way as described by Jesse, Baddorf and Kalinin (2006). It is found that both positive and negative coercive biases are nearly not affected by

increasing V_{ac}, but the maximum switchable PR is altered. In addition, the drive frequency also influences the shapes of the hysteresis loop and its characteristic values. The hysteresis loops in Fig. 6.2(a) are obtained at two different frequencies near the contact resonance frequency. To set the second drive frequency properly, the PR is retuned to get the amplitude-versus-frequency curve with latest settings. The value of the second drive frequency is set only 2 kHz larger than the first one. With the identical drive signal, the hysteresis loops at slightly different frequencies [4 V_{ac} and 4 V_{ac} retuned in Fig. 6.2(a)] show significant changes in the maximum switchable and remanent PR. In addition, the hysteresis loop is slimmer and the work of switching (defined as the area enclosed by hysteresis loop) is smaller when it is acquired at lower frequency. Therefore, it can be concluded that drive frequency is one of the factors that affects the value of remanent PR (at zero bias), while the maximum switchable PR can be altered by adjusting the drive amplitude or drive frequency. Moreover, at a fixed drive frequency, when V_{ac} reaches a critical value (4 V in this case) the hysteresis loops are identical regardless of further increment of V_{ac}. Thus, 4 or 5 V_{ac} is used for all the subsequent measurements to avoid any artificial effects from the drive amplitude.

Fig. 6.2(b) illustrates the hysteresis loops that obtained under different V_{dc}, ranging from 5 V_{dc} to 30V_{dc}. All of the characteristic values associated with hysteresis loop, including coercive bias, maximum switchable PR, remanent PR and work of switching, are increased along with the rise of V_{dc}. The changes of the coercive bias and remanent PR are shown in Fig. 6.3. Both the positive and negative coercive biases are increased linearly with the DC

bias, while the positive and negative remanent PR are increased with the DC bias in an approximately second order polynomial relation. The shifts of the hysteresis loops along the vertical and horizontal axes are represented by the differences between the two remanent PR curves and the differences between the two coercive bias curves respectively (Fig. 6.3). The larger the shifts, the stronger the internal fields are. This shift may be caused by the highly orientated biopolymer domains. As all of the loops are obtained at the selected points with the strong PR, these locations should have highest biopolymer concentration (Li and Zeng, 2012). It is found that the shape of the hysteresis loops obtained from the abalone shell is similar to the macroscopic P-E loop observed from the P(VDF/TrFE/CTFE) terpolymer which usually shows promise of great energy storage and fast discharge ability (Chu et al., 2006; Zhang and Chung, 2007). In addition, the hysteresis loops measured from the cross-sectional nacre surface can still maintain their slim shape even under high V_{dc}. This reveals the possibility that the biopolymers in nacre may exhibit the similar energy storage and discharge functions as that of the synthetic biopolymers, which may also promote the increased toughness of mollusk shell.

It is worth discussing in more detail on the hysteresis loop obtained from mollusk shells. Firstly, it is much easier to obtain a saturate hysteresis loop in mollusk shell (in certain orientations) compared to that of the other conventional inorganic or organic piezoelectric materials (such as PZT and PVDF) at a relatively low applied bias (± 10 V_{dc}). This indicates that the ferroelectric domains in the mollusk shell can be easily switched under electrical field or being trigged by mechanical stress. Schneider (2007) has

discussed the “domain switch toughening” mechanism for certain ferroelectric ceramics. He showed that the toughness change under applied electric field in poled ferroelectric ceramics was due to domain switching, and reported that an increase in fracture toughness of up to 100% could be expected for materials poled parallel to the crack orientation (Schneider, 2007). Furthermore, it was also reported that the critical electrical energy release rate could be more than 10 times higher than the measured critical mechanical energy release rate for some materials (Zhang, Zhao and Liu, 2004), this further confirms the domain switching toughening mechanisms. To apply the same scenario to the observed piezoelectricity and hysteresis loop in mollusk shell structure, the results suggest that the mollusk shell may have some intrinsic mechanisms resulting in “domain switching toughening” under external stresses. Therefore, the effective stresses acting on the shell structures are effectively reduced; this may be one of the mechanisms leading to the high mechanical performance of the mollusk shell structure. Of course, this argument is somewhat speculative at the moment, the effects of “domain switching toughening” still need more detailed study, especially theoretical and numerical simulations.

The second point is the shape of the hysteresis loop. It is well known that, for dielectric materials, the energy density storage and loss can be computed from the area enclosed in the hysteresis loop of the polarization versus applied electrical field hysteresis loop (Chu et al., 2006; Zhang and Chung, 2007; Zhang, Meng and Chung, 2009). Comparing the hysteresis loop of the mollusk shell to what reported in the literatures, it is found that the shape of the hysteresis loop of the mollusk shell represents high energy storage and energy release, which is similar to many synthetic polymers for

energy applications (Chu et al., 2006; Zhang and Chung, 2007; Zhang, Meng and Chung, 2009; Wang et al., 2010). The hysteresis loops of these polymers with large electric energy density are required to have high electric displacement or charge density and very small remnant polarization. Therefore, these polymers usually have slim and tilted shape of hysteresis loops, which are very similar to those obtained from the abalone shell.

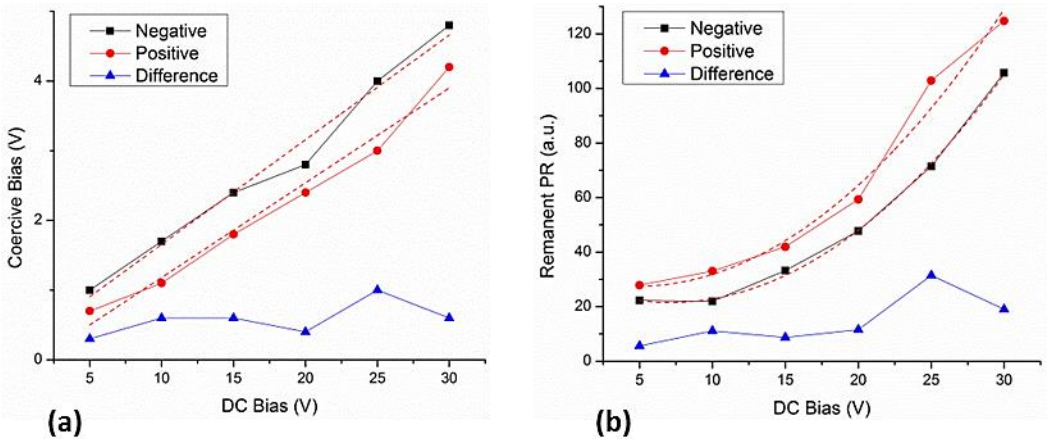

Fig. 6.3 Changes of coercive biases and remanent PR along with rise of DC bias. (a) positive and negative coercive bias fitted with linear lines, (b) positive and negative remanent PR with 2nd order polynomials fitting.

On the other hand, the mechanical contact force between the SPM tip and sample can affect the electric field distribution and further influence the shape of hysteresis loops. Fig. 6.2(c) illustrates the hysteresis loops observed under different trigger forces. The range of the loading force is set to be from 100 fN to 100 nN. No hysteresis loops can be observed beyond this range. At low force load, such as 100 fN, the surface morphology may have significant effects due to the non-firm contact between tip and sample so that bumps are formed along the hysteresis loop. On the other hand, at high force load, such as100 nN, the maximum switchable PR is significantly increased, which may

due to the strong interaction between the electric field and the tip-induced stress field. However, the coercive fields are not affected by different trigger forces. Within the range of 1 nN ~ 50 nN, all of the hysteresis loops nearly coincide. Therefore, the trigger force is set to be 5 nN for all the subsequent measurements.

Fig. 6.2(d) shows the hysteresis loops by LPFM measurement on the cross-sectional surface of nacre. In this case, the electric field is applied in the vertical direction, but the detected strain and polarization switching is in the lateral direction. Thus, it represents the shear strain alteration with the DC bias. There are many differences between the hysteresis loops measured in the vertical and lateral directions. Firstly, higher V_{dc} is required to have a saturate phase loop (phase rotates by 180 °). Secondly, much higher coercive bias is observed in the lateral direction than that in the vertical direction with the same DC bias window. Thirdly, the maximum switchable PR of the LPFM hysteresis loop is reduced (~250 with 40 V_{dc}) and hence more works are required to rotate the dipoles to get a complete hysteresis loop in the lateral direction. Fourthly, the hysteresis loops from LPFM measurement are not as smooth as that from VPFM measurement, which may due to the tip-sample frictional force. In addition, unlike the hysteresis loop in the VPFM measurement, when V_{dc} increases, the imprint becomes larger accordingly. This is due to that only the positive coercive bias is increased as the negative coercive bias remains at a constant value. This suggests that there should be a preferential state of the biopolymer dipoles that does not change with increasing electric field. Furthermore, the hysteresis loops from LPFM measurement are orientated in an opposite direction in contrast with that from

the VPFM measurement. This inversion is directly due to the opposite behaviors of the polarization direction switching as illustrated in Fig. 6.4(a). Although both the phase loops show about 180 °altered phase angle, the angle switching paths are in the opposite directions as indicated by two arrows. For the phase loop in lateral direction, there is a turn-over spot, at which the polarization directions switch back to the original direction and keep increasing in the opposite direction. There may be an interim unstable polarization direction (about 0 °in this case) induced by the bias. With the increasing local poling field, the polarization may switch to the opposite stable direction and grow continuously. It has been reported that the inversion of the PR hysteresis loops can be controlled by either electron or hole injection in certain materials (Li et al., 2011). This inversion phenomenon definitely worth more sophisticated studies on nacre structures in the future. Finally, Fig. 6.4(b) illustrates that the lateral loop has significantly smaller maximum amplitude/strain than that of vertical loop. Since the value of amplitude controls the magnitude of hysteresis loop, higher maximum amplitude results in larger maximum switchable PR. In comparison, the ferroelectric hysteresis loops have been successfully acquired from synthesized organic materials on the nanoscale, including those for γ−glycine (Isakov et al., 2010; Heredia et al., 2012; Sencadas et al., 2012). These loops have various shapes, and the majority of them are not symmetric about the zero-bias axis. The coercive biases are about double of the value that was reported here in the vertical direction, but very similar to the value obtained in the lateral direction. Therefore, the hysteresis loops observed here may be associated with more than one type of biopolymers in nacre.

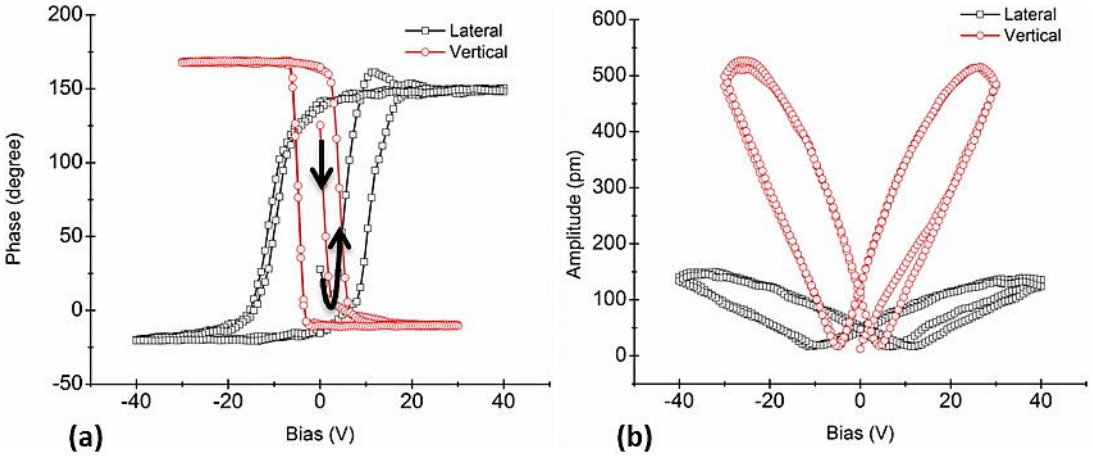

Fig. 6.4 Different phase and amplitude responses from vertical and lateral SS-PFM. (a) phase loops, and (b) amplitude loops.

The hysteresis loops have also been acquired on the *platelet surface of nacre* at selective positions. Because of the similar shapes of all the hysteresis loops, the average hysteresis loops are shown in Fig. 6.5 with standard deviations from six different locations. The hysteresis loops observed here are greatly diverse from those observed on the cross-sectional nacre. The only similarity is the inversely orientated hysteresis loops between the VPFM and LPFM measurements. In Fig. 6.5(a), there are large deviations at the saturation regions of the loops, and it significantly affects the maximum switchable PR. Similar to the studies from the cross-sectional surfaces, many factors, including the drive frequency, drive amplitude, and trigger force can affect the shape and characteristic parameters of the hysteresis loop. Here the loops are acquired with the same settings as described for the cross-sectional surface, thus, the frequency can be the primary reason for this larger deviation value (slightly different contact resonance frequency at different locations). Other characteristic parameters can remain consistent even the measurements are made at different locations. In contrast to the hysteresis loops on

cross-sectional surface, the hysteresis loops from inner surface in the vertical direction show large shifts along the vertical and bias axes. The vertical shift of the hysteresis loops was usually interpreted in terms of a non-switchable layer (Alexe et al., 2001; Rodriguez et al., 2010). In case of the nacre surface, the non-switchable layers may be the $CaCO_3$ nanograins. On the other hand, the horizontal shift may be due to the aligned internal fields originated from the local preferentially oriented defects pointing in approximately the same direction (Damjanovic, 1998). Conversely, the hysteresis loops from LPFM measurement [Fig. 6.5(b)] are found to be symmetric and the shifts along vertical and horizontal axes are very small. But these loops have totally different shapes compared with those observed from the nacre region, indicated by the clear nucleation points (sudden change of the slope of hysteresis loop). Their shape resembles to the macroscopic hysteresis loops of P(VDF-CTFE) copolymer (Chu et al., 2006). The different shape of the hysteresis loops on inner surface are mainly due to the different amplitude/strain loops, as illustrated in Fig. 6.5(c). The amplitude loop obtained in the vertical direction shows slightly reduced value at high DC bias near saturation, which may be due to the electrostatic reaction. Among all the amplitude loops, the largest deformation is obtained from the cross-sectional surface in the vertical direction.

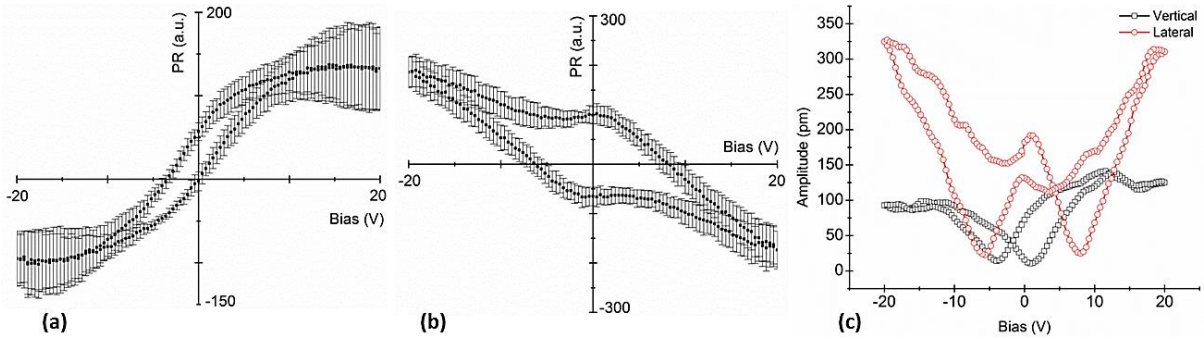

Fig. 6.5 Hysteresis loops acquired on the inner surface of abalone shell. (a) averaged hysteresis loops in the vertical direction, (b) average hysteresis loops in the lateral direction, and (c) representative amplitude loops.

6.1.3 HV Ferroelectric Hysteresis Loops of Calcite

The PR loops in the calcite region of the cross-sectional nacre has also been characterized [Fig. 6.6]. The overall shape of the loops in vertical direction [Fig. 6.6(a)] is similar to that of cross-sectional nacre [Fig. 6.2(a)], except that the maximum switchable PR is higher and the vertical shift and imprint is larger than that of nacre. On the other hand, the shape and characteristic parameters of PR loops obtained in the lateral direction is quite scattered, as shown in Fig. 6.6(b). There is no overall shape of the loops can be analyzed. Hence, the lateral PR loops in calcite are highly location-dependent. However, it is worth to note that the lateral loop orientation is the same as that of the vertical one, which is totally different from that in the nacre. In addition, the minimum bias window required for phase saturation is relatively low (20 V_{dc}) compared to that of nacre (30~40 V_{dc}). Lastly, the maximum switchable PR is at the same level as that of nacre. Therefore, the frictional force may be the main contributor of the limitation of the lateral strain.

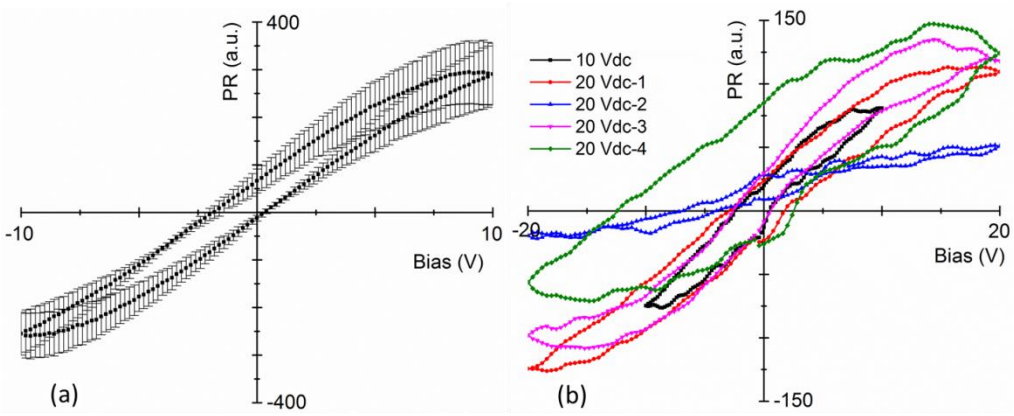

Fig. 6.6 Hysteresis loops acquired on the calcite region of cross-sectional abalone shell. (a) averaged PR loop in the vertical direction, and (b) a few PR loops observed in the lateral direction.

6.2 Ferroelectric Hysteresis Behaviors of Clam Shell

For clam shell, ferroelectric hysteresis loops are firstly collected as mapping at each point of a 64×32 mesh ($2\times1\,\mu^2$ area) on the outer shell surface (FS) and the cross-sectional surface (FC) of polished fresh shells. The variations of the remanent amplitude and phase values, i.e., the responses collected at the $V_{dc} = 0$ interval, versus DC bias cycle are captured. These data points forms the amplitude loop and phase loop, and the representative loops are shown in Fig. 6.7. Different DC bias windows are necessary to obtain fully saturated phase loops based on the different ferroelectric characteristics of the FS and FC samples. It was found that too high DC voltage usually causes permanent surface damage of the clam shell sample. Thus, the maximum bias is maintained at 100 V_{dc}. Figs. 6.7(a)-(c) and (d)-(f) are the representative hysteresis loops of the FS and FC samples respectively. All of the data points in the SS-PFM meshes (64×32 pixels) have the similar corresponding loops as those in Figs. 6.7(a)-(f), but with slightly different values of the critical properties. Different from the traditional ferroelectric materials, there is no clear nucleation point in the PR loops, which probably indicates very different

mechanisms of ferroelectric switching in the clam shell. For FS sample, a saturated phase loop can be easily obtained with relatively low DC bias window (±10 V_{dc}) [Figs. 6.7(a)-(c)]. On this surface, it was found that the overall shapes of the amplitude, phase, and PR loops persist even when bias is increased to 100 V_{dc}, but the values of coercive biases are increased with the applied DC voltage. On the other hand, the FC sample requires much higher DC bias to obtain a saturated phase loop, and it has much slimmer loops than those in the FS sample [Figs. 6.7(d)-(f)]. These loops have similar shape as the hard ferroelectric materials with highly pinched domain walls (Damjanovic, 2005). However, the phase loop does not saturate or reach stable states because no perfect horizontal lines can be observed no matter how large the DC bias is applied [circled region in Fig. 6.7(e)]. Additional mini loops are always observed at the expected saturation regions. All of the above observations indicate the highly aligned local dipoles inside the cross-sectional shell sample (Damjanovic, 2005). For both FS and FC samples, the coercive biases are around 0V and -4.5V. They can be directly viewed from the turnovers of the amplitude loops [e.g. point 1 in Fig. 6.7(a)]. The PR loops obtained from both sample are non-symmetric, and their remanent piezoresponse (when bias = 0) are all positive. Accordingly, the magnitude of the positive saturated piezoresponse is higher than that of the negative saturated piezoresponse. In addition, the PR loops are also shifted along the bias axis, which indicates that there might be local internal fields from the aligned defects dipoles (Damjanovic, 1998). Lastly, the work of switching for the FC sample is more than that of the FS sample, which means that the

energy loss or the energy consumed during domain switching is higher when observed from the cross-sectional surface of clam shell.

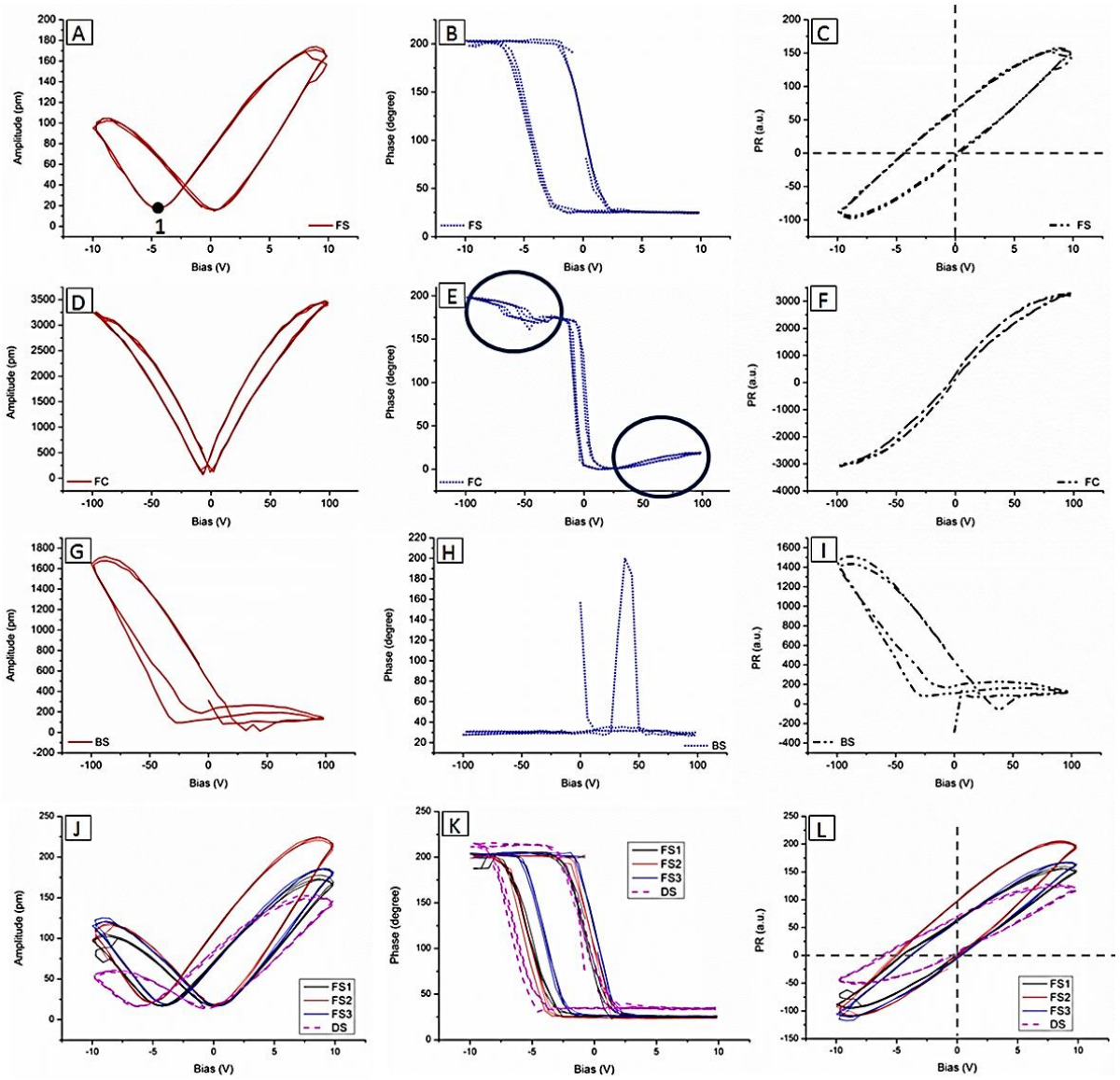

Fig. 6.7 Ferroelectric hysteresis loops (three bias cycles), including amplitude loop, phase loop and PR loop, of four different samples (FS, DS, BS, and FC). Graphs in the 1st, 2nd, and 3rd column are the amplitude loops, phase loops, and PR loops respectively. (a-c) from FS sample, (d-f) from FC sample, (g-i) from the BS sample, and (j-l) from the DS sample

Furthermore, ferroelectric hysteresis loops were also acquired from selective points on the outer shell surface (BS) sample bleached by using 10% NaOH solution, as well as the dried outer shell surface (DS) sample. The

bleached sample no longer exhibits any ferroelectric behavior because the polarization directions remain at the same level even when bias reaches 100 V_{dc} [Figs. 6.7(g)-(i)]. This result is expected because the biopolymers on the sample surface should be greatly removed by the chemical treatment. However, the BS sample still exhibits piezoelectric properties, which may due to the residual biopolymers inside the nanograins after the bleaching process. Therefore, this observation further confirms that the biopolymer phase is the origin of the piezoelectric property and the biopolymers that exposed on sample surface should be the main reason or mechanism for the ferroelectric properties in clam shell.

In addition, the DS sample has also been studied to determine the effect of moisture on the ferroelectric behavior of clam shell [Figs. 6.7(j)-(l)]. The hysteresis loops are acquired on the outer shell surface immediately after the sample being kept in furnace at 60 ℃ for two hours. This relatively low temperature is to prevent biopolymer degradations because the aspartic acid releases CO_2 at about 50 ℃ and the biogenic aragonite starts to release CO_2 at approximately 70 ℃ (Pokroy et al., 2006). The hysteresis loops acquired at different locations have quite consistent shape and characteristic parameters as shown in Figs. 6.7(j)-(l) by dashed lines. Three loops obtained from the fresh sample are plotted together with the one from dried sample for comparison. For the DS sample, 180 ^{o}switching of phase angle can still be achieved within the 10 V_{dc} bias. With the reduced moisture contents, both the coercive biases become slightly more negative and the maximum strains can be achieved are greatly reduced. In addition, the remnant piezoresponses do not change significantly, but the saturated piezoresponses are also dramatically reduced.

Therefore, the effects of the moisture in clam shell are slightly decreasing the coercive bias field and increasing the maximum switchable polarization, which is consistent with the finding by Fukada (2000), in which the macroscopic hysteresis loops observed from PVDF polymer showed higher coercive biases and smaller maximum switchable polarization under the condition that ionic conductivity was insignificant. Since the moisture promotes ionic conductivity, thus the EM coupling due to the ionic motion will be greatly reduced in dried clam shell sample. However, as the clam shell still exhibits ferroelectric hysteresis loop after dried, this is a further evidence to prove the existence of ferroelectricity in the clam shell. It is anticipated that sufficient energy needs to be consumed for the polarization switching process in the clam shell. When external mechanical stresses are applied to clam shell, internal electric fields can be generated because of the characteristics of the piezoelectric and ferroelectric properties, and the fields may further cause the domain switching process. Thus, part of the externally applied mechanical energy can be consumed by the intrinsic piezoelectric and ferroelectric responses, and it may further contribute to the toughening of clam shell. In this study, we propose this mechanism as the “domain switching toughening” by mollusk shell structure.

6.3 Summary

This chapter has reported the ferroelectric hysteresis behaviors of both clam and abalone (nacre and calcite sections) shells. The experimental parameters or settings, which affect the shape and characteristic parameters of the hysteresis loop, have been studied in details. Similar to the piezoelectricity,

the ferroelectric behaviors of mollusk shells are also directional dependent, and is originated from the biopolymers that exposed on sample surface. To verify that whether the ferroelectric behavior is primarily contributed by ionic motion or polarization, the dried clam shell has been characterized. It is confirmed that the ferroelectric behavior is the intrinsic property of mollusk shell.

To summarize, mollusk shell exhibits ferroelectric behavior, which is directionally dependent. During the polarization switching process, local deformation is accompanied, and energy can be stored and released (indicated by the area enclosed by the PR loop) at the same time. Together with the piezoelectric behavior, the "domain toughening mechanism" associated with nacre is proposed. When external mechanical impact or stress is applied, internal local electric fields can be induced be the external stress due to the piezoelectricity of nacre. This may assist to sense the strength and location of the stresses. In addition, these localized electric fields may also lead to the polarization switching processes in the biopolymers. Thus, mechanical energy is converted to electrical energy and may be either consumed or stored inside the mollusk shell. The stored energy could be released or consumed by certain unknown mechanisms. Therefore, it is believed that the piezoelectric and ferroelectric behaviors of nacre may also contribute to its extraordinary mechanical property, as well as the biological or physiological behaviors.

Chapter 7

Responsive Piezoelectric and Ferroelectric Behaviors to External Stress and Temperature

CHAPTER 7 Responsive Piezoelectric and Ferroelectric Behaviors to External Stress and Temperature

The previous two chapters expound the basic piezoelectric and ferroelectric behaviors and properties of fresh and chemically treated mollusk shells. This chapter will discuss the effects of the various external factors, including flexural stress and high temperature, on the biopiezoelectric and bioferroelectric phenomena of the mollusk shells.

7.1 Responses of Nacre to External Flexural Stresses

The experimental setup for this test has been presented in the Chapter 3. Using this set-up, the flexural stress is applied through the two point forces and delivered to the cross-sectional surface of the nacre by casted epoxy resin. The stress caused mechanical and electromechanical changes are presented in the following sections. The results presented in this section was published in the journal paper by Li and Zeng (2013).

7.1.1 Local Morphology Changes under Flexural Stresses

Typical layered structure of abalone shell is observed in the entire cross-sectional surface (Fig. 7.1). The thin white layers are where the interlamellar biopolymers are located, while the thick layers with embedded nanograins are the mineral layers (about 300~400 nm thick). In general, the outermost mineral layer is found about 100 nm thicker than that of the innermost ones (data not shown), which probably due to the shell growth sequence.

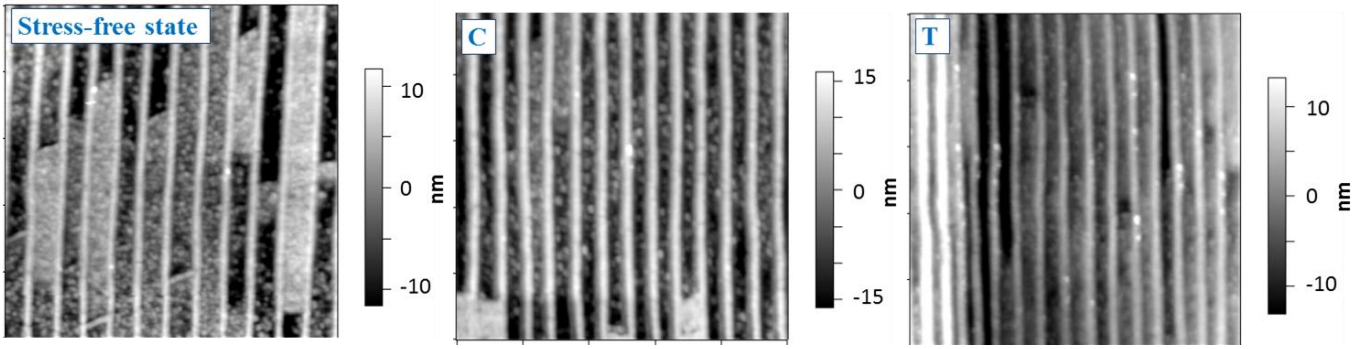

Fig. 7.1 Local topographic images under stress-free, compressive and tensile stress states by tapping mode. Image sizes are all 5×5 μm^2. C: Under compression; T: Under tension.

After polishing, it is found that the boundaries between the organic and mineral layers is about ~10 nm higher than the middle of mineral layers (this is named as bulging layers). This may be due to the intimate connections or interpenetrations of mineral and organic phases. Another possible reason is that the interlamellar biopolymer is slightly pushed out after the polishing process. In our set-up, when shell is subjected to flexural stresses, the outermost shell is under the maximum tensile stress, whereas the innermost shell is under maximum compressive stress, and the neutral axis is near the middle position between the outer and inner shell surfaces. Hence, in this work, the interested regions to be studied are those under the maximum tensile and maximum compressive stresses, as well as that near the neutral axis. The comparisons are primarily among these three regions. Fig. 7.1 shows the local morphological changes in the regions of stress-free, compressive, and tensile stresses. The imaging locations under compressive and tensile stresses are near the innermost and outermost layers of the cross-sectional nacre respectively. Thus, the associated stresses should be close to the maximum values obtained by FE simulations (page 42-43), i.e., 150 MPa and -140 MPa respectively. By exerting stress, the bulging layers generally become wider, even under

compressive stress. It is suspected that designed fixture may have some shear stress accompanied with the tensile or compressive stresses. Hence, the cooperation of these stresses may lead to the rotation of nanograins at the bulging layers and hence make them appears wider. In addition, the nanograins in the mineral layers apparently become larger under the compressive stress. These nanograins are surrounded by the intracrystalline biopolymer. Under compressive stress, the squeezed biopolymers may push out the bonded nanograins and make them looks larger. Conversely, the mineral layer under tensile stress looks more flat than that under stress-free state. The nanograins are less apparent because they may slightly sink into the intracrystalline biopolymer matrix at the tensile region.

7.1.2 Stress Affected Piezoresponse of Nacre by BE-PFM

Figure 7.2 shows the BE-PFM images of the regions under different stress states. The raw data $\{A, \varphi\}(\omega)$ at each pixel are fitted by DSHO approximation (Gannepalli et al., 2011) and four types of images are generated. Firstly, the amplitude image is composed by the piezoresponse amplitude (in pm) at the resonance frequency at each pixel. The amplitude value is proportional to the local piezoelectric constants d_{zz} with dimension of pm/V, which is defined as the field-induced deformation observed in the vertical direction while the electric field was applied in the same direction. Secondly, the phase image shows the responsive phase offset angle (in degree) with respect to the drive signal (V_{ac}) and reveals the local polarization directions at each pixel. Thirdly, the Q-factor image reveals the relative dissipative energy of the tip-sample interaction. Finally, the frequency image

shows the contact resonance frequency shift at different locations and can be eventually related to the relative stiffness of the sample surface. Different constituents in nacre and their responses to electric field can be differentiated from the corresponding contrast together with the physical meanings of these four types of images.

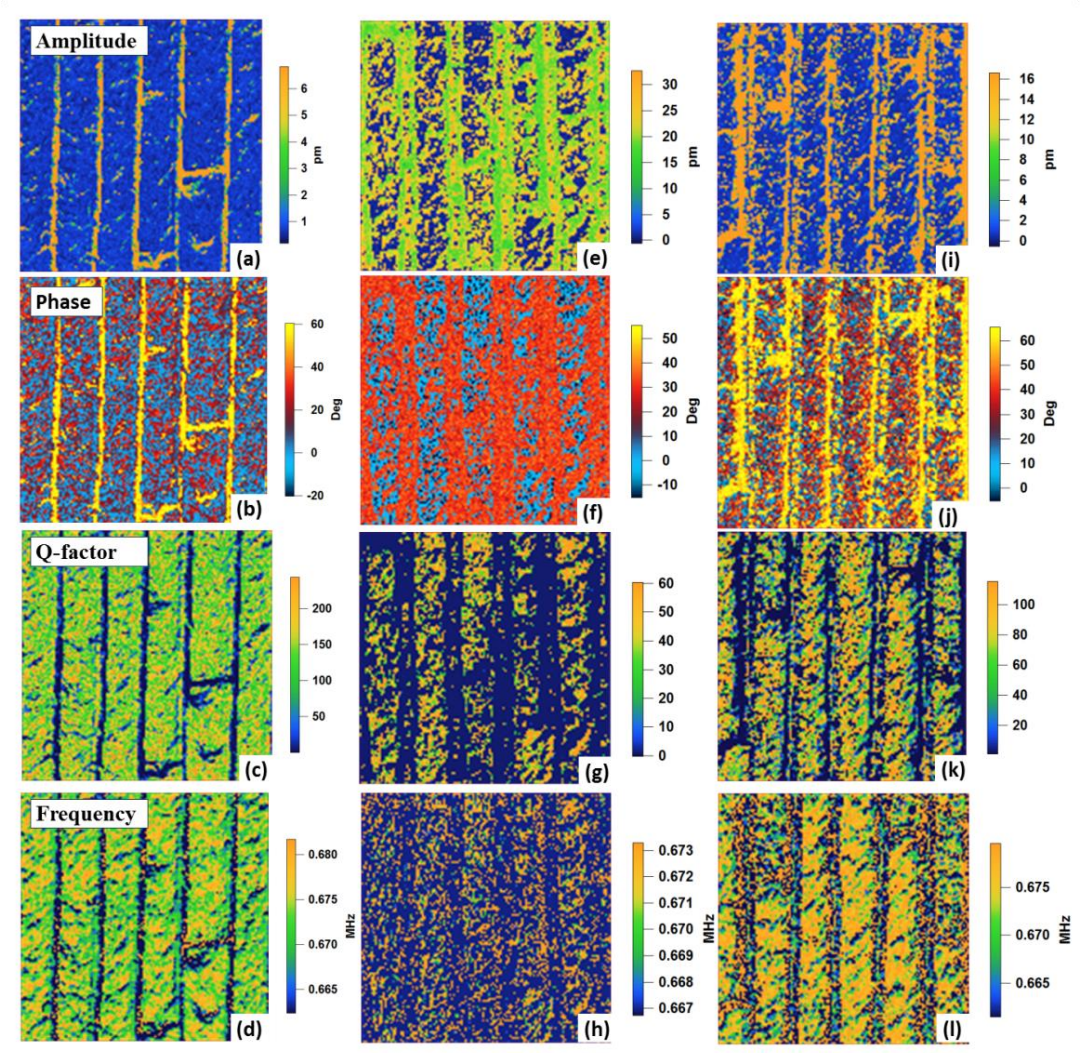

Fig. 7.2 BE-PFM images of the cross-sectional surface in nacre of the abalone shell. All of the images have 128×128 data points within 2×2 μm^2 scanning area. The 1st column, 2nd column and 3rd column images illustrate the piezoelectric response under stress-free state, tensile stress and compressive stress respectively. Amplitude images: (a), (e), and (i); Phase images: (b), (f), and (j); Q-factor images: (c), (g), and (k); and Frequency images (d), (h), and (l).

Under the stress-free state, i.e., before applying any bending stress, the entire cross-sectional nacre surface exhibits the similar contrast in piezoresponse image. The representative set of images scanned at the outer shell region is shown in Figs. 7.2(a)-(d). As discussed before, aragonite should not have any piezoresponse due to its centrosymmetric crystal structure. On the other hand, most biopolymers, belonging to the classes of polysaccharides, proteins, and nucleic acids, have been found to exhibit the piezoelectric effect (Fukada, 1995). The organic phases in mollusk shell are mainly chitin and various proteins that are rich in Asp, Ala and Gly of amino acid residues (Marin and Luquet, 2004; Bezares, Asaro and Hawley, 2010). Most of these amino acids in biopolymers have been found to exhibit piezoelectricity (Ando, Fukada and Glimcher, 1977; Lemanov, Popov and Pankova, 2002). Their polarizations are originated from the internal dipole rotations (e.g. CO-NH) induced by shear or tensile stress that delivered to the biopolymer molecules. In the Fig. 7.2(a), the yellow-color regions show the highest amplitude value (~23 pm). It is therefore believed that the yellow thin layers represent the interlamellar biopolymers, which is located between the mineral layers. It should be noted that most of the literature reported values for piezoelectric constant of biopolymers were d_{14} (i.e., under the shear stress) at the macroscale (Fukada, 1995), and it is much lower than the local effective d_{zz} value at nanoscale that obtained from this study. On the other hand, the mineral layers should be associated with the blue color regions, whose piezoresponse is weak (~0.7 pm). This weak response may originate from the intercalated biopolymers/macromolecules in the aragonite structure during the bio-mineralization process. The thickness of the yellow and blue colored

layers is about 20~40 nm and 0.3~0.4 μm respectively, which also confirms the above findings. Furthermore, there are some random green-yellow spots inside the mineral layers (blue color) with the intermediate response amplitude (1~5 pm). These spots can be either the intracrystalline matrix where the mineral nanograins are embedded in, or the interlamellar biopolymers that displaced due to the polishing stress. In the phase image [Fig. 7.2(b)], three distinct colors can also be identified. The interlamellar biopolymer shows a phase angle of ~57 º(bright yellow color). Inside the mineral layers, the blue color phase is ~0 ºand the red color phase is around 20 °. Compared to the amplitude image, 0 ºcorresponds with the weakest piezoresponse regions, which is the mineral phase. However, both the intracrystalline biopolymer and part of the mineral phase have phase angle around 20 °. In addition, Q-factor measures the dissipative response of the tip-sample interaction or the work done on sample by the oscillating probe. The lower the value, the more the energy is dissipated. In Fig. 7.2(c), the interlamellar biopolymers show the lowest value of Q (blue color). This indicates that the soft biopolymers can absorb much more energy than that of the hard $CaCO_3$ mineral when interact with the conductive tip during the BE-PFM scanning. The Q-factor image has the opposite contrast to the amplitude image. The difference in the Q-factor values between the mineral and biopolymers suggests that these two microconstituents have different EM coupling mechanisms. Lastly, in Fig. 7.2(d) the frequency image is an indicator of the relative stiffness of the scanned area. Regions with lower contact resonance frequency (blue-color) are less stiff than those with higher contact resonance frequency (yellow-color). Thus, the interlamellar biopolymer regions are less stiff than that of the

mineral layers, which reflects the correct correlation of the nanostructure of the abalone shell. Regions with intermediate value (green-color) should be associated with the intracrystalline biopolymers. But with the intimated bonded nanograins that immediately at the subsurface of the intracrystalline biopolymer matrix, the observed stiffness could be higher than that of the pure isolated intracrystalline biopolymers in these regions. In general, the piezoresponse with higher amplitude, lower Q-factor and lower contact resonance frequency corresponds to the regions of biopolymers in nacre, either interlamellar or intracrystalline, while the contrary applies to the mineral phase. These results are consistent with what reported in Chapter 5.

Figs. 7.2(e)-(h) show the piezoresponse of nacre under tensile stress (outer shell region). The responses in the sample surface are dramatically changed compared to those under the stress-free state [Figs. 7.2(a)-(d)]. In Fig. 7.2(e), the overall strength of piezoresponse is significantly increased. The interlamellar biopolymer still has the highest amplitude value, which is now larger than 25 pm (yellow-color), while the mineral phase has the lowest amplitude value of ~ 1 pm (blue-color). In addition, green-color regions with amplitude of around 20 pm can be found. Because of such high piezoresponse amplitude, these regions should also have highly-concentrated biopolymers. The area of biopolymers is increased by about 60% compared to that in the stress-free state, and this leads to the enhanced average piezoresponse strength. When tensile stress is applied, polymer molecules and chains are stretched, which can cause the rotation or displacement of bonded nanograins. The nanograins may sink into the intracrystalline biopolymer matrix and lead to more biopolymers appear on the sample surface. This can also be verified

by the features in Fig. 7.1. In the Fig. 7.2(f), two distinct phase contrasts can be identified: the phase in 30 º(red-color) corresponds to the biopolymers and the phase in 0 º(blue-color) corresponds to the mineral. Compared to that of the stress-free state, the phase angles of biopolymers are shifted from 57 º (interlamellar) and 20 º(intracrystalline) to around 32 º. This shift of the phase angle of biopolymers suggests the dipole rotations caused by the tensile stress. In the Q-factor image [Fig. 7.2(g)], biopolymers still have lower value than that of the mineral phase. The overall value is lower than that of the stress-free state, which indicates the tip-sample energy dissipation becomes higher for the nacre under tensile stress, in other words, biopolymer dissipates more energy under tensile stress. In Fig. 7.2(h), biopolymers still show lower stiffness than that of the mineral phase. But the clear boundaries between the mineral and organic phase layers are almost disappeared. The image can be interpreted as the stiffer particles randomly embedded in the less stiff organic matrix. Apparently, the tensile stress along the layers direction has the effects to expose more biopolymers on sample surface and increase the strength of piezoresponse. Therefore the relative position of constituents is changed and the properties of individual constituent, especially the biopolymers, have been changed as well. Generally-speaking, the interlamellar biopolymer in nacre is proposed as sheets of β-chitin fibrils. There may be silk/fibroin-like Asp-rich glycoproteins (polar acidic) adsorbed on the surface of the β-chitin sheets and act as the joining media to the aragonite crystals (Lin and Meyers, 2005). However no isolated silk-like protein has been characterized from nacreous shells. So their existence and properties are still questionable. There are also proteins located between side walls of platelets in the same mineral layer

called intertabular matrix (Heinemann et al., 2011). In our study, the tensile stress is parallel to the interlamellar biopolymer layers, and it leads to the stretch of the β-chitin sheet and probably breaks some of the fibrils as well. Both the amplitude and phase images suggest that the number of open pores along the interlamellar layers are slightly increased under the tensile stress (blue dots indicate the exposure of mineral phase). The amplitudes of both interlamellar and intracrystalline biopolymers are also increased under the tensile stress. As the strength of piezoresponse is proportional to the crystallinity and orientation of the macromolecules (Ando, Fukada and Glimcher, 1977), the tensile stress may therefore cause the increase in crystallinity, or change the molecule orientation; and the fibrous configuration of chitin in nacre may also manifest the shear piezoelectric effect (Fukada, 2000; Pereira-Mouries et al., 2002; Bezares, Asaro and Hawley, 2010). In addition, the tensile stress may cause the rotation of the CO-NH dipoles in the acidic acid that also can contribute to the increased piezoresponse of the biopolymers.

Furthermore, Figs. 7.2(i)-(l) show the piezoresponse of nacre under compressive stress. Similar to the case of under tensile stress, compressive stress also leads to the rearrangement of the micro-constituents in nacre. Under compression, the interlamellar biopolymers have amplitude of 21 pm, and phase in ~60 °. The mineral phase has amplitude of 0.6 pm, and phase of ~0 °. There are also small amount of intracrystalline biopolymers with 2~6 pm amplitude and ~40 ° phase angle. Once the pool of intracrystalline biopolymer in mineral layer is compressed, the nanograins can be either lifted up to the surface or hidden into the intracrystalline biopolymers. Furthermore, the

nanograins composed the bulging layers can be rotated and aligned in the direction which occupies the minimum space, this may cause the displacement of the interlamellar biopolymers and makes them appearing wider and distorted. From Figs. 7.2(k) and (l), it seems that the stiff nanograins in the mineral layers are packed more closely along a preferred orientation. Different from the cases of the stress-free as well as under the tensile stress, the stiffness of mineral layer appears more uniform under the compressive stress, which promote the idea that most nanograins are lifted up and squeezed together under the compression.

Table 7.1 Statistical summary of the EM coupling properties of individual component in nacre under different stress states. The percentage of data points with piezoresponse amplitude larger than 10 pm is also listed in the fourth column.

	Amplitude (pm)				***Phase (°)***		
	Inter-polymer	**Intra-polymer**	**mineral**	**≥ 10**	**Inter-polymer**	**Intra-polymer**	**mineral**
Stress Free	**23**	**1-5**	**0.7**	**9.58 %**	**57**	**20**	**0**
Tension	**>25**	**20**	**1.0**	**71.75 %**	**32**	**32**	**0**
Compression	**21**	**2-6**	**0.6**	**36.50 %**	**60**	**40**	**0**

For the purpose of easy comparison, Table 7.1 summarizes the values of the piezoresponse amplitude and phase angle of the individual constituent in nacre under different stress states. Generally-speaking, the biopolymers always have much stronger piezoresponse than that of the mineral phase. Tensile stress has caused more biopolymers to be exposed onto the sample surface and greatly increase the strength of the piezoresponse of the entire scanned surface, while compressive stress tends to push the nanograins onto the surface. Furthermore, the local amplitude may also include the coupled piezoresponse from both lateral and vertical directions, whereas this study

only presents the results from the vertical direction and the exact crystal orientations of the nacre layers are not identified. Table 7.1 also summarizes the amount of strong piezoresponse regions (defined as amplitude > 10 pm in this work) by the percentage of the data points from the amplitude images (128×128 points). These values indicate the relative amount of biopolymers exposed on sample surface under different stress states. Moreover, the histogram graphs presented in Figs. 7.3(a) and (b) represent the full data range from the images in Fig. 7.2. The vertical axis represents the number of data points and the horizontal axis represents the data scale. These two graphs provide more intuitive view of the changes in the piezoresponse triggered by the external stress.

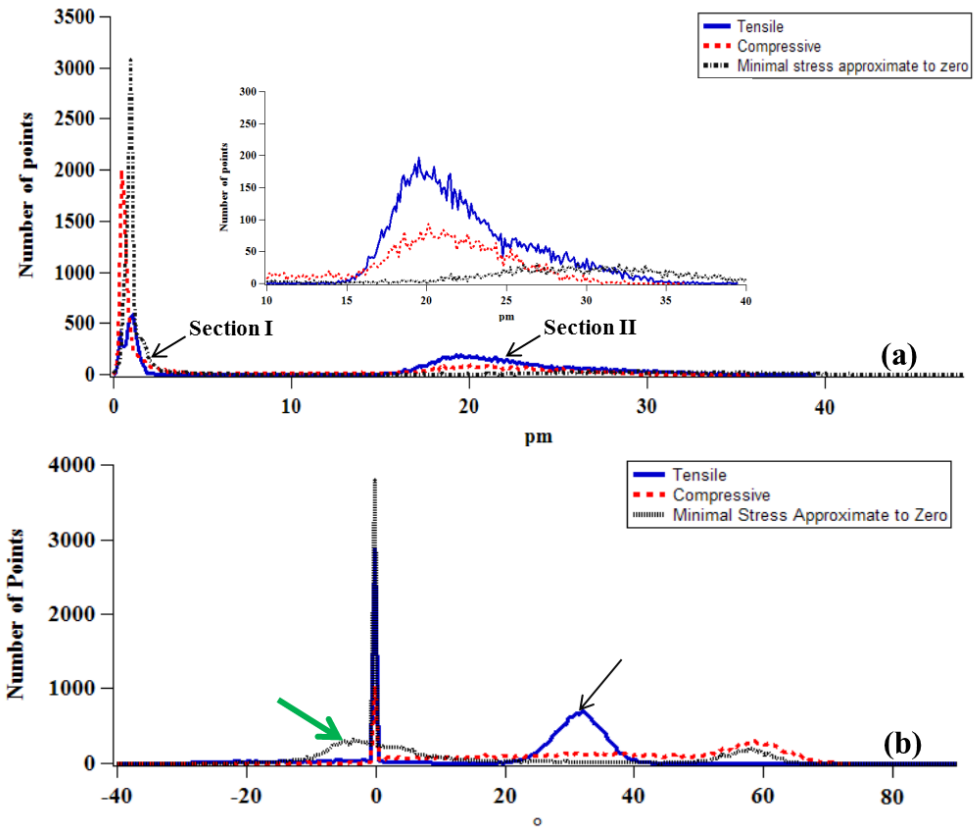

Fig. 7.3 Histogram illustration of BE-PFM images under different stress states. (a) Amplitude distribution. The insertion is the magnified region

between 10~40 pm with the vertical scale set to 0~300, (b) Phase distribution. (The arrows are discussed in the text).

Two sections are shown in the amplitude histogram [Fig. 7.3(a)]. When stress is applied, regardless of tension or compression, the amount of lower amplitude section (I) is reduced and the number of data points with higher amplitude section (II) is increased. As the phase data directly represent the phase lag/lead relative to the drive signal, they reveal the domain patterns based on the difference in the polarization directions. However, without the knowledge of the exact crystal orientation, only the relative phase difference in an image can be quantified. The mineral phase is found always have the phase angle close to 0 º, indicating that the domains are pointing vertically downwards and their directions are not affected by the stress. On the other hand, the domains with the phase angle differ from 0 ºat the stress-free state are shifted after the application of the tensile stress, as indicated by a thick arrow in Fig. 7.3(b). Taking the mineral phase as a reference (0 º), the tensile stress causes the most significant change of the phase angle by more than 20 º. The newly emerged domain/polarization under tensile stress is indicated by a thin arrow. As the CH_3 and NH_3 groups in amino acid crystals may hinder the rotations of the molecular groups (Lemanov and Sochava, 2003), they may confine the rotation of dipoles only to a certain angle. In such case, the external tensile stress alters the original dipole moments within the biopolymers to another preferable stable state. On the other hand, the compressive stress seems do not have very significant effect on the dipole rotation.

In short, the BE-PFM method clearly differentiates the mineral phase, interlamellar biopolymer, and intracrystalline biopolymer at the nanoscale based on their distinct interactions with the applied electric field under different stress states. The relative surface stiffness and energy loss from tip-sample interaction can also be revealed. From these images, the deformation mechanisms of the nacre under tension and compression can be revealed. Moreover, nacre has again been approved with piezoelectric property, which is originated from various types of biopolymers. This intrinsic property can make the biopolymers as the "sensor" or even "actuator" to control the bio-mineralization process and to make the proper response to the external stresses.

7.1.3 Ferroelectric Hysteresis Behaviors Responding to External Stress

In this study, ferroelectric hysteresis mappings of the cross-sectional nacre were observed by using SS-PFM technique (sample mappings are illustrated in Appendix-C). These maps (10×10 points within 3×3 μm^2 area) are acquired from three different regions: maximum tension, maximum compression, and near the neutral axis. All of the maps are acquired with exactly the same tip, laser position, and parameter settings.

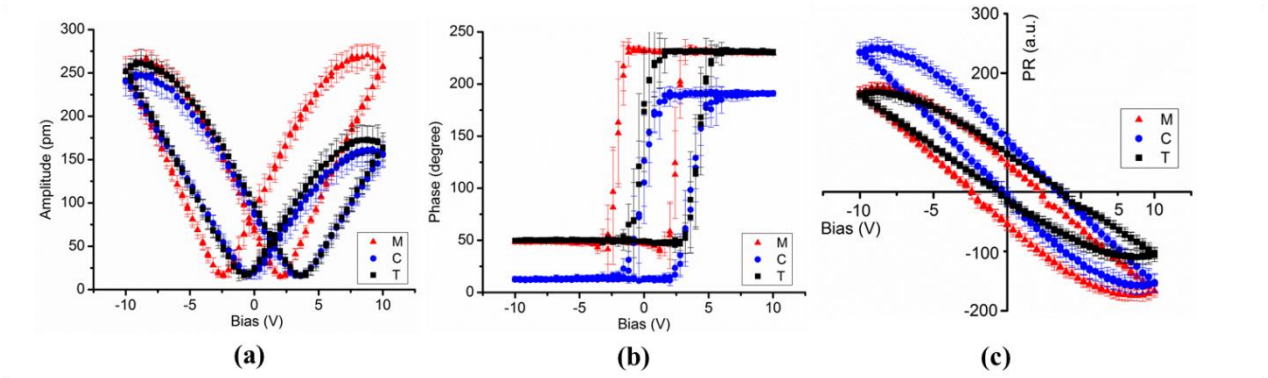

Fig. 7.4 Ferroelectric hysteresis loops of cross-sectional nacre under different stress states. (a) Amplitude hysteresis loops, (b) Phase offset hysteresis loops, and (c) PR hysteresis loops. The annotations "C", "T", and "M" indicate compression, tension, and zero-stress positions respectively.

In Fig. 7.4, each loop is plotted based on the average values of ten representative data points at the same region. The applied local poling bias window is ±10 V_{dc}, and the bias for piezoresponse detection is 4 V_{ac}. The amplitude loops in Fig. 7.4(a) have the butterfly shape as those from many typical ferroelectric materials. Under zero-stress state (indicated by M), the amplitude loop is symmetric about the zero-bias axis, and the maximum bias-induced deformation can reach to approximately 270 pm. Under the stressed states (where tension is indicated by T and compression is indicated by C), the amplitude loops become highly non-symmetrical and shift along the bias-axis towards the positive direction. The maximum deformation under positive bias is significantly reduced by about 36%. In addition, the maximum deformation at the tensile region is slightly larger than that at the compressive region. Thus, the compressive stress may reorientate the biopolymers to a direction that cannot be deformed as much as that under the tensile stress. Fig. 7.4(b) shows the polarization direction switching as a function of DC bias swept. The switched phase angles between two stable/saturated states at high V_{dc} are all about 180 °, which indicated the saturation of the response. In the previous

chapters, it has been shown that only the biopolymers exposed on sample surface can have such ferroelectric hysteresis loops, which is also reported earlier (Li and Zeng, 2012). Clearly, the loop under compressive stress shows different stable polarization directions from the other two, and this indicates the different stable dipole orientations under the compressive stress. Based on the amplitude and phase hysteresis loops, the biopolymers under compression and tension clearly show different molecular orientation or deformation characteristics.

Table 7.2 Mean values of the characteristic parameters extracted from PR loops at zero-stress, tensile, and compressive regions based on the one hundred data points in SS-PFM maps (C, M, and T refer to Fig. 7.4).

	Vertical shift (a.u.)	***Imprint (V)***	***Coercive bias (V^+)***	***Coercive bias (V^-)***	***Maximum switchable PR(a.u.)***	***Work of switching(a.u.)***
C	**30.5**	**1.41**	**3.56**	**0.78**	**403**	**1416**
M	**-8.5**	**-0.3**	**1.62**	**-2.43**	**345**	**1497**
T	**15**	**1.23**	**3.38**	**-0.55**	**266**	**1112**

Fig. 7.4(c) illustrates the calculated PR loops. The characteristic parameters extracted from these loops were summarized in Table 7.2, including: coercive bias, imprint, maximum switchable piezoresponse, shift along the PR-axis (vertical shift), and work of switching. These values are showed as the mean values from one hundred data points at each region. Compared to those from the zero-stress PR loop, the imprint and shift along the vertical-axis are dramatically increased for PR loops under the stressed states. The shift of ferroelectric hysteresis loop along the bias axis (indicated by imprint) manifests the existence of the internal bias fields inside the samples. It was reported that this shift should be mainly due to the perfect

alignment of defects, i.e., the local defect dipoles are all along the similar orientation (Damjanovic, 1998). The PR loops observed under tensile and compressive states have almost the same imprint value, which indicate the similar value of aligned internal field. The biopolymer molecules are found to have the modular structure which can be analogous to the coiled-spring structure (Xu and Li, 2011). Under the tensile stress, the biopolymers/macromolecules are stretched and the modular domains can be unfolded and aligned in the same manner. In other words, the stretched biopolymers may have their dipoles aligned almost in the same directions and hence cause the local uniform internal fields. Under compressive state, some of the biopolymer domains may also realigned the local dipoles in certain orientation, which is not necessarily similar to that under tension. Despite of this shift along bias-axis, the coercive fields of the PR loops under the stress states are similar. On the other hand, the vertical shift of the PR loops is related to the relative thickness of non-switchable layer in the materials (Alexe et al., 2001; Kalinin et al., 2010; Rodriguez et al., 2010). Under the stressed states, some of the biopolymer domains may be either stretched or compressed to extreme, which do not allow further dipole rotations or require much higher energy to rotate the local dipoles. Besides, the PR loop under compressive state shifts up more on the vertical axis than that under the tensile state. Under compression, the nanograins should be packed more closely, which may also contribute to the local non-switchable component.

Furthermore, the work of switching indicates the energy consumed or lost during polarization switching and pinning strength, it is calculated from the area enclosed by the PR loop (Kholkin et al., 2007). The zero-stress loop

has the highest value of work of switching, and the loop obtained under tensile stress has the lowest value. Thus, less energy (reduced by about one quarter) is required to complete the switching process when the material is subjected to the tensile stress. In other words, the tensile stress has consumed certain energy of the initial PR loop under stress-free state. This process may be associated with the mechanism called "domain switch toughening" operated in some ferroelectric ceramics (Schneider, 2007), i.e., the poled ferroelectric ceramics showed increased fracture toughness under the electric field. Furthermore, it has been reported that the critical energy release rate in the electrical way could be more than ten times faster than that in the mechanical way (Zhang, Zhao and Liu, 2004). Therefore, the nacre's ability to switch the local polarizations between the stable states with or without applied stress can help to relieve the imposed mechanical stress or energy to certain extent. When external stress is applied, local electric fields can be generated due to the piezoelectric properties of nacre. The induced electric fields can further switch the polarizations of the nacre within their range. If crack is generated in the first place, there will be a generated electric field surrounding the crack tip based on the local stress conditions, and this may prevent the crack propagation or even close the crack gradually. To certain extent, this result confirms our previous assumption, i.e., the piezoelectric toughening in mollusk shell, therefore, we believe that the piezoelectric and ferroelectric properties of nacre may play some roles in the toughening behavior of the nacre. In addition, the shape of the hysteresis loop of nacre under all three stress conditions resembles to those macroscopic P-E loops observed from the synthetic polymers which usually show great energy storage and fast discharge

ability (Chu et al., 2006; Zhang and Chung, 2007). This also suggests the possibility that the biopolymers in nacre can store the external energy and then release it in some way. However, this proposed mechanism still needs more theoretical and experimental works to further confirm it or to understand to what extent the piezoelectric/ferroelectric behavior of the biopolymers can contribute to the toughening and strengthening of the nacre.

7.1.4 Summary

In this study, it has been shown that the tensile stress leads to the sinking of nanograins into intracrystalline biopolymers, while compressive stress tends to push the nanograins onto the surface. This can change the amount of biopolymers exposed on the sample surface and eventually affect the detectable piezoresponse at the cross-sectional surface of the nacre. The change of the biopolymers structure can be tracked by the phase data in the BE-PFM analysis. The tensile stress has emerged new domains which may be due to the restricted rotation of amino acid dipoles. Finally, the saturated ferroelectric hysteresis loops have been studied. They further indicate the deformation or rotation of the biopolymers in the nacre structure under stresses. The energy associated with the ferroelectric loops under different stresses is presented as well. The results have confirmed, at least to certain extent, the possible “domain switch toughening” in the mollusk shell structures.

7.2 Responses of Mollusk Shells to Temperature Changes

Besides piezoelectric and ferroelectric, ionic motion or streaming potential is another source of EM coupling in the biological materials. Based on the studies of bone (Ahn and Grodzinsky, 2009), which is a more complex calcified tissue than mollusk shell, the strain-generated potential was attributed to two main mechanisms: piezoelectricity and streaming potential (Fukada and Yasuda, 1957; Shamos, Shamos and Lavine, 1963; Lang, 2000). In particular, for the tissues with a high degree of hydration (such as wet bone), streaming potential, in which was raised from the small channels or micropores that filled with charged fluid, was believed to be the predominant origin of the electromechanical behavior other than the piezoelectricity. With mechanical deformation, the fluids are forced to flow through the microvoids and thus generate a flow of ions against the oppositely charged walls, resulting in a potential difference between two points along the stream (Hastings and Mahmud, 1988).

In order to understand the functionality of moisture and degradation of the organic phase in the EM coupling effects in mollusk shells, it is necessary to study the piezoresponse of mollusk shells that have been treated at different temperatures. The results will be presented and discussed in the following sections.

7.2.1 Response of Abalone Shell

TGA and DTA are firstly conducted to identify the decomposed temperature for moisture and biopolymers in abalone shell (Fig. 7.5).

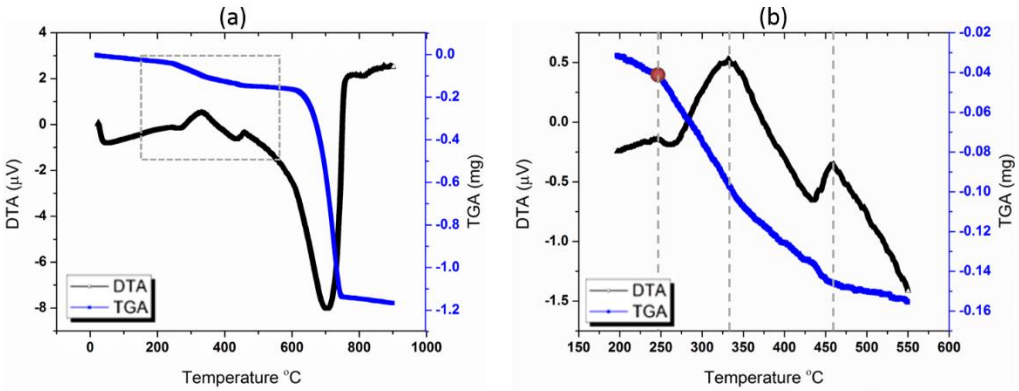

Fig. 7.5 TGA and DTA curves of abalone shell fragment (air atmosphere; room temperature to 900 ℃; heating rate = 10 ℃/min). (a) curves in the full temperature range, and (b) curves representing major biopolymers decomposition from 150~550 ℃.

Fig. 7.5(a) shows the full range TGA curve of the abalone shell. The water content was found less than 1 wt.% presumably to be completely evaporated in the range of 100~105 ℃. According to the study of bovine bone and decalcified bone, the critical hydration that causes significant effects to dielectric constant and piezoelectricity is at least 4 wt.% (Maeda and Fukada, 1982). Thus, it provides the first clue that the moisture content may not have significant effects on piezoresponse in abalone shell. In addition, void space in fresh abalone shell should be much smaller than those in bone, hence, the piezoresponse should play a more critical role than the effect of the ionic-fluid-based streaming potential.

When further increasing the temperature, the great mass drop at about 700 ℃ is found, and this is due to the decomposition of $CaCO_3$. Furthermore, the major decomposition of biopolymers starts at about 200 ℃ and ends at about 600 ℃. It was reported that the biogenic aragonite releasing of CO_2 started at 70 ℃ and reached to the maximum just above 250 ℃ (Pokroy et al., 2006), and our result is consistent with Pokroy's finding [Fig. 7.5(b)]. The red dot indicates the temperature for an abrupt change in slope of the TGA curve.

The decomposition rate reaches to the maximum at about 250 ℃, and gradually slows down until all of the biopolymers are decomposed. Because decomposition may start much earlier, the moisture content may be even lower than the previous predicted value. It was reported that the biological aragonite has a structure distorted by the organic phase. This structure distortion is greatly reduced at elevated temperature, and at 300 ℃ the unit cell of biogenic aragonite reverts to that of geological aragonite (Pokroy et al., 2006). In our study, based on the finding from TGA and DTA curves, the unpolished shell was firstly heated to 105 ℃ to remove moisture and then to 380 ℃ to remove certain amount of the biopolymers. The PFM imaging was then conducted on the unpolished shell samples at room temperature after each heat treatment at these temperatures. Because of the high temperature treatment, shell sample casted in epoxy resin is not suitable for this experiment, hence, only the inner surface (smooth enough for SPM observation) of unpolished abalone shell was studied.

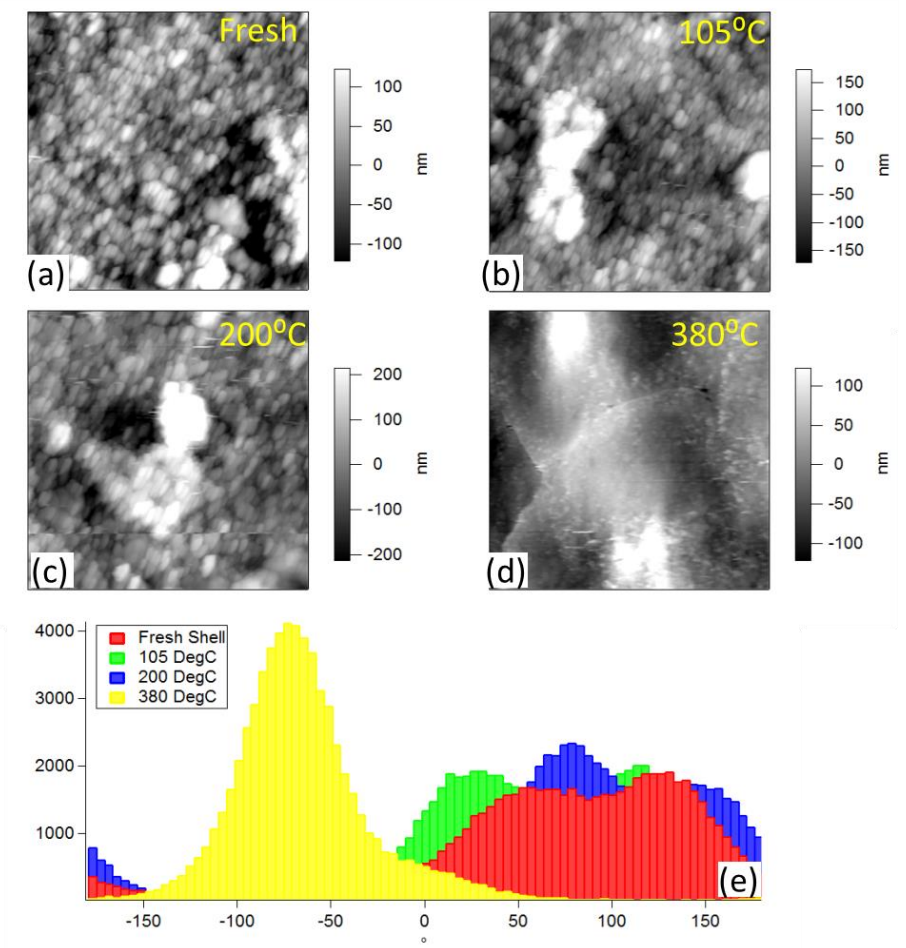

Fig. 7.6 PFM topographies of the inner surface of (a) fresh abalone shell, (b) after being heated at 105 ℃, (c) 200 ℃, and (d) 380 ℃, (e) PFM phase angles of shell with different heat treatments. Scan size is 10×10 μm for all images.

After being heated to 380 ℃, the shell became very brittle, peeled-off layers can be visually observed. This is mainly due to the decomposition of the interlamellar biopolymers between the aragonite platelets. In addition, the original oval nanoparticles can no longer be identified in the topography image after the sample was treated at 380 ℃ [Figs. 7.6(a)-(d)]. Without biopolymers, abalone shell can no longer be considered as a nanocomposite. The $CaCO_3$ crystals may recrystallize and grow, or have phase transformation at high temperature. Thus, nanograins disappear and only platelet patterns left. In the PFM studies, compared with that of the fresh shell sample, the observed

piezoresponse becomes stronger after that sample was being heated to 105 ℃. This is possibly due to the reduced water content. The abalone shell still exhibits piezoresponse even after the heat treatment at 380 ℃, which probably originates from the remaining intracrystalline biopolymers or those intercalated in the $CaCO_3$ crystalline structure. At this temperature, the ionic fluid-induced EM coupling can be eliminated. Thus, this reveals that piezoelectricity dominates the EM coupling effects other than ionic motion in mollusk shell structure. In addition, the histograms of polarization directions from different temperatures are illustrated in Fig. 7.6(e). For the shells treated below 380 ℃, there are always two peaks of phase angle, one corresponds to biopolymer and the other corresponds to mineral. However, after being heated at 380 ℃, the phase angle is significantly changed and there is only one peak left, which indicates that majority of the biopolymers is decomposed at this temperature.

7.2.2 Response of Clam Shell

The effects of temperature were also studied on the clam shell. Firstly, the TGA and DTA curves of the clam shell are obtained and shown in Fig. 7.7(a).

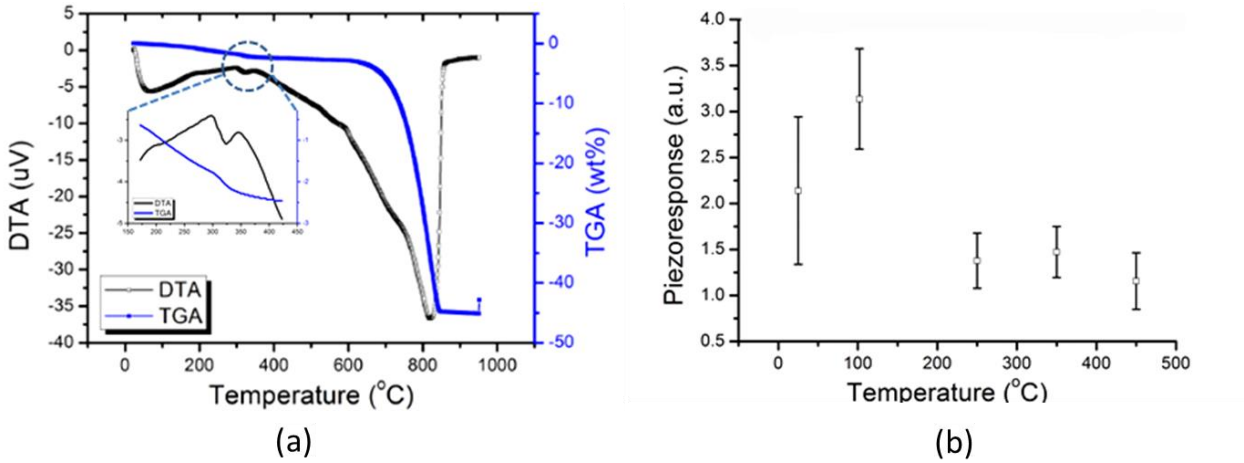

Fig. 7.7 Effects of temperature on piezoresponse of the innermost shell surface: (a) TGA and DTA curves of clamshell heated to 900 ℃, and (b) change of piezoelectric constant with temperatures.

The moisture content of fresh clam shell fragment is found about 0.29 wt. %. From the DTA curve, the major decomposition of biopolymers takes place at the temperature range of 300-350 ℃ and with peak maxima at 325 ℃ [insertion in Fig. 7.7(a)]. At this point, the original long-chain biopolymer molecules may be decomposed into low molecular products. After this temperature, the weight loss slows down with further increasing temperature, and till 550 ℃, the weight loss is ~2.49 wt. %. Excluding the water content, the mass fraction of organic phase in clam shell is slightly higher than the reported value in the literature (Fleischli et al., 2008). In our study, a small piece of clam shell fragment is studied by PFM after being treated at different temperatures. The changes of the effective piezoelectric constant of the innermost surface are plotted versus the temperatures in Fig. 7.7(b). After being heated at 102 ℃ for 72 hours, the piezoresponse increases substantially. The elimination of moisture at this stage reduces the effects from ionic motion or streaming potential and hence increases the detectable piezoresponse of the clam shell. However, when further increasing the temperature, the

piezoresponse is reduced significantly to a value which is lower than the original one. Weakening of the piezoresponse is probably due to the degradation of the biopolymer phase. However, this weakening process slows down at higher temperature. A weak piezoresponse still persists even at 450 ℃. It may be due to the intracrystalline biopolymers within the structures that are not fully decomposed at the high temperature. Therefore, the dramatic reduction of the piezoresponse should mainly due to the degradation of the biopolymers directly exposed on sample surface. This observations is very similar to that from abalone shell. On the other hand, the effects of moisture and the role of biopolymers on the ferroelectric behaviors of clam shell have already been presented in the previous chapter.

7.2.3 Summary

To summarize the effects of temperatures, it is found that the moisture has certain effects to screen out the piezoresponse from polarization. When moisture is eliminated, stronger piezoresponse is usually observed. If further increasing the temperature, the biopolymers are gradually decomposed, which leads to the reduction of the piezoresponse from the biopolymer. It further confirms the origin of piezoresponse in mollusk shell is biopolymers.

Generally speaking, the EM coupling in a biological system may have several contributing factors; in addition to piezoelectric coupling, electrocapillary phenomena and ionic motion mechanisms can also contribute to EM coupling effects. However, the latter two phenomena involve the existence of water molecules (Shahinpoor, 2003; Mirfakhrai, Madden and Baughman, 2007; Farinholt et al., 2008). Farinholt et al. (2008) has compared

the energy harvesting by piezoelectric and ionic conductive polymers, and it was found that the piezoelectric polymer, such as PVDF, was much better at energy harvesting, whereas ionic polymers favored to storing the energy produced. The current results on temperature effects show that the mollusk shell still has piezoelectric effects even after the water is removed from the structure, proving that the contribution of the water molecules does not significantly affect EM coupling. Therefore, it is anticipated that the piezoelectric effect is one of the main factors in the observed EM coupling phenomena, but, for the possibility of energy storage and release, ionic motion may play a role, and this will need further sophisticated studies.

Chapter 8

Bone Piezoelectricity, Self-healing of Mollusk Shell, and Future Perspectives

CHAPTER 8 Bone Piezoelectricity, Self-healing of Mollusk Shell, and Future Perspectives

The previous chapters have discussed the biopiezoelectric and bioferroelectric properties of mollusk shells in detail. This chapter firstly provides some preliminary results of piezoresponse of bone, followed by the damage healing phenomena observed from mollusk shell. Based on all of the findings from the entire research work, and from the related literatures, the implications and significances of the studies on biopiezoelectric and bioferroelectric behaviors of biological materials, from cell to tissue level, will be presented and discussed at the end of this chapter.

8.1 Electromechanical Coupling Behaviors of Bone

Similar to the mollusk shell, bone is another type of highly organized anisotropic hard tissue that serves as a reservoir for calcium and phosphate, a site for hematopoiesis and provides the structural support requited for movement (Isaacson and Bloebaum, 2010). Bone can be considered as a natural nanocomposite with a fibrous polymer framework and mineral nanoparticles (Peterlik et al., 2006). Bone is generally composed by 35% organic phase (over 90% is type I collagen) and 65% inorganic phase (primarily hydroxyapatite $Ca_5(PO_4)_3(OH)_2$, as well as three types of cells: osteocytes, osteoblasts and osteoclasts. Fig. 8.1 illustrates the 7-level hierarchical structures of bone, and the toughening mechanisms corresponds to each level of structure. This type of structure is critical for bone to provide mechanical support and movement flexibility.

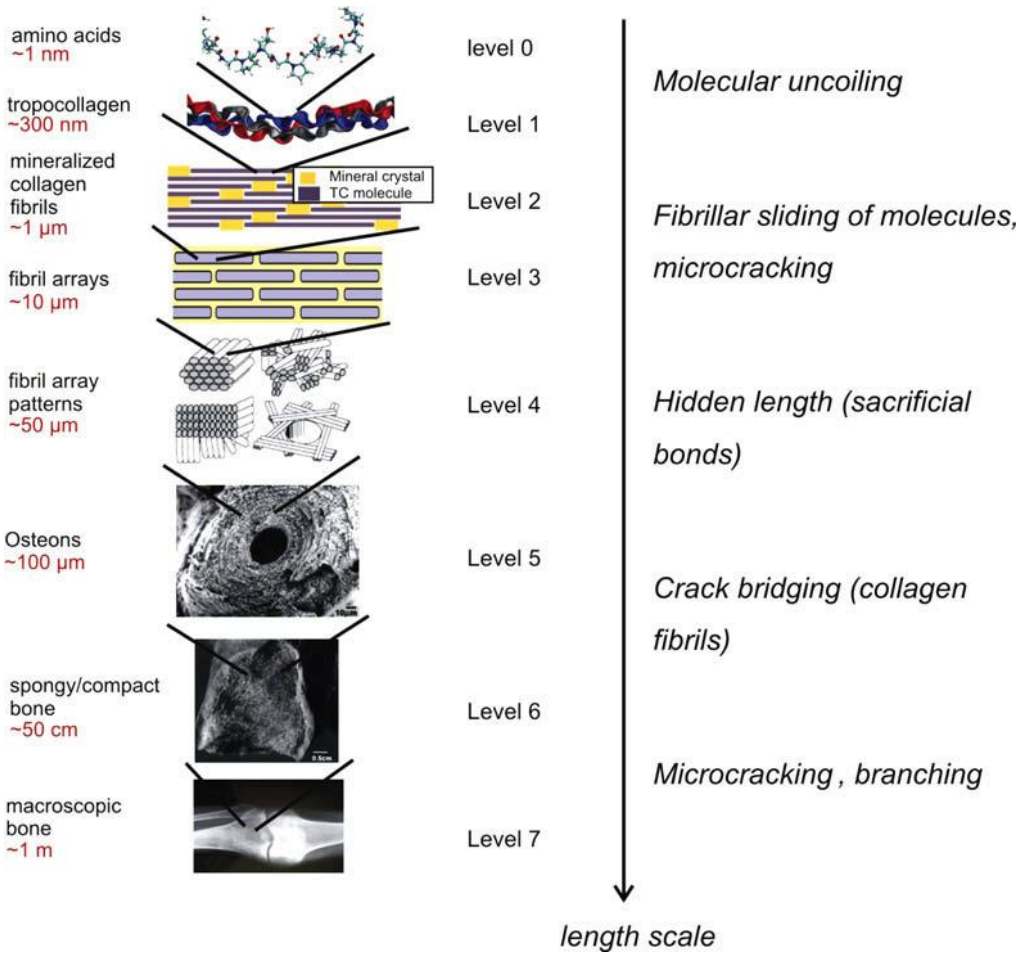

Fig. 8.1 7-level of hierarchical structure of bone (left panel), and the associated deformation and toughening (fracture resistance) mechanisms of each level. Reproduced from Espinosa et al. (2009).

On the other hand, bone has the intriguing ability of self-regeneration and self-remodeling. It can also alter its structure responsive to the external forces according to a well-established principle knows as "Wolff's law", explained as that when bone can be deposited and reinforced at areas of greatest stress (Frost, 2004). Therefore, astronauts returned from space have weaker bone, while weightlifters possess increased bone density (Ahn and Grodzinsky, 2009). But the critical question is how osteocytes (bone resorption cell) and osteoblasts (bone growth cell) sense the mechanical load. During these processes, piezoelectricity was proposed as one of the

indispensable factors (Isaacson and Bloebaum, 2010). It has been proven by clinical trials that electrical stimulation can facilitate bone healing (Griffin and Bayat, 2011). However, the details of healing mechanism is still not fully understood, especially that how the cells can sense the defects and move and proliferate proper amount to the right position. Naturally, piezoelectricity is considered as the potential trigger. Recently, the bone piezoelectricity has also been reported as a potential source of intense blast-induced electric fields in the brains, with magnitudes and timescales comparable to fields with known neurological effects (Lee et al., 2011). Therefore, more detail studies of the bone piezoelectricity is necessary in future. In this aspect, PFM is again an ideal tool to study this phenomenon in detail.

To evaluate whether the method developed to study mollusk shell also can also be applied to study the bone piezoelectricity, the nanoscale piezoelectricity of mechanically polished swine femur was characterized by DART-PFM (Fig. 8.2). Under such observing scale, level 1-3 hierarchical structures can be clearly observed in the height image. The smallest feature identified from the height images is the mineral nanograins. On the other hand, due to the specific nature of PFM technique, both amplitude and phase images can be used to help identify the biopolymer phases, including collagen. There is no direct correspondence between height and amplitude images, thus the topographic crosstalk is minimized. Under the smaller scanning size, collagen fibrils can be identified more clearly. Similar to the case in the mollusk shell, the strong piezoresponse should be originated from the polymer contents, which is clearly shown as white contrast in Fig. 8.2(e). The size of tropocollagen is about 300 nm, which is consistent with the PFM amplitude

image (white contrast pointed by a dark arrow) [Fig. 8.2(e)]. The long-chain collagen fibrils cannot always be observed. It depends on the bone orientation and sample preparation conditions. Collagens also have correspondence PFM phase contrast. The maximum polarization orientation difference is over 100 °. By knowing the crystallographic information of collagens, in-situ 3D mapping of piezoresponse and polarization of collagen molecules can be built from the PFM observation.

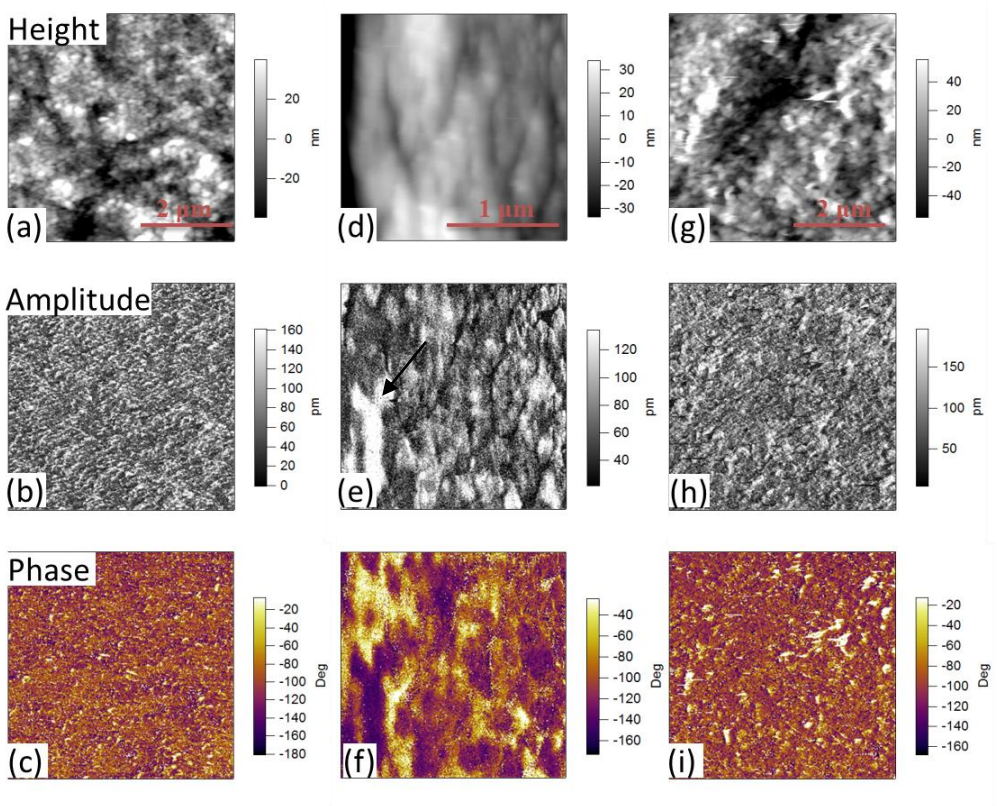

Fig. 8.2 DART-PFM raw images of fresh swine femur (4 V_{ac}). 1st and 2nd column images are obtained from the longitudinal surface, while the 3rd column images are obtained from the lateral cut surface.

The important role of bone is to provide support and protection. The piezoelectricity help bone structure to sense different loading force and trigger proper responses. But healthy bone and diseased bone may behave in different

ways in terms of piezoelectricity and elasticity. By examining the piezoelectric response of healthy and diseased bones under loading conditions, the role of piezoelectricity in bone remodeling may be clearly identified. Based on such observations, cures targeted to specific disease may be developed.

8.2 Self-healing phenomenon observed from Mollusk Shell

The damage healing of mollusk shells are mainly observed by optical microscopy. It is observed that the micro-morphologies of the defects and cracks generated by the microindentation change with time in various solutions. The key results and associated implications and limitations are presented in the following.

Several solutions are used for healing studies of the mollusk shells, including (1) DI water, (2) 3.5% NaCl, (3) Supersaturated $CaCO_3$, (4) 20mM $CaCl_2$, and (5) 0.5 mM Polyacrylic Acid (PAA) + 20 mM $CaCl_2$ (Kijima, Oaki and Imai, 2011). Defects were generated on the inner surface, outer surface and cross-sectional surface of the polished abalone shell by microindentation method as described in the Chapter 3. Besides of the indentation generated defects, the polishing processes may also induce other defects on the entire polished surface. Thus, the solutions caused shell surface morphology changes are not only near indentation, but also over the entire sample surface. One set of representative optical images of nacre surface is illustrated in Fig. 8.3. In the PAA + CaCl2 solution, the initial cross-shape of indentation impression gradually turned into circular shape and the size of impression was clearly increased in the lateral direction, which indicates the loss of materials. Cracks at the edges of “cross” were disappeared completely after 2 hours in the

solution. However, this change may be caused by the rapid dissolution of the micro-constituents in this solution.

The big challenge to observe the sample morphology change is the artifacts from optical measurements. The appearance of image can be greatly affected by focusing depth. In addition, although FE-SEM can provide much clearer image, gold sputtering is necessary for insulating materials like mollusk shells as they are essentially insulating materials. But with the thin gold coating, the healing of shell is prohibited. Moreover, due to the viscoelastic property of nacre, even large indentation force may not generate obvious cracks under optical microscope. Thus, the studies were focused on the shape change of the large scale indentation impressions.

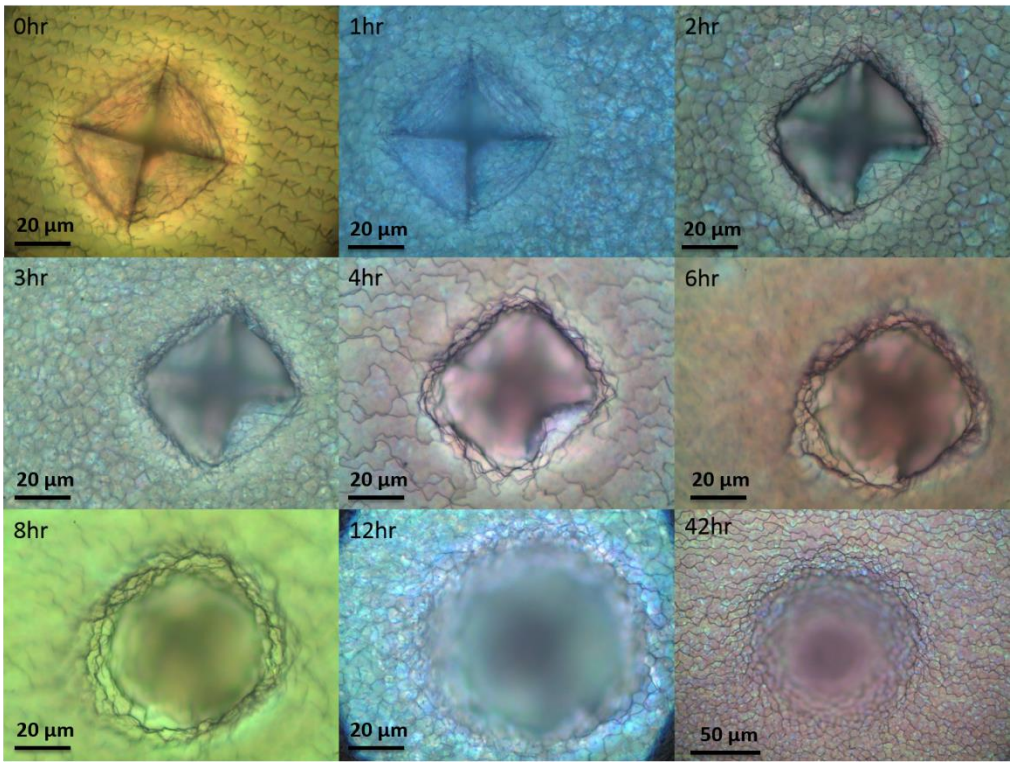

Fig. 8.3 Change of impression on nacre surface with time in PAA + $CaCl_2$ solution. All of the optical images are observed under the same scale (1000X magnification), except the one of 42 hr (500X magnification).

Moreover, the calcite section (the first shield to external attack) in abalone shell was also studied in the same way. Figs. 8.4, 8.5 and 8.6 illustrate the changes of indentations with time in DI water, NaCl solution and $CaCO_3$ solution respectively. After polishing, calcite crystals with different orientation are exposed on the sample surface. Height difference between differently oriented crystals is gradually increased with time when samples are placed in the solutions. This difference is caused by more rapid growth or dissolution of one type crystals. Unlike that in PAA + $CaCl_2$ solution, the lateral extent of impression is generally reduced in these three solutions, which may indicate the healing of defects. The morphology has more obvious changes when the samples are immersed in DI water and NaCl solution.

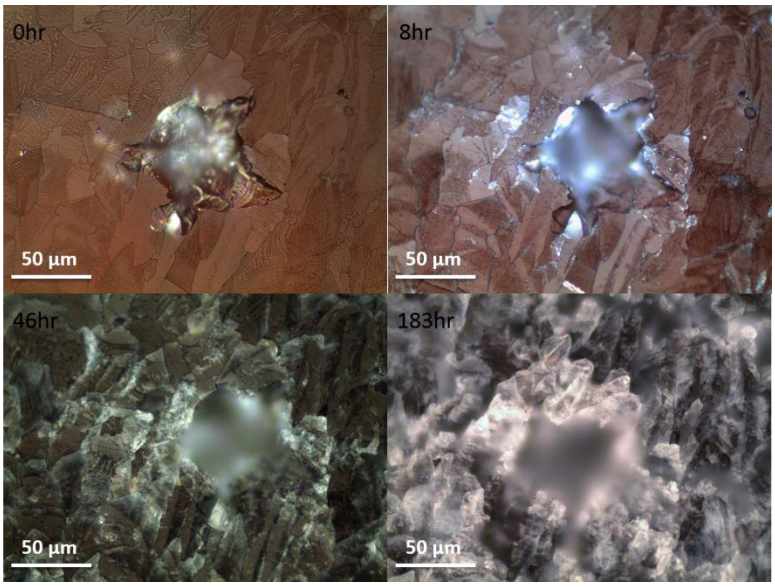

Fig. 8.4 Morphology change of calcite surface in DI water observed by optical microscope.

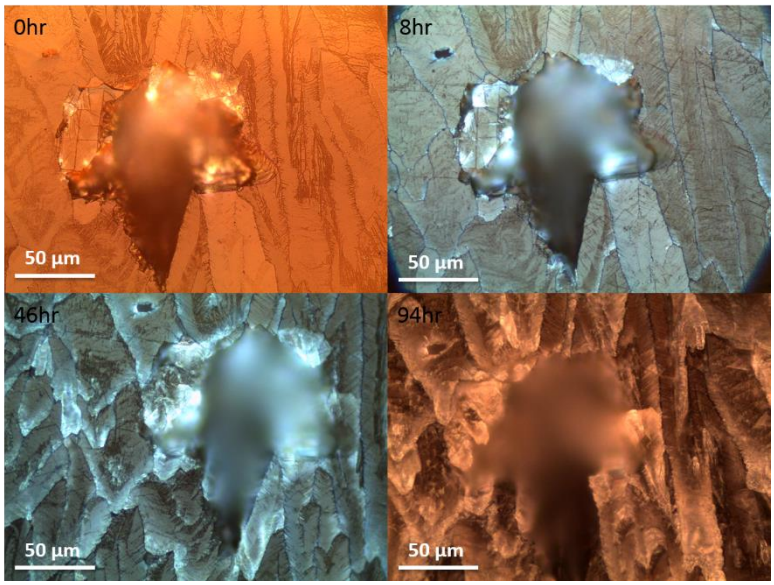

Fig. 8.5 Morphology change of calcite surface in NaCl solution observed by optical microscope. The indentation cannot be relocated in 183hr due to the severe morphology change.

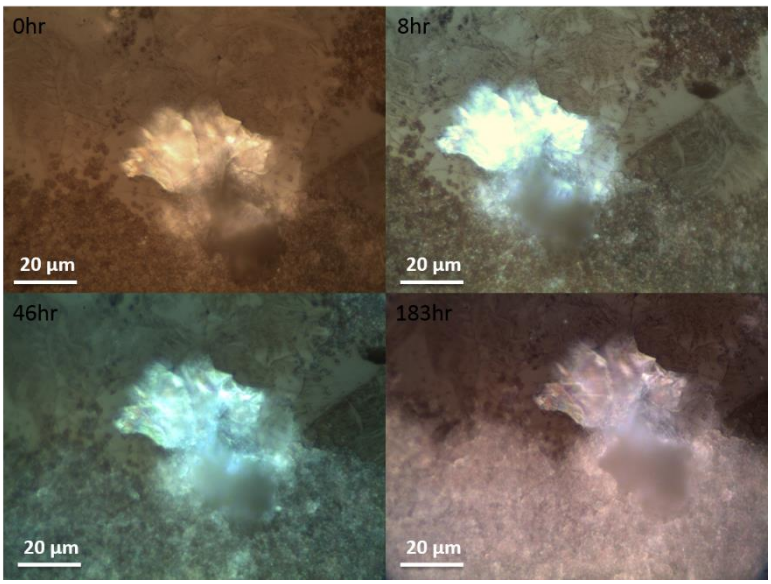

Fig. 8.6 Morphology change of calcite surface in $CaCO_3$ solution observed by optical microscope.

On the other hand, the changes of crack length were also monitored on clam shell in three different solutions: DI water, NaCl solution, and $CaCO_3$ solution. Optical images were obtained in the same way. Crack lengths were measured using the in-built software with the optical microscopy. The change

of crack length is recorded continuously within 7 hours after indentation (Fig. 8.7). Clam shell has more uniform structure and less biopolymer contents than those in the abalone shell. A lot of cracks can be generated near the indentation sites. Only two of the largest cracks were selected for measurement in order to have clearer optical image. Based on the graph, cracks healing rate is the fastest in NaCl Solution, and the slowest in the $CaCO_3$ solution. The underlining mechanisms of mollusk shell behaviors in variety of solutions require more studies in future. Moreover, it is found that both dissolution and crystal growth may contribute to the morphology changes in various solutions.

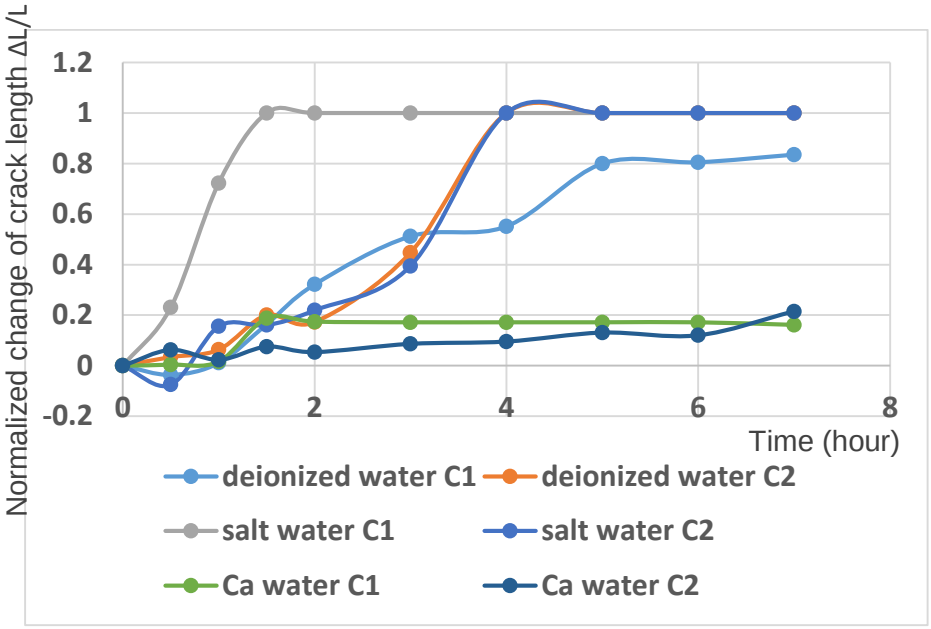

Fig. 8.7 Percentage change of crack length (ΔL/L) observed by optical microscope on the surface of clam shell. "0" indicates new crack; "1" indicates healed crack; "C" indicates crack.

8.3 Significances and Implications

The details of biopiezoelectric and bioferroelectric phenomena of the mollusk shells have been presented in the previous chapters. The preliminary

results for the bone and the healing phenomena of mollusk shells are briefly reported in this chapter.

In fact, not only hard tissue, soft tissue like heart muscles also exhibits EM coupling which may be critical for tissue functioning. Recently, the EM coupling of heart muscle has been studied and reported (Liu et al., 2012; Liu et al., 2013). However, there is still no explanation on the initiation and reason of such phenomena appeared in the soft tissues, and also how to relate these properties to the ordinary phenomena such as impaired contractility and arrhythmias in connection with heart failure (Stokke et al., 2012). Nevertheless, the biopiezoelectricity and bioferroelectricity again show their potential significances in biological systems.

The research of biopiezoelectricity and bioferroelectricity of biomaterials were firstly started in the 1950s. In most cases, these biomaterials were studied in the same way as for the traditional non-biological piezoelectric or ferroelectric materials. However, the biomaterials responses are far more complex, and one simple biological response usually involves mechanisms which cannot be explained in one scientific discipline. Therefore, due to the limitations of the characterization facilities and relatively scarce relevant information, no great breakthrough has ever been reported. Since the development of SPM techniques, such as PFM, more attentions were paid on the studies of natural biomaterials in this area. This topic is again gradually progressed in the past few years. The entire realm is still at its infant stage. Currently, several groups have been making great efforts on the research of biopiezoelectricity and bioferroelectricity of biomaterials for future potential applications.

Generally speaking, the study of the biopiezoelectricity and bioferroelectricity is an essential step to fully understand the underlining mechanisms of many mechanical and physiological behaviors in biological systems, ranging from macromolecules to complex tissue. This thesis mainly contributes to this aspect, and it is the essential step to make subsequent progresses. Thorough understanding is the foundation of arbitrary manipulation. A further step from the characterization is to utilize the observed properties to develop practical applications based on the comprehensive understandings of how these mechanisms work. These applications can be evolved in two directions. One is the biomedical applications, for instance, newly designed treatments according to the intrinsic piezoelectric and ferroelectric properties of biological tissues. The other is to develop new generation of materials, or biomimetic in the perspective of piezoelectric and ferroelectric behaviors of biomaterials, for instance, self-assembled flexible and environmental-friendly memory devices based on the ferroelectric properties in biomaterials. Therefore, the realm of biopiezoelectricity and bioferroelectricity phenomena have great potential and will blossom in the future.

Chapter 9

Conclusions and Recommendations

CHAPTER 9 Conclusions and Recommendations

Based on the results presented in the Chapters 4 to 8, overall conclusions of the entire research work can be made. Furthermore, the future works that may continue based upon the current research of the mollusk shells are also proposed in this chapter.

9.1 General Conclusions

The main objective of this thesis is to achieve basic understandings of the mechanisms and the importance of the biopiezoelectric and bioferroelectric properties in the mollusk shell. The thesis has presented the detail results on the nanoscale structural, mechanical and EM coupling behaviors of the mollusk shells (abalone and clam shell), in terms of piezoelectric and ferroelectric properties. The role of the EM coupling in mollusk shells and maybe other biological systems has been speculated and discussed. The key findings in this research work are summarized in the following.

❖ Nanoscale Elasticity and Energy Loss Mappings of the Abalone Shell

CR-FM technique provides the unique way to quantify the nanoscale elastic modulus and loss tangent of stiff and compliant materials. In this work, abalone shell has been characterized using this method. Both nacre and calcite show highly non-homogenous elasticity, elastic modulus continuously varied over the scanned surface. Under lower loading force, the elastic modulus near the sample surface is probed. Biopolymers can be easily identified as the low

stiffness regions in the images. Under higher loading force, stiffened nanograin boundaries can be observed. It may be due to the collective interactions of squeezed biopolymers and the surrounded nanograins, based on the characterization on the deproteinated abalone shell. In addition, the mean stiffness ranking in abalone shell is from the softest calcite-nacre transition region (CNTR) boundary to nacre and then to the stiffest calcite. The elastic modulus of nacre found by this method is similar to the values reported in the literature, but with great details of variations and distributions at the nanoscale that other methods cannot be achieved.

❖ Biopiezoelectric Properties of Mollusk Shells

In general, the piezoelectric property in the mollusk shells is originated from the biopolymer contents, including both interlamellar and intracrystalline biopolymers. However, some of the mineral nanograins also exhibit weak piezoresponse, and this may be due to the intercalated biopolymers inside the mineral crystals structure after biomineralization process. When part of the biopolymers is removed from the sample surface, piezoresponse of mollusk shells become weaker. The piezoresponse is also directional dependent so that different response is observed from different shell surfaces. The mean piezoelectric constant (d_{zz}) varies with shell species and shell ages. Clam shell exhibits relatively small d_{zz}, but it is still comparable to that of the x-cut quartz. The d_{zz} value for grown abalone shell is much higher, which is similar to as-grown γ-glycine microcrystals. Furthermore, the area shown piezoresponse is usually larger than the expected size of biopolymers. No sharp domain boundary can be observed. The property transitions between the

mineral and biopolymer phase are gradual and affect wider area than their boundaries. Piezoelectricity is naturally for sensing and actuating purpose. The observed piezoelectricity in mollusk shell, bone, teeth, and many other soft biomaterials may be responsible for detecting the local mechanical, chemical, and other properties changes via the biological electric pulse, and may also offer proper response. However, the electric current flow and cell response mechanisms are still mysterious and require further research.

❖ Bioferroelectric Properties of Mollusk Shells

Saturated ferroelectric hysteresis loops have been observed on different species of mollusk shell in various orientations under a relatively low DC bias window. Such response are attributed to the interlamellar and intracrystalline biopolymers. The coercive biases of the mollusk shells are found less than 5 V_{dc}, which makes it easier to switch the polarization. On the other hand, it is commonly to have non-symmetric hysteresis loops, with large imprint and vertical shift. These are usually believed to be due to the aligned and random internal fields. Biopolymers are complex long-chain molecules with local domains. Thus, the ferroelectric behavior may be originated from these permanent dipoles. When large DC electric field is applied, these dipoles may switch between the stable states and form the ferroelectric hysteresis loops. It is also found that the shapes of the loops observed from the mollusk shell are very similar to those of the synthetic polymers for energy storage applications, which are slim and tilted. Therefore, the biopolymers in the mollusk shell can store and release energy based on its ferroelectric property when external

mechanical stress is exerted. This may be another factor, which makes the biopolymers as an important reason for mollusk shell toughening.

❖ External Stress Effects on the EM Coupling of Nacre

Nacre is a type of nanocomposite material with viscoelastic properties. It is composed by nanograins embedded in biopolymer matrix. When nacre is subjected to tensile stress that parallels to the biopolymer layer, the whole section is stretched. In the cross-sectional surface, the biopolymer layers appear thinner, and the nanograins look smaller because they may sink into the intracrystalline biopolymer matrix. Conversely, when compressive stress is supplied, interlamellar biopolymer layers become wider and nanograins look larger as they may be pushed onto the surface. For both cases, the amount of biopolymers exposed on sample surface are increased, and this leads to the increase of the mean piezoresponse, especially under the tensile stress. In case of phase angle or polarization orientation, tensile stress causes the most significant changes, which is over 20 °. When biopolymers are subjected to tensile stress, the local polymer dipoles can be rotated and realigned to a stable state and form a different piezoelectric domain. On the other hand, compressive stress does not have this effect, which may be due to the restrained space or more resistance for polymer domains to be squeezed.

Furthermore, the ferroelectric hysteresis loops (piezoresponse vs. bias) of nacre under stress-free state is nearly symmetric about the origin. However, under stressed state, the loops are shifted along both piezoresponse and bias axes. This phenomena indicates that the local conformation of biopolymer molecules may be changed, which leads to aligned defects dipoles as well as

random electric field. Besides the shifts, PR loop also provides information of work of switching. The hysteresis loop observed from tensile-stressed nacre has the lowest work of switching, which suggests lower energy is required to complete the switching process. Lastly, the minimum deformation/amplitude achieved by nacre is constrained by the supplied stress compared to the stress-free nacre.

In general, nacre's ability to switch the local polarizations between the stable states with or without applied stress may assist to relieve the imposed mechanical stress or energy to certain extent. When external stress is applied, local electric fields can be generated due to the piezoelectric properties of nacre. The induced electric fields can further switch the polarizations of the nacre within their range. Hence, the effective stress acting on the nacre structure can be reduced.

❖ Role of Moisture and Biopolymers in Mollusk Shells

For all of the biological systems, water is an essential element for their surviving. However, water molecules may become obstacle for piezoresponse characterization on biomaterials due to their polar nature which can screen out the detectable piezoresponse. For dried mollusk shells, it is observed that the piezoresponse is increased compared to that of the fresh shells. On the other hand, the piezoresponse is expected to be originated from the biopolymer contents in mollusk shells because of the complex macromolecular structure of the biopolymers. To verify this assumption, biopolymers have been removed either by chemical treatment or high temperature. Results show the overall piezoresponse is greatly reduced, which confirms the previous findings.

❖ General conclusions on the Studies of EM Coupling in Biological Systems

The EM coupling of mollusk shell has been studied in detail and reported in this thesis. In addition, our preliminary studies show that bone also exhibits strong piezoresponse, which should be originated from the collagen fibrils, and this may contribute to the healing process. We also show that the cracks or damages generated on the surface of mollusk shell can be healed or change their morphologies when immersed in different solutions. It reveals the potential of mollusk shell as a kind of self-healed material, similar to bone. Therefore, the EM coupling may contribute to the improved mechanical performance of mollusk shell and the similar calcified tissues. It may also play a role in the self-healing process of these tissues. According to literatures published in recent years, soft tissues also exhibit EM coupling behaviors, and these behaviors are necessary or responsible for various tissues functionalities. The EM coupling is now believed as one of the important reasons for proper functioning of biological systems, for instance, cell movements and proliferation, neuron signal transmission, and enzyme production.

Generally speaking, the studies of EM coupling in biological systems can provide better understanding of the functional mechanisms of living organisms based on which new biomedical approaches can be developed. Also some of the organic polymers can be potential materials for flexible memory applications which can be more stable, cheaper, and environmental friendly. In recent years, many researches are focused in this area, and more efforts are required to make substantial progress.

9.2 Recommended Future Works

❖ Modeling and Simulation

One of the great challenges in studies of the roles of piezoelectric and ferroelectric properties in biological systems is to observe the direct evidence on how these properties affect the mechanical or physiological behaviors. Under some circumstances, it is impossible to achieve such goals by experiments. Thus, modeling and simulation are necessary to fully understand the role of biopiezoelectricity and bioferroelectricity on the mechanical and physiological behaviors in mollusk shells. For instance, by comparing the nanocomposite materials with normal polymer to those with piezoelectric polymer, the role of biopiezoelectricity to the mechanical issues may be revealed in certain extent. Combining the modeling and the experimental results, the speculations on the role of EM coupling in biological systems can be understand in more detail.

❖ Systematic Studies on the Electromechanical Coupling of Bone and Teeth

The healing of human hard tissue has always been a hot topic to be studied. It is widely accepted that piezoelectricity is an essential condition for bone regeneration and remodeling. However, in the past few decades, no break though results were ever reported. Most clinical proposals were also based on trial and error approach. SPM is a unique and powerful tool to study the piezoresponses of the biological systems from molecular to tissue levels. Both the piezoresponse and the electric potential on the nanoscale can be quantified

in bone by this technique. On the other hand, the study of teeth by SPM may contribute to the fabrication of teeth implant with better performance. It is believed that this study has built the methodology of EM coupling characterizations of natural hard tissues, and this can facilitate the following studies on bone, teeth, and other hard tissues in biological systems.

❖ New Generation of Synthetic Composites Inspired by Mollusk Shell Properties

So far, most of the synthetic materials from biomimicry of mollusk shell are solely based on the structural consideration, such as the alternating layer structure of hard ceramic and ductile polymer. However, none of those attempts has considered the piezoelectric and ferroelectric properties of the mollusk shells. If replacing the conventional polymers with the piezoelectric polymer, for instance, PVDF-based polymers, the toughening performance of the synthetic materials may be further improved. In this aspect, the polymers with various piezoelectric properties can be incorporated and tested. It is worth more efforts in exploring this realm in the future.

❖ Investigation of Self-healing Properties of Mollusk Shell

Some of the preliminary results on self-healing of mollusk shell have been presented in the Chapter 8. In this work, mollusk shell, as a standalone natural material without living organism, can heal itself in specific solutions under ambient conditions. This is the unique properties of biological systems. The advantages of study healing properties of mollusk shell over other biomaterials are: (1) no physiological environment needs to be reconstructed,

(2) raw materials are readily available, (3) material handling and sample preparations are relatively simple. Therefore, the studies of self-healing properties of mollusk shell can be a good start, and may provide invaluable insight on the mechanisms of biological healing that can be further applied on smart synthetic materials or biomedical applications.

References

Mukherjee, A., (ed.) 2010. Biomimetics, learning from nature. InTech, India.

Ahn, A.C., Grodzinsky, A.J., 2009. Relevance of collagen piezoelectricity to "Wolff's Law": a critical review. Med. Eng. Phys. 31, 733-741.

Alexe, M., Harnagea, C., Hesse, D., Gosele, U., 2001. Polarization imprint and size effects in mesoscopic ferroelectric structures. Appl. Phys. Lett. 79, 242-244.

Ando, Y., Fukada, E., Glimcher, M.J., 1977. Piezoelectricity of chitin in lobster shell and apodeme. Biorheology 14, 175-179.

Aschero, G., Gizdulich, P., Mango, F., Romano, S.M., 1996. Converse piezoelectric effect detected in fresh cow femur bone. J Biomech. 29, 1169-1174.

Barthelat, F., 2007. Biomimetics for next generation materials. Phil. Trans. R. Soc. A 365, 2907-2919.

Barthelat, F., Rim, J.E., Espinosa, H.D. 2009. A review on the structure and mechanical properties of mollusk shells-perspectives on synthetic biomimetic materials, pp. 17-44, In: B. Bhushan and H. Fuchs, (eds.) Applied scanning probe methods XIII: biomimetics and industrial applications, Vol. XIII. Springer.

Bassett, C.A.L., 1968. Biologic significance of piezoelectricity. Calc. Tiss. Res. 1, 252-272.

Bezares, J., Asaro, R.J., Hawley, M., 2010. Macromolecular structure of the organic framework of nacre in Haliotis rufescens: implications for mechanical response. J. Struct. Biol. 170, 484-500.

Bystrov, V.S., Bdikin, I., Heredia, A., Pullar, R.C., Mishina, E., Sigov, A.S., Kholkin, A.L. 2012. Piezoelectricity and ferroelectricity in biomaterials: from proteins to self-assembled peptide nanotubes, pp. 187-211, In: G. Ciofani and A. Menciassi, (eds.) Piezoelectric nanomaterials for biomedical applications. Springer, Berlin Heidelberg.

Campbell, S.E., Ferguson, V.L., Hurley, D.C., 2012. Nanomechanical mapping of the osteochondral interface with contact resonance force microscopy and nanoindentation. Acta Biomater. 8, 4389-4396.

Christman, J.A., Kim, S.H., Maiwa, H., Maria, J.P., Rodriguez, B.J., Kingon, A.I., Nemanich, R.J., 2000. Spatial variation of ferroelectric properties in $Pb(Zr_{0.3},Ti_{0.7})O_3$ thin films studied by atomic force microscopy. J. Appl. Phys. 87, 8031-8034.

Chu, B., Zhou, X., Ren, K., Neese, B., Lin, M., Wang, Q., Bauer, F., Zhang, Q.M., 2006. A dielectric polymer with high electric energy density and fast discharge speed. Science 313, 334-336.

Currey, J.D., Taylor, J.D., 1974. The mechanical behaviour of some molluscan hard tissues. J. Zool. 173, 395-406.

Damjanovic, D., 1998. Ferroelectric, dielectric and piezoelectric properties of ferroelectric thin films and ceramics. Rep. Prog. Phys. 61, 1267-1324.

Damjanovic, D. 2005. Hysteresis in piezoelectric and ferroelectric materials, pp. 337-465, In: I. Mayergoyz and G. Bertotti, (eds.) The Science of Hysteresis, Vol. 3. Elsevier, London.

Eaton, P., West, P., 2010. Atomic Force Microscopy Oxford University Press, United States.

Eibl, R., 2009. Direct Force Measurements of Receptor–Ligand Interactions on Living Cells, pp. 1-31, In: B. Bhushan and H. Fuchs, (eds.), Applied Scanning Probe Methods XII, Springer Berlin Heidelberg.

Espinosa, H.D., Rim, J.E., Barthelat, F., Buehler, M.J., 2009. Merger of structure and material in nacre and bone- Perspectives on de novo biomimetic materials. Prog. Mater. Sci. 54, 1059-1100.

Farinholt, K.M., Pedrazas, N.A., Schluneker, D.M., Burt, D.W., Farrar, C.R., 2008. An energy harvesting comparison of piezoelectric and Ionically conductive polymers. J. Intell. Mater. Syst. Struct. 20, 633-642.

Fleischli, F.D., Dietiker, M., Borgia, C., Spolenak, R., 2008. The influence of internal length scales on mechanical properties in natural nanocomposites: a comparative study on inner layers of seashells. Acta Biomater. 4, 1694-1706.

Frost, H.M., 2004. A 2003 update of bone physiology and Wolff's Law for clinicians. Angle. Orthod. 74, 3-15.

Fu, D.W., Cai, H.L., Liu, Y., Ye, Q., Zhang, W., Zhang, Y., Chen, X.Y., Giovannetti, G., Capone, M., Li, J., Xiong, R.G., 2013. Diisopropylammonium bromide is a high-temperature molecular ferroelectric crystal. Science 339, 425-428.

Fukada, E., 1968a. Piezoelectricity as a fundamental property of wood. Wood Sci. Technol. 2, 299-307.

Fukada, E., 1968b. Piezoelectricity in polymers and biological materials. Ultrasonics 6, 229-234.

Fukada, E., 1995. Piezoelectricity of biopolymers. Biorheology 32, 593-609.

Fukada, E., 2000. History and recent progress in piezoelectric polymers. IEEE Trans. Ultrason. Ferroelectr. Freq. Control. 47, 1277-1290.

Fukada, E., Yasuda, I., 1957. On the piezoelectric effect of bone. J. Phys. Soc. Jpn. 12, 1158-1162.

Fukada, E., Ueda, H., 1970. Piezoelectric effect in muscle. Jan. J. Appl. Phys. 9, 844-845.

Fukada, E., Date, M., 1973. Piezoelectric relaxations in polymers: spherical dispersion model. J. Macromol. Sci. B 8, 463 - 474.

Gannepalli, A., Yablon, D.G., Tsou, A.H., Proksch, R., 2011. Mapping nanoscale elasticity and dissipation using dual frequency contact resonance AFM. Nanotechnology 22, 355705.

Garcia, R., Tamayo, J., Paulo, A.S., 1999. Phase contrast and surface energy hysteresis in tapping mode scanning force microscopy. Surf. Interface Anal. 27, 312-316.

García, R., Pérez, R., 2002. Dynamic atomic force microscopy methods. Surf. Sci. Rep. 47, 197-301.

Gautier, B., Thiebaud, C., Charraut, D., Labrune, J.C., 2002. Nanoscale investigation of the ferroelectric properties of sol-gel ($PbZr_xTi_{1-x}O_3$) films. Ferroelectrics 269, 219-224.

Goes, J.C., Figueiro, S.D., Paiva, J.A.D., Sombra, A.S.B., 1999. Piezoelectric and dielectric properties of collagen films. Phys. Status. Solidi. A 176, 1077-1083.

Griffin, M., Bayat, A., 2011. Electrical stimulation in bone healing: critical analysis by evaluation levels of evidence. ePlasty 11, e34. Retrieved from: http://www.ncbi.nlm.nih.gov/pmc/articles/PMC3145421/.

Gruverman, A., Kalinin, S.V., 2006. Piezoresponse force microscopy and recent advances in nanoscale studies of ferroelectrics. J. Mater. Sci. 41, 107-116.

Gruverman, A., Rodriguez, B.J., Kalinin, S.V. 2007. Electromechanical behavior in biological systems at the nanoscale, pp. 615-633, In: S. V. Kalinin and A. Gruverman, (eds.) Scanning probe microscopy, Vol. III. Springer, New York.

Habelitz, S., Rodriguez, B.J., Marshall, S.J., Marshall, G.W., Kalinin, S.V., Gruverman, A., 2007. Peritubular dentin lacks piezoelectricity. J. Dent. Res. 86, 908-911.

Halperin, C., Mutchnik, S., Agronin, A., Molotskii, M., Urenski, P., Salai, M., Rosenman, G., 2004. Piezoelectric effect in human bones studied in nanometer scale. Nano Lett. 4, 1253-1256.

Hastings, G.W., Mahmud, F.A., 1988. Electrical effects in bone. J. Biomed. Eng. 10, 515-521.

Heinemann, F., Treccani, L., Fritz, M., 2006. Abalone nacre insoluble matrix induces growth of flat and oriented aragonite crystals. Biochem. Biophys. Res. Commun. 344, 45-49.

Heinemann, F., Launspach, M., Gries, K., Fritz, M., 2011. Gastropod nacre: structure, properties and growth - biological, chemical and physical basics. Biophys. Chem. 153, 126-153.

Heredia, A., Meunier, V., Bdikin, I.K., Gracio, J., Balke, N., Jesse, S., Tselev, A., Agarwal, P.K., Sumpter, B.G., Kalinin, S.V., Kholkin, A.L., 2012. Nanoscale Ferroelectricity in Crystalline γ-Glycine. Adv. Funct. Mater. 22, 2996-3003.

Heuer, A.H., Fink, D.J., Laraia, V.J., Arias, J.L., Calvert, P.D., Kendall, K., Messing, G.L., Blackwell, J., Rieke, P.C., Thompson, D.H., Wheeler, A.P., Veis, A., Caplan, A.I., 1992. Innovative materials processing strategies- a biomimetic approach. Science 255, 1098-1105.

Hurley, D.C., 2009. Contact Resonance ForceMicroscopy techniques for nanomechanical measurements, pp. 97-138, In: B. Bhushan and H. Fuchs, (eds.) Applied Scanning Probe Methods XI: Scanning Probe Microscopy Techniques, Springer, Heidelberg.

Hurley, D.C., 2010. Measuring Mechanical Properties on the Nanoscale with Contact Resonance Force Microscopy Methods, pp. 95-124, In: S. V. Kalinin and A. Gruverman, (eds.) Scanning Probe Microscopy of FUnctional Materials: Nanoscale Imaging and Spectroscopy, Springer, New York.

Isaacson, B.M., Bloebaum, R.D., 2010. Bone bioelectricity: what have we learned in the past 160 years? J. Biomed. Mater. Res. A 95, 1270-1279.

Isakov, D.V., Gomes, E.D.M., Almeida, B.G., Bdikin, I.K., Martins, A.M., Kholkin, A.L., 2010. Piezoresponse force microscopy studies of the triglycine sulfate-based nanofibers. J. Appl. Phys. 108, 042011.

Jackson, A.P., Vincent, J.F.V., Turner, R.M., 1988. The mechanical design of nacre. Proc. R. Soc. Lond. B 234, 415-440.

Jackson, A.P., Vincent, J.F.V., Turner, R.M., 1990. Comparison of nacre with other ceramic composites. J. Mater. Sci. 25, 3173-3178.

Jesse, S., Kalinin, S.V., 2011. Band excitation in scanning probe microscopy: sines of change. J. Phys. D Appl. Phys. 44, 464006.

Jesse, S., Lee, H.N., Kalinin, S.V., 2006. Quantitative mapping of switching behavior in piezoresponse force microscopy. Rev. Sci. Instrum. 77, 073702.

Jesse, S., Baddorf, A.P., Kalinin, S.V., 2006. Switching spectroscopy piezoresponse force microscopy of ferroelectric materials. Appl. Phys. Lett. 88, 062908.

Jesse, S., Kalinin, S.V., Proksch, R., Baddorf, A.P., Rodriguez, B.J., 2007. The band excitation method in scanning probe microscopy for rapid mapping of energy dissipation on the nanoscale. Nanotechnology 18, 435503.

Jesse, S., Kumar, A., Kalinin, S.V., Gannepali, A., Proksch, R. 2010. Band excitation scanning probe microscopies: travelling through the fourier space. Retrieved from: http://www.asylumresearch.com/Applications/BandExcitation/BandExcitation.shtml.

Ji, B., Gao, H., 2010. Mechanical principles of biological nanocomposites. Annu. Rev. Mater. Res. 40, 77-100.

Kalinin, S., Karapetian, E., Kachanov, M., 2004. Nanoelectromechanics of piezoresponse force microscopy. Phys. Rev. B 70, 184101.

Kalinin, S.V., Rar, A., Jesse, S., 2006. A decade of piezoresponse force microscopy: Progress, challenges, and opportunities. IEEE Trans. Ultrason. Ferroelectr. Freq. Control. 53, 2226-2252.

Kalinin, S.V., Jesse, S., Liu, W., Balandin, A.A., 2006a. Evidence for possible flexoelectricity in tobacco mosaic viruses used as nanotemplates. Appl. Phys. Lett. 88, 153902.

Kalinin, S.V., Morozovska, A.N., Chen, L.Q., Rodriguez, B.J., 2010. Local polarization dynamics in ferroelectric materials. Rep. Prog. Phys. 73, 056502.

Kalinin, S.V., Rodriguez, B.J., Jesse, S., Thundat, T., Gruverman, A., 2005. Electromechanical imaging of biological systems with sub-10nm resolution. Appl. Phys. Lett. 87, 053901.

Kalinin, S.V., Rodriguez, B.J., Jesse, S., Karapetian, E., Mirman, B., Eliseev, E.A., Morozovska, A.N., 2007a. Nanoscale electromechanics of ferroelectric and biological systems: a new dimension in scanning probe microscopy. Annu. Rev. Mater. Res. 37, 189-238.

Kalinin, S.V., Rodriguez, B.J., Shin, J., Jesse, S., Grichko, V., Thundat, T., Baddorf, A.P., Gruverman, A., 2006c. Bioelectromechanical imaging by scanning probe microscopy: galvani's experiment at the nanoscale. Ultramicroscopy 106, 334-340.

Kalinin, S.V., Rodriguez, B.J., Jesse, S., Shin, J., Baddorf, A.P., Gupta, P., Jain, H., Williams, D.B., Gruverman, A., 2006b. Vector piezoresponse force microscopy. Microsc. Microanal. 12, 206-220.

Kalinin, S.V., Rodriguez, B.J., Jesse, S., Seal, K., Proksch, R., Hohlbauch, S., Revenko, I., Thompson, G.L., Vertegel, A.A., 2007b. Towards local electromechanical probing of cellular and biomolecular systems in a liquid environment. Nanotechnology 18, 1-10.

Kareem, A.U., Solares, S.D., 2012. Characterization of surface stiffness and probe-sample dissipation using the band excitation method of atomic force microscopy: a numerical analysis. Nanotechnology 23, 015706.

Katti, K.S., Katti, D.R., Mohanty, B. 2010. Biomimetics lessons learnt from nacre, pp. 193-216, In: A. Mukherjee, (ed.) Biomimetics, learning from nature. InTech, India.

Kholkin, A.L., Kalinin, S.V., Roelofs, A., Gruverman, A. 2007. Review of ferroelectric domain imaging by piezoresponse force microscopy, In: S. Kalinin and A. Gruverman, (eds.) Scanning Probe Microscopy. Springer, New York.

Kijima, M., Oaki, Y., Imai, H., 2011. In vitro repair of a biomineral with a mesocrystal structure. Chemistry 17, 2828-2832.

Killgore, J.P., Geiss, R.H., Hurley, D.C., 2011. Continuous measurement of atomic force microscope tip wear by contact resonance force microscopy. Small 7, 1018-1022.

Killgore, J.P., Kelly, J.Y., Stafford, C.M., Fasolka, M.J., Hurley, D.C., 2011a. Quantitative subsurface contact resonance force microscopy of model polymer nanocomposites. Nanotechnology 22, 175706.

Killgore, J.P., Yablon, D.G., Tsou, A.H., Gannepalli, A., Yuya, P.A., Turner, J.A., Proksch, R., Hurley, D.C., 2011b. Viscoelastic Property Mapping with Contact Resonance Force Microscopy. Langmuir 27, 13983-13987.

Lang, S.B., 2000. Piezoelectricity, pyroelectricity and ferroelectricity in biomaterials speculation on their biological significance. IEEE Trans. Dielectr. Electr. Insul. 7, 466-473.

Launspach, M., Rückmann, K., Gummich, M., Rademaker, H., Doschke, H., Radmacher, M., Fritz, M., 2012. Immobilisation and characterisation

of the demineralised, fully hydrated organic matrix of nacre – An atomic force microscopy study. Micron 43, 1351-1363.

Lee, K.Y.K., Nyein, M.K., Moore, D.F., Joannopoulos, J.D., Socrate, S., Imholt, T., Radovitzky, R., Johnson, S.G., 2011. Blast-induced electromagnetic fields in the brain from bone piezoelectricity. NeuroImage 54, Supplement 1, S30-S36.

Lemanov, V.V., 2000b. Piezoelectric and pyroelectric properties of protein amino acids as basic materials of Soft State Physics. Ferroelectrics 238, 211-218.

Lemanov, V.V., 2000a. Piezo-, pyro-, and ferroelectricity in biological materials, p. 1-9, in: C. Galassi, M. Dinescu, K. Uchino, M. Sayer, (eds.) Piezoelectric Materials: Advances in Science, Technology and Applications, Springer, Netherlands.

Lemanov, V.V., Sochava, L.S., 2003. Hindered rotation of the CH3 group in L-alanine single crystals: Temperature-induced transformation of the ESR spectrum. Phys. Solid State 45, 1455-1458.

Lemanov, V.V., Popov, S.N., Pankova, G.A., 2002. Piezoelectric properties of crystals of some protein aminoacids and their related compounds. Phys. Solid State 44, 1929-1935.

Lemanov, V.V., Popov, S.N., Pankova, G.A., 2011. Piezoelectricity in protein amino acids. Phys. Solid State 53, 1191-1193.

Li, Q., Liu, Y., Schiemer, J., Smith, P., Li, Z., Withers, R.L., Xu, Z., 2011. Fully-inverted piezoresponse hysteresis loops mediated by charge injection in $0.29Pb(In_{1/2}Nb_{1/2})O_3–0.44Pb(Mg_{1/3}Nb_{2/3})O_3–0.27PbTiO_3$ single crystals. Appl. Phys. Lett. 98, 092908.

Li, T., Zeng, K., 2011. Piezoelectric properties and surface potential of green abalone shell studied by scanning probe microscopy techniques. Acta Mater. 59, 3667-3679.

Li, T., Zeng, K., 2012. Nano-hierarchical structure and electromechanical coupling properties of clamshell. J. Struct. Biol. 180, 73-83.

Li, T., Zeng, K., 2013. Nanoscale piezoelectric and ferroelectric behaviors of seashell by piezoresponse force microscopy. J. Appl. Phys. 113, 187202.

Li, T., Chen, L., Zeng, K., 2013. In situ studies of nanoscale electromechanical behavior of nacre under flexural stresses using band excitation PFM. Acta Biomater. 9, 5903-5912.

Li, X., Chang, W.C., Chao, Y.J., Wang, R., Chang, M., 2004. Nanoscale structural and mechanical characterization of a natural nanocomposite material: the shell of red abalone. Nano Lett. 4, 613-617.

Lin, A., Meyers, M.A., 2005. Growth and structure in abalone shell. Mater. Sci. Eng. A 390, 27-41.

Lin, A.Y.M., Meyers, M.A., Vecchio, K.S., 2006. Mechanical properties and structure of strombus gigas, tridacna gigas, and haliotis rufescens sea shells: a comparative study. Mater. Sci. Eng. C 26, 1380-1389.

Liu, Y., Zhang, Y., Chow, M.J., Chen, Q., Li, J., 2012. Biological ferroelectricity uncovered in aortic Walls by Piezoresponse Force Microscopy. Phys. Rev. Lett. 108, 078103.

Liu, Y., Wang, Y., Chow, M.J., Chen, N.Q., Ma, F., Zhang, Y., Li, J., 2013. Glucose Suppresses Biological Ferroelectricity in Aortic Elastin. Phys. Rev. Lett. 110, 168101.

Maeda, H., Fukada, E., 1982. Effect of water on piezoelectric, dielectric, and elastic properties of bone. Biopolymers 21, 2055-2068.

Majid, M.-J., Yu, M.F., 2009. Nanoscale characterization of isolated individual type I collagen fibrils: polarization and piezoelectricity. Nanotechnology 20, 085706.

Marin, F., Luquet, G., 2004. Molluscan shell proteins. C. R. Palevol 3, 469-492.

Marino, A.A., Becker, R.O., Soderholm, S.C., 1971. Origin of the piezoelectric effect in bone. Calc. Tiss. Res. 8, 177-180.

Martelet, C., Jaffrezic-Renault, N., Hou, Y., Errachid, A., Bessueille, F., 2007. Nanostructuration and Nanoimaging of Biomolecules for Biosensors, pp. 225-257, In: B. Bhushan and H. Fuchs, (eds.) Applied Scanning Probe Methods VII, Springer, Heidelberg.

Meyers, M.A., Lin, A.Y., Chen, P.Y., Muyco, J., 2008. Mechanical strength of abalone nacre: role of the soft organic layer. J. Mech. Behav. Biomed. Mater. 1, 76-85.

Minary-Jolandan, M., Yu, M.F., 2010. Shear piezoelectricity in bone at the nanoscale. Appl. Phys. Lett. 97, 153127.

Mirfakhrai, T., Madden, J.D.W., Baughman, R.H., 2007. Polymer artificial muscles. Mater. Today 10, 30-38.

Mohanty, B., Katti, K.S., Katti, D.R., Verma, D., 2006. Dynamic nanomechanical response of nacre. J. Mater. Res. 21, 2045-2051.

Moshe-Drezner, H., Shilo, D., Dorogoy, A., Zolotoyabko, E., 2010. Nanometer-Scale Mapping of Elastic Modules in Biogenic

Composites: The Nacre of Mollusk Shells. Adv. Funct. Mater. 20, 2723-2728.

Nikiforov, M.P., Thompson, G.L., Reukov, V.V., Jesse, S., Guo, S., Rodriguez, B.J., Seal, K., Vertegel, A.A., Kalinin, S.V., 2010. Double-layer mediated electromechanical response of amyloid fibrils in liquid environment. ACS nano 4, 689-698.

Nudelman, F., Chen, H.H., Goldberg, H.A., Weiner, S., Addadi, L., 2007. Lessons from biomineralization: comparing the growth strategies of mollusc shell prismatic and nacreous layers in atrina rigida. Faraday Discuss. 136, 9-25.

Pereira-Mouries, L., Almeida, M.J., Ribeiro, C., Peduzzi, J., Barthelemy, M., Milet, C., Lopez, E., 2002. Soluble silk-like organic matrix in the nacreous layer of the bivalve Pinctada maxima. Eur. J. Biochem. 269, 4994-5003.

Peter, F., Rudiger, A., Waser, R., Szot, K., Reichenberg, B., 2005. Comparison of in-plane and out-of-plane optical amplification in AFM measurements. Rev. Sci. Instrum. 76, 046101.

Peterlik, H., Roschger, P., Klaushofer, K., Fratzl, P., 2006. From brittle to ductile fracture of bone. Nat. Mater. 5, 52-55.

Pokroy, B., Zolotoyabko, E., 2003. Microstructure of natural plywood-like ceramics: a study by high-resolution electron microscopy and energy-variable X-ray diffraction. J. Mater. Chem. 13, 682-688.

Pokroy, B., Fitch, A.N., Lee, P.L., Quintana, J.P., Caspi, E.N., Zolotoyabko, E., 2006. Anisotropic lattice distortions in the mollusk-made aragonite: a widespread phenomenon. J. Struct. Biol. 153, 145-150.

Proksch, R., Kalinin, S.V. Piezoresponse force microscopy with asylum research AFMs. Retrieved from: http://www.asylumresearch.com/Applications/PFMAppNote/PFMAppNote.shtml.

Proksch, R., Schäffer, T.E., Cleveland, J.P., Callahan, R.C., Viani, M.B., 2004. Finite optical spot size and position corrections in thermal spring constant calibration. Nanotechnology 15, 1344-1350.

Rao, P.R., 2003. Biomimetics. Sadhana 28, 657-676.

Rodriguez, B., Jesse, S., Baddorf, A., Kalinin, S., 2006a. High resolution electromechanical imaging of ferroelectric materials in a liquid environment by piezoresponse force microscopy. Phys. Rev. Lett. 96.

Rodriguez, B.J., Callahan, C., Kalinin, S.V., Proksch, R., 2007. Dual-frequency resonance-tracking atomic force microscopy. Nanotechnology 18, 475504.

Rodriguez, B.J., Gruverman, A., Kingon, A.I., Nemanich, R.J., Ambacher, O., 2002. Piezoresponse force microscopy for polarity imaging of GaN. Appl. Phys. Lett. 80, 4166-4168.

Rodriguez, B.J., Jesse, S., Seal, K., Balke, N., Kalinin, S.V., Proksch, R., 2010. Dynamic and Spectroscopic Modes and Multivariate Data Analysis in Piezoresponse Force Microscopy, pp. 491-528, In: S. V. Kalinin and A. Gruverman, (eds.) Scanning Probe Microscopy of Functional Materials, Springer, New York.

Rodriguez, B.J., Kalinin, S.V., Jesse, S., Thompson, G., Vertegel, A., Hohlbauch, S., Proksch, R., 2008. Nanoelectromechanics of inorganic and biological systems from structural imaging to local functionalities.

Microscopy Today, 28-33. Retrieved from: http://www.asylumresearch.com/Products/PFM/ABKalinin2.pdf.

Rodriguez, B.J., Kalinin, S.V., Shin, J., Jesse, S., Grichko, V., Thundat, T., Baddorf, A.P., Gruverman, A., 2006b. Electromechanical imaging of biomaterials by scanning probe microscopy. J. Struct. Biol. 153, 151-159.

Rousseau, M., Lopez, E., Stempflé, P., Brendlé, M., Franke, L., Guette, A., Naslain, R., Bourrat, X., 2005. Multiscale structure of sheet nacre. Biomaterials 26, 6254-6262.

Sahagun, E., Garcia-Mochales, P., Sacha, G.M., Saenz, J.J., 2007. Energy dissipation due to capillary interactions: Hydrophobicity maps in force microscopy. Phys. Rev. Lett. 98, 176106.

Sarikaya, M., Gunnison, K.E., Yasrebi, M., Aksay, I.A., 1990. Mechanical property-microstructural relationships in abalone shell. Mater. Res. Soc. Symp. P. 174, 109-116.

Schneider, G.A., 2007. Influence of electric field and mechanical stresses on the fracture of ferroelectrics. Annu. Rev. Mater. Res. 37, 491-538.

Schöberl, T., Jäger, I.L., Lichtenegger, H.C., 2009. Application of SPM and Related Techniques to the Mechanical Properties of Biotool Materials, pp. 71-103, In: B. Bhushan and H. Fuchs, (eds.) Applied Scanning Probe Methods XIII, Springer, Heidelberg.

Sencadas, V., Ribeiro, C., Heredia, A., Bdikin, I.K., Kholkin, A.L., Lanceros-Mendez, S., 2012. Local piezoelectric activity of single poly(L-lactic acid) (PLLA) microfibers. Appl. Phys. A 109, 51-55.

Shahinpoor, M., 2003. Ionic polymer - conductor composites as biomimetic sensors, robotic actuators and artificial muscles- a review. Electrochim. Acta 48, 2343-2353.

Shamos, M.H., Lavine, L.S., 1967. Piezoelectricity as a fundamental property of biological tissues. Nature 213, 267-269.

Shamos, M.H., Shamos, M.I., Lavine, L.S., 1963. Piezoelectric effect in bone. Nature 197, 81.

Smith, B.L., Schaffer, T.E., Viani, M., Thompson, J.B., Frederick, N.A., Kindt, J., Belcher, A., Stucky, G.D., Morse, D.E., Hansma, P.K., 1999. Molecular mechanistic origin of the toughness of natural adhesives, fibres and composites. Nature 399, 761-763.

Soergel, E., 2011. Piezoresponse force microscopy (PFM). J. Phys. D Appl. Phys. 44, 1-18.

Song, F., Soh, A.K., Bai, Y.L., 2003. Structural and mechanical properties of the organic matrix layers of nacre. Biomaterials 24, 3623-3631.

Song, F., Zhou, J., Xu, X., Xu, Y., Bai, Y., 2008. Effect of a negative poisson ratio in the tension of ceramics. Phys. Rev. Lett. 100, 245502.

Stempfl é, P., Pantal é, O., Rousseau, M., Lopez, E., Bourrat, X., 2010. Mechanical properties of the elemental nanocomponents of nacre structure. Mat. Sci. Eng. C 30, 715-721.

Stokke, M.K., Rivelsrud, F., Sjaastad, I., Sejersted, O.M., Swift, F., 2012. From global to local: a new understanding of cardiac electromechanical coupling. Tidsskr. Nor. Legeforen. 132, 1457-1460.

Sumitomo, T., Kakisawa, H., Owaki, Y., Kagawa, Y., 2008. In situ transmission electron microscopy observation of reversible deformation in nacre organic matrix. J. Mater. Res. 23, 1466-1471.

Tamayo, J., Garcia, R., 1998. Relationship between phase shift and energy dissipation in tapping-mode scanning force microscopy. Appl . Phys. Lett. 73, 2926-2928.

Tang, C.Y., Chan, L.C., Liang, J.Z., Cheng, K.W.E., Wong, T.L., 2002. Mechanical and thermal properties of ABS-CaCO3 composites. J. Reinf. Plast. Comp. 21, 1337-1345.

Tao, J.H., Zhou, D.M., Zhang, Z.S., Xu, X.R., Tang, R.K., 2009. Magnesium-aspartate-based crystallization switch inspired from shell molt of crustacean. PNAS 106, 22096-22101.

Towe, K.M., Hamilton, G.H., 1968. Ultrastructure and inferred calcification of the mature and developing nacre in bivalve mollusks. Calc. Tiss. Res. 1, 306-318.

Treccani, L., Mann, K., Heinemann, F., Fritz, M., 2006. Perlwapin, an abalone nacre protein with three four-disulfide core (whey acidic protein) domains, inhibits the growth of calcium carbonate crystals. Biophys. J. 91, 2601-2608.

Wang, R.Z., Wen, H.B., Cui, F.Z., Zhang, H.B., Li, H.D., 1995. Observations of damage morphologies in nacre during deformation and fracture. J. Mater. Sci. 30, 2299-2304.

Wang, R.Z., Suo, Z., Evans, A.G., Yao, N., Aksay, I.A., 2001. Deformation mechanisms in nacre. J. Mater. Res. 16, 2485-2493.

Wang, T., Feng, Z.D., Song, Y.X., Chen, X.L., 2007. Piezoelectric properties of human dentin and some influencing factors. Dent. Mater. 23, 450-453.

Wang, Y., Zhou, X., Chen, Q., Chu, B.J., Zhang, Q.M., 2010. Recent development of high energy density polymers for dielectric capacitors. IEEE Trans. Dielectr. Electr. Insul. 17, 1036-1042.

Xu, Z.H., Li, X.D., 2011. Deformation strengthening of biopolymer in nacre. Adv. Funct. Mater. 21, 3883-3888.

Yablon, D.G., Gannepalli, A., Proksch, R., Killgore, J., Hurley, D.C., Grabowski, J., Tsou, A.H., 2012. Quantitative Viscoelastic Mapping of Polyolefin Blends with Contact Resonance Atomic Force Microscopy. Macromolecules 45, 4363-4370.

Zhang, T.Y., Zhao, M.H., Liu, G.N., 2004. Failure behavior and failure criterion of conductive cracks (deep notches) in piezoelectric ceramics I - the charge-free zone model. Acta Mater. 52, 2013-2024.

Zhang, Z., Meng, Q., Chung, T., 2009. Energy storage study of ferroelectric poly(vinylidene fluoride-trifluoroethylene-chlorotrifluoroethylene) terpolymers. Polymer 50, 707-715.

Zhang, Z.C., Chung, T.C.M., 2007. The structure-property relationship of poly(vinylidene difluoride)-based polymers with energy storage and loss under applied electric fields. Macromolecules 40, 9391-9397.

Zhu, Z., Tong, H., Ren, Y., Hu, J., 2006. Meretrix lusoria--a natural biocomposite material: in situ analysis of hierarchical fabrication and micro-hardness. Micron 37, 35-40.

Appendix A – Glossary of Terms in Electromechanical Coupling

Curie-Weiss law: It describes the magnetic susceptibility χ of a ferromagnet in the paramagnetic region above the Curie point.

$\chi = \frac{C}{T - T_c}$, where C is Curie constant, T_c is Curie temperature.

Dipole moment: A vector that defined by the product of the magnitude of charge and the distance of separation between the charges.

Electromechanical coupling: Materials behaviors that generally involve conversions between electrical energy and mechanical energy.

Electrostriction: A property of all dielectric materials that causes them to change their shape under the application of electric field. The resulting strain is proportional to the square of polarization.

Ferroelectricity: A property of piezoelectric material that have a spontaneous electric polarization that can be reversed by the application of an external electric field.

Ion channel: Pore-forming membrane proteins whose functions include establishing a resting membrane potential, shaping action potentials and other electrical signals by gating the flow of ions across the cell membrane, controlling the flow of ions across secretory and epithelial cells, and regulating cell volume.

Paraelectricity: Ability of materials to become polarized under an applied electric field. Permanent dipole is not necessary. Removal of the fields results in the polarization in the material returning to zero (electric-induced polarization). This behavior is caused by the distortion of individual ions (displacement of the electron cloud from the nucleus) and the polarization of molecules or combinations of ions or defects.

Piezoelectricity: When a piece of piezoelectric material is mechanically deformed, it becomes electrically polarized. The magnitude of the polarization depends on the electric field present or induced in the materials.

Polarization: A net vector sum of dipole moment in a polar material.

Pyroelectricity: Ability of materials to generate a temporary voltage when they are heated or cooled. The positions of the atoms within the crystal structure can be modified by temperature, so that the polarization changes, which gives rise to a voltage across the crystal.

Appendix B - Complimentary PFM Images

1. PFM images of partially decalcified nacre [surface ($30 \times 30\ \mu m^2$) and cross-section ($5 \times 5\ \mu m^2$)]. Biopolymer matrix is clearly revealed in the amplitude and phase images.

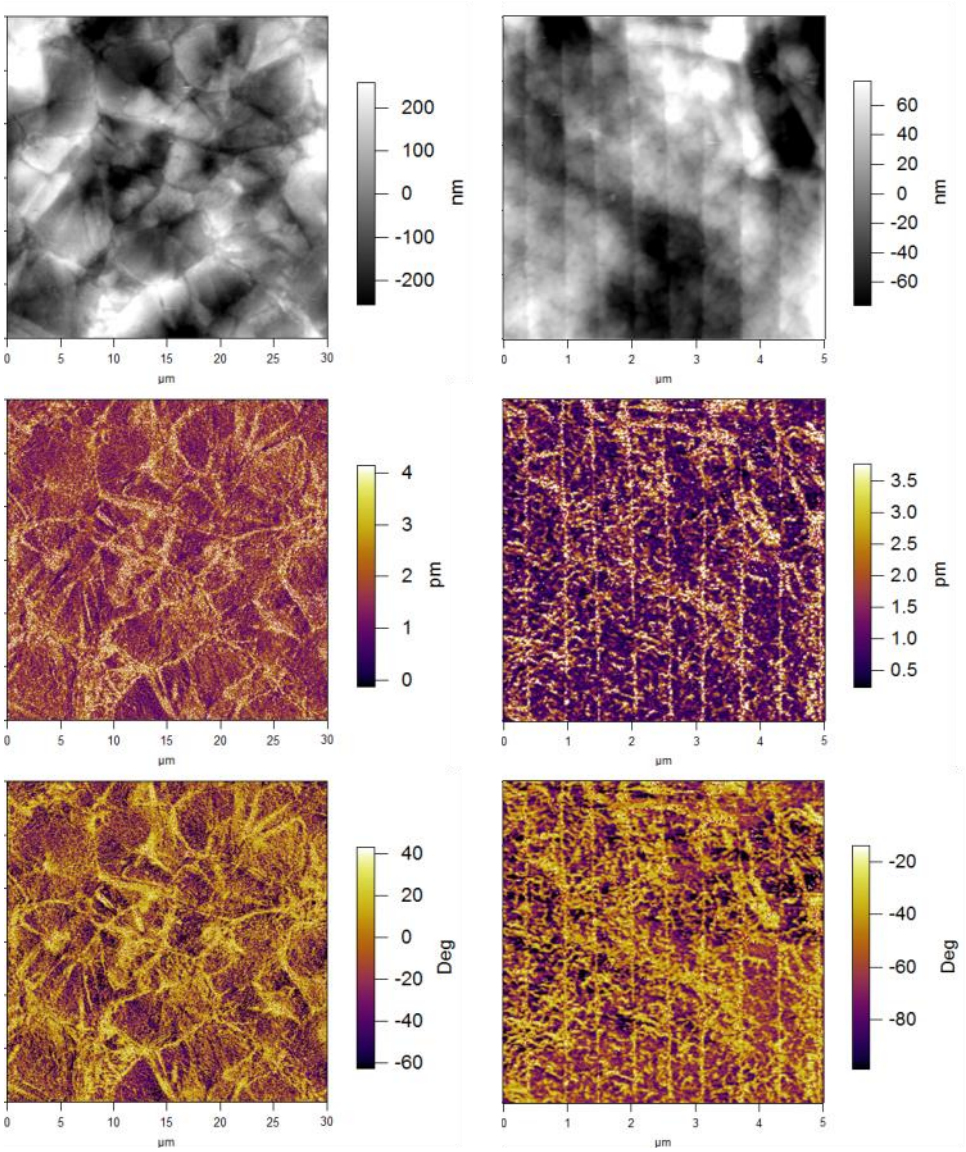

2. PFM images (20×20 μm^2) of indented fresh vs. healed decalcified nacre surface (1hr in DI water)

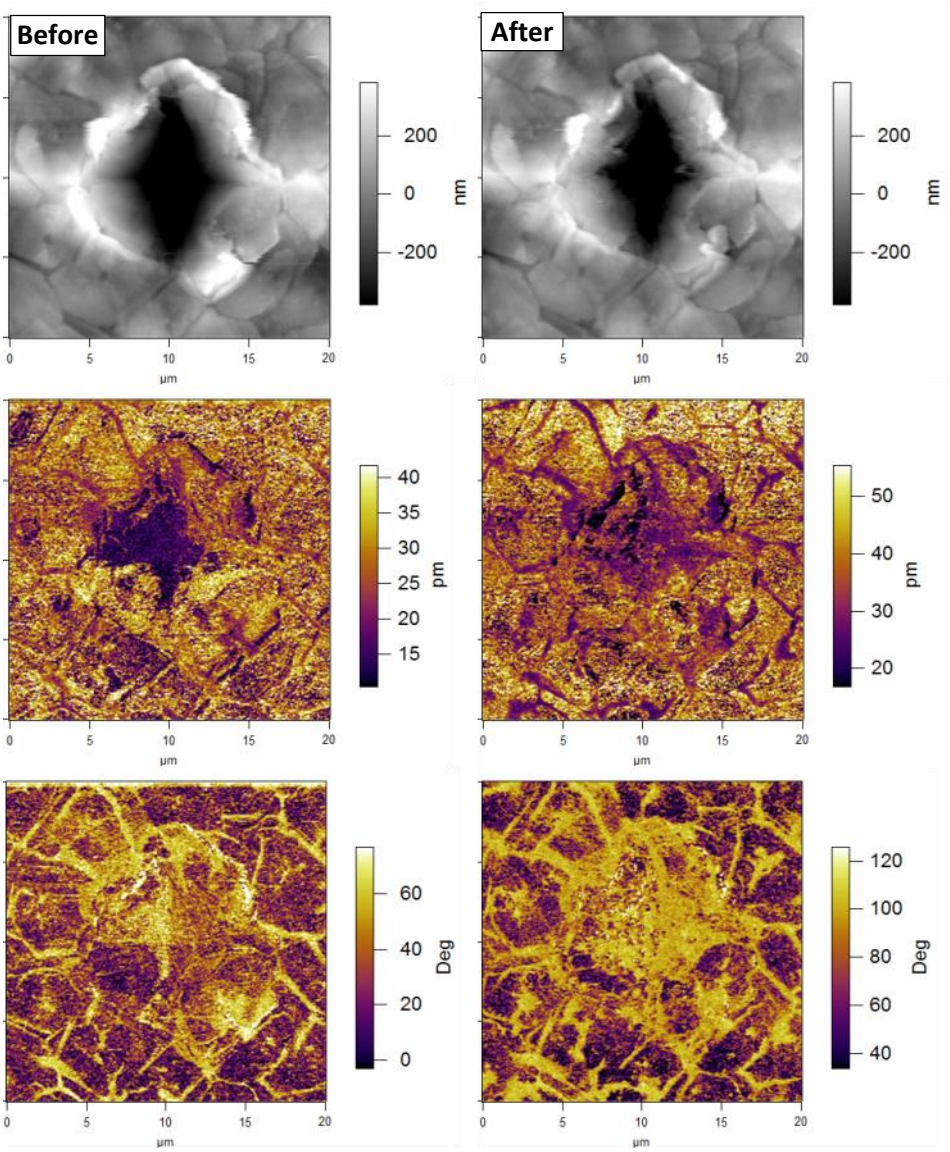

3. PFM images (15×15 μm^2) of indented fresh vs. healed deproteinated cross-sectional nacre (1hr in 3.5% NaCl solution)

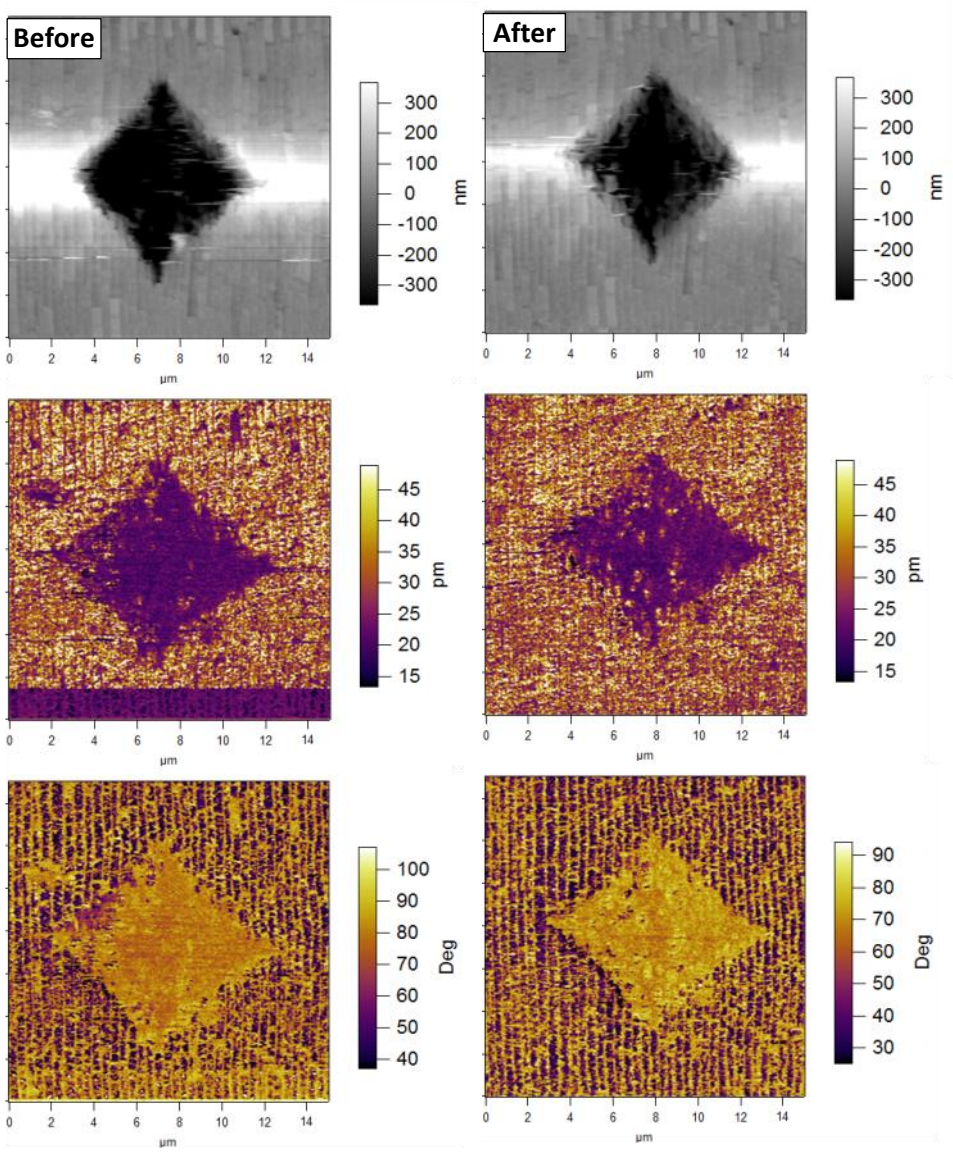

Appendix C – SS-PFM Mappings of Cross-Sectional Abalone Shell under Flexural Stresses

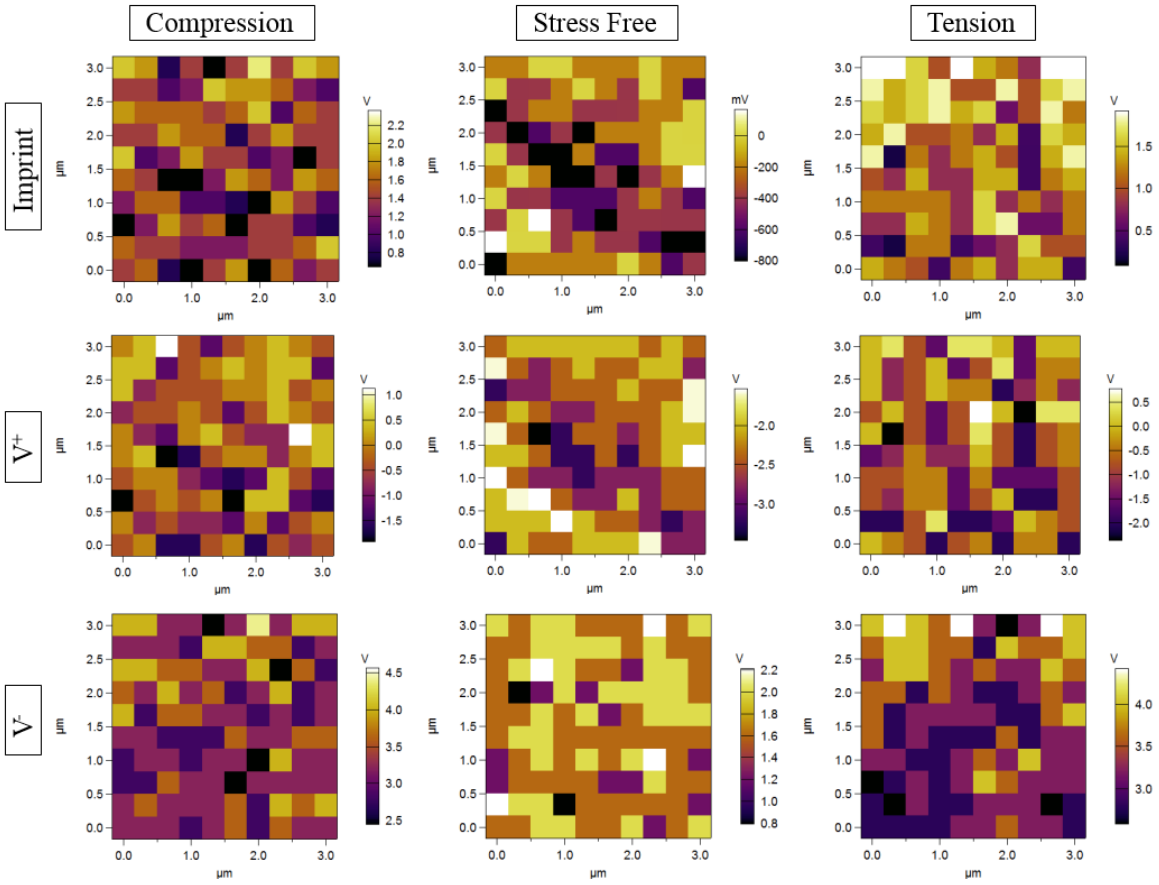

Appendix D – Stress Distribution in Cross-sectional Abalone Shell Observed by Finite Element method

1. Thinner shell sample (8.6 mm × 0.5 mm)

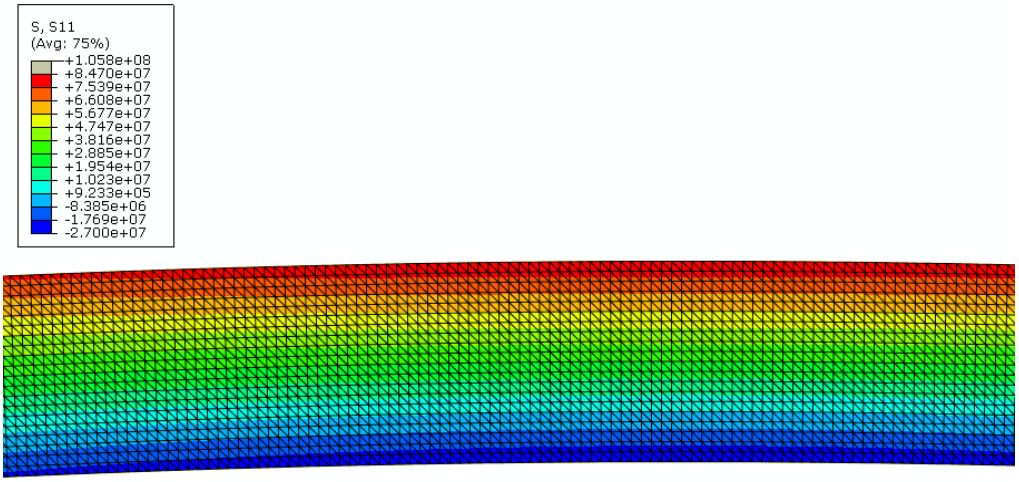

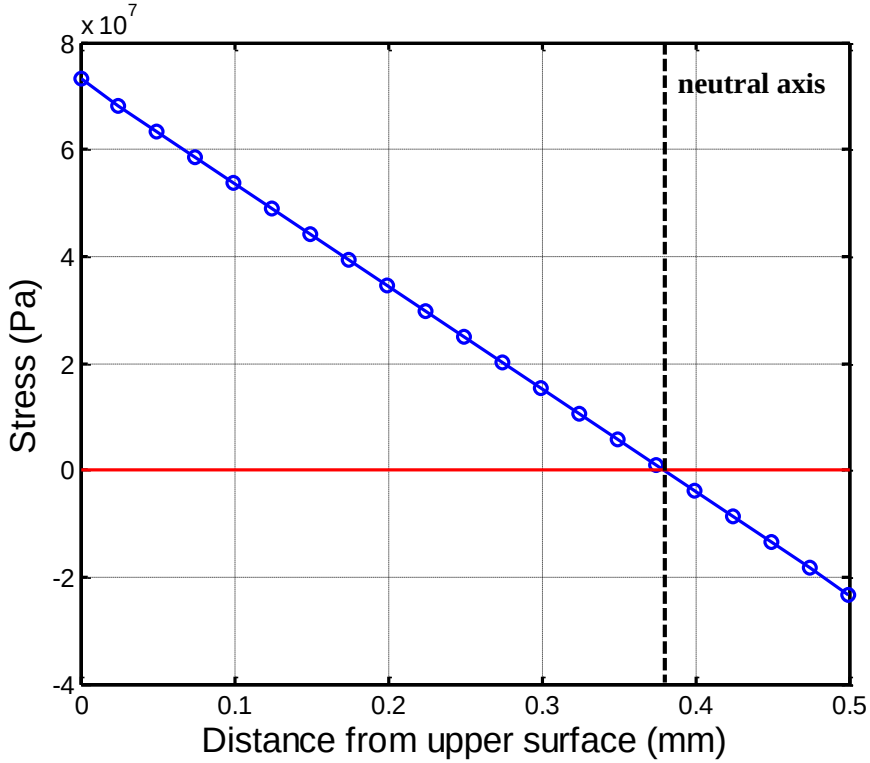

2. Thicker shell sample (11 mm × 1 mm)